Design and Control of Mechanoneural Interfaces for Neuroprosthetic Limbs

by

Hyungeun Song
B.E. Electrical Engineering and Computer Science
Nagoya University, 2014

M.E. Electrical Engineering and Information Systems
The University of Tokyo, 2016

Submitted to the Harvard-MIT
Program in Health Sciences and Technology
in Partial Fulfillment of the Requirements for the Degree of

DOCTOR OF PHILOSOPHY IN MEDICAL ENGINEERING AND MEDICAL PHYSICS

at the

MASSACHUSETTS INSTITUTE OF TECHNOLOGY

JUNE 2023

Authored by: Hyungeun Song
Harvard-MIT Program in Health Sciences and Technology
May 19, 2023

Certified by: Hugh Herr, PhD
Professor of MIT Media Arts and Sciences
Director of the MIT Biomechatronics Group
Co-director of the MIT K. Lisa Yang Center for Bionics

Accepted by: Collin M. Stultz, MD, PhD
Director, Harvard-MIT Program in Health Sciences and Technology
Nina T. and Robert H. Rubin Professor in Medical Engineering and Science
Professor of Electrical Engineering and Computer Science

Design and Control of Mechanoneural Interfaces for Neuroprosthetic Limbs

by

Hyungeun Song

Submitted to the Harvard-MIT
Program in Health Sciences and Technology
in Partial Fulfillment of the Requirements for the Degree of

DOCTOR OF PHILOSOPHY IN MEDICAL ENGINEERING AND MEDICAL PHYSICS

Abstract

Within the past two decades, numerous attempts have been made to fully reconstruct bionic gait via signals derived from the human nervous system. However, human gait has been difficult to emulate due to the high resolution of both efferent and afferent signaling required to replicate coordinated volitional and reflexive motor commands. Even invasive neural interfaces providing functional feedback from the bionic leg have been unable to demonstrate biomimetic gait. To compound the difficulty, there is limited understanding of the fundamental level of afferent feedback necessary to facilitate a high degree of neuroprosthetic integration for human locomotion.

In this thesis, we investigate the impact of preserving afferent feedback in residual limbs on the sensorimotor responses of individuals with below-knee amputations. Additionally, we present a neuroprosthetic framework that fully reconstructs biomimetic gait from neural information generated by individuals with below-knee amputation. We have achieved the level of neuroprosthetic integration necessary to execute versatile gait through a surgically-constructed mechanoneural interface that enhances native muscle afferents within the amputated residuum. Finally, we develop a myoneural actuator technology in a rodent model, enabling the design of a novel mechanoneural interface that allows for the direct modulation of proprioceptive afferents. These advancements have the potential to significantly improve the quality of life for individuals with amputations and further the development of advanced surgical and neuroprosthetic technologies.

Thesis Supervisor: Hugh M. Herr, PhD
Professor of MIT Media Arts and Sciences
Director of the MIT Biomechatronics Group
Co-director of the MIT K. Lisa Yang Center for Bionics

Acknowledgments

I would like to express my deepest gratitude to Professor Hugh Herr for his invaluable guidance, support, and encouragement throughout my doctoral studies. Your dedication to my research, your patience, and your unwavering commitment to excellence have been a constant source of inspiration and motivation for me. It has been a privilege to work alongside you and learn from you.

I am grateful to my thesis committee for their invaluable guidance in shaping the narrative of this dissertation. Professors Roche and Brown, your input has been instrumental in weaving together the threads of this story. Thank you.

Robin and Seongho, thank you guys for your endless dedication to this work. This study would not have been possible without you guys. Tony, I believe we share many things. Things that are important in our lives. Always enjoyed talking to you. Guillermo, I will never forget those fun times we had at the animal facility. Perhaps we had too much fun. Erica, you taught me a value of mentoring and gave me a lesson that it is indeed bi-directional learning process. I wish you a very good luck for everything you do. Lindsey, you are the glue that makes everything work behind the scenes. Thank you for everything. To the rest of Biomech, you are all amazing. I will see you all at work.

Ben and Nathan, because of you guys, my time at HST never have been lonely. Sketchbook and beer were only things we needed to have fun. Thank you for all the inspiration and for making my days more colorful.

I thank the HST community for the welcoming home you have created for me. To the undergraduate students, thank you for your patience with me and for producing exceptional work. Additionally, I extend my gratitude to the patients who generously offered their time and energy to contribute to this research.

I would like to recognize the enormous contributions from my family. Mom and Dad, thank you so much for your support and always believing in me. Yegeun, thank you for watching my back. You have been always my hero. You guys are where all this began. Thank you!

Finally, I dedicate this thesis to my lovely wife, Yuko. You are my happiness and my peace. Thank you for holding my hands and guide me through this wonderland. I will be there for you as well, always. Love you.

Contents

List of Figures

List of Tables

Chapter 1. Introduction

Overview and Specific Aims

For many years, science fiction has imagined bionic limbs that can match the responsiveness and versatility of biological limbs. However, current technology has yet to achieve this level of sophistication[1]. The current bionics relies on intrinsic robotic architecture to simulate human gait, but without or with only partial direct nervous system control[2–12]. This is due to the complex nature of legged neuromechanics, which involves the coordinated interaction between afferent and efferent signals directed to and from the volitional supraspinal and reflexive spinal neural circuitry[13–15]. This complexity is compounded by the loss of essential locomotor peripheral afferents[16,17] that occurs during the standard-of-care amputation procedure[18]. Several previous clinical investigations have shown that bionic legs engineered to provide afferent feedback through electrical nerve stimulation can enhance gait function[19–22]. To further refine neuroprosthetic control, amputation paradigms that aim to reconfigure residual limb soft tissues have been developed, including Targeted Muscle Reinnervation (TMR)[23–25], Regenerative Peripheral Nerve Interfaces (rPNIs)[26,27], and the Agonist-antagonist Myoneural Interface (AMI) [28–30]. Each of these techniques have been demonstrated in combination with neuroprostheses for the enhancement of prosthetic control. However, such systems have yet to achieve biomimetic gait under full nervous system control. Additionally, evaluating neuroprosthetic performance is a complex process that depends on several factors, such as the subject's inherent capacities for residual limb motor control and phantom limb perception, the presence of functional feedback, and the selection of the neuroprosthetic control paradigm. Consequently, it is essential to investigate the impact of surgical residual limb reconstruction alone on clinical outcomes after amputation. Identifying subject-specific motor control and perception mechanisms post-amputation could offer valuable insights for the development of future surgical and neuroprosthetic technologies.

The objective of this thesis is to investigate the impact of preserving biological muscle dynamics and afferents on sensorimotor responses and to provide a comprehensive understanding of the required level of afferent feedback to facilitate a high degree of neuroprosthetic integration for human locomotion. Building upon these findings, the objective is to develop neuroprosthetic technologies that enable direct modulation of neural signaling to advance the level of neuroprosthetic integration. To accomplish these objectives, the thesis addresses the following specific aims:

Aim 1. To investigate free-space sensorimotor responses in individuals with below-knee amputation with varying levels of muscle dynamics preservation: The available literature falls short of providing a comprehensive understanding of the implications of retaining biomimetic muscle dynamics in the residual limb for the preservation of motor control and limb perception. This study aims to fill this gap by examining the sensorimotor responses of individuals with below-knee amputation and their correlation with the degree of residual muscle dynamics preservation. The experiments are designed to provide evidence for the proposition that the naturalness of motor control and phantom limb perception is largely influenced by and proportionate to the degree of biomimetic muscle dynamics within residual muscles post-amputation. Experiments addressing this aim are described in Chapter 2.

Aim 2. To assess the ability of neuroprosthetic gait fully driven by the human nervous system in individuals with below-knee amputation with varying levels of residual muscle afferents: The objective of this aim is to investigate the potential for restoring a fully biomimetic prosthetic gait, which is driven entirely by the human nervous system in individuals with below-knee amputation. Building upon the findings from Aim 1, which demonstrated that preserving muscle dynamics in the residuum improves free-space motor control, this study aims to explore the potential for a high degree of neuroprosthetic integration necessary for gait in individuals with biomimetic muscle dynamics preservation in the residuum. The series of experiments are designed to demonstrate the capability of bionic walking on level-ground and over various inclination angles and speeds, stair ambulation, as well as obstructed pathways. Furthermore, the study investigates residual muscle neuromechanics to quantify the level of residual muscle afferents necessary to execute versatile neuroprosthetic gait. Chapter 3 and 4 describe the experiments addressing this aim.

Aim 3. To develop a novel mechanoneural interface technology that enables direct modulation of proprioceptive afferents: Building on the findings of Aims 1 and 2, a promising avenue for directly manipulating proprioceptive afferents lies in the ability to control residual muscle stretch and contraction. Therefore, the objective of this study is to advance myoneural actuator technology and establish an interface that enables such modulation of proprioceptive afferents. The experiments conducted in Chapters 5 aims to develop and test the feasibility of this novel mechanoneural interface technology.

The present doctoral dissertation provides a comprehensive investigation of the impact of biomimetic muscle dynamics and afferents in residual limb on sensorimotor responses during free-space motor control and ambulatory tasks. Moreover, the study proposes a novel myoneural framework that could serve as a foundation for the development of future mechanoneural interfaces for enhancing neuroprosthetic integration with the human nervous system. The findings of this work could potentially contribute to the advancement of prosthetic technologies that enable more natural and intuitive neuroprosthetic control for individuals with amputations.

Background and Significance

Mechanoneural Transduction and Proprioception

Mechanoneural transduction is a fundamental principle underlying sensory feedback in the human body, where neural signaling is generated by mechanical stimuli (deformations) of sensory organs[16,17]. Proprioception, which refers to the ability to sense the relative spatial positioning of body parts and the amount of force exerted on the environment, plays a critical role in fine motor control for human locomotion[16,17]. This sensory modality is made possible by the mechanoneural transduction of sensory organs within peripheral tissues, such as muscles, tendons, joint capsules, and skin[16,31]. Among these sensory organs, muscle spindles and Golgi tendon organs are the primary mechanoreceptors that mediate proprioception by sensing muscle length, speed, and tension[16]. Such proprioceptive neural signaling relies on both microscale mechanoneural transduction and macroscale biomechanically-functional tissue architectures. In

individuals with biologically intact limbs, this architecture is realized through mechanically-coupled agonist-antagonist muscles spanning an articular joint. The physical linkage of agonist-antagonist muscles operates as a pulley-like system in which the contraction of the agonist muscle stretches its antagonist muscle. This process produces proprioceptive afferent signaling from the partner's muscle, mediated by mechanoneural transduction of sensory organs that are evoked by agonist-antagonist muscle strain (AMS).

Standard-of-Care Amputation Procedures

Current clinical amputation procedures typically result in the loss of biomimetic muscle dynamics of the biologically intact limb. In these procedures, tissues distal to the site of amputation are discarded without consideration of viable segments, while proximal residual muscles are layered over the distal transected bone to provide a stable surface for mounting a prosthesis[18]. However, this approach buries transected nerves deep in the residuum without end organs, often leading to the development of painful neuromas. Additionally, the rudimentary approximation of discordant tissues in the distal limb results in a disorganized scar mass, which destroys the biological agonist-antagonist dynamics[32]. This uncoupling of native agonist-antagonist architecture leads to isometric contraction of residual muscle groups upon volitional activation, resulting in incomplete and unbalanced proprioceptive afferent feedback to the central nervous system, thereby producing aberrant motor control and limb perception for neuroprosthetic control.

Advanced Amputation Procedures

The common approach for controlling neuroprosthetic limbs involves the utilization of electromyography (EMG)[33]. This is done by decoding EMG signals to estimate the desired joint position or torque for neuroprosthetic control. Targeted Muscle Reinnervation (TMR) has been developed to improve the quality of EMG signaling[23–25]. TMR involves redirecting residual nerves to intact muscles above the amputation level, which amplifies neural signals from residual nerves and provides an alternative muscle site for EMG-controlled neuroprosthetic limbs. TMR has demonstrated improved neuroprosthetic control compared to standard amputation and enabled multiple degree-of-freedom (DoF) neuroprosthetic control. Regenerative Peripheral Nerve Interfaces (RPNI) is another surgical intervention that offers improved neuroprosthetic control[26,27]. In contrast to TMR, RPNI involves the creation of a free graft from donor tissue that is not sourced from an otherwise normally innervated proximal muscle. Subsequently, the muscle segment is gradually re-innervated by the redirected nerve ending, which enables voluntary activation of the muscle segment in response to central nervous system (CNS). Comparable to TMR, RPNI has exhibited an ability to enhance multiple degrees-of-freedom (DoF) neuroprosthetic control among upper limb amputees. However, both TMR and RPNI do not preserve proprioception lost during amputation, which limits neuroprosthetic controllability without direct visual information or additional functional stimulation.

Agonist-antagonist Myoneural Interface (AMI)

The AMI technique involves the creation of myoneural interfaces that surgically replicate the natural agonist-antagonist muscle dynamics within the amputated residuum[28–30]. This is achieved

by physically coupling agonist-antagonist muscle pairs during amputation, such that when one muscle is neurologically triggered to contract, its partner muscle simultaneously undergoes stretching. By restoring the innate muscle dynamics, the AMI approach leverages the native sensory organs present within the residual muscles and tendons, generating biological afferents that correspond to the free-space movements of the amputated joints. For each external prosthetic joint, one AMI muscle pair is created for its neuroprosthetic control. In the case of below-knee AMI amputation, the lateral gastrocnemius (L. GAS) is mechanically linked to the tibialis anterior (TA) for prosthetic ankle control, while the peroneus longus (PL) is linked to the tibialis posterior (TP) for prosthetic subtalar control. A previous pilot study[29] has demonstrated that below-knee AMI amputation leads to improved volitional free-space and swing control compared to amputations without the AMI. However, the extent to which the preservation of agonist-antagonist muscle dynamics improves biomimetic neuroprosthetic control has not been investigated. Additionally, there has yet to be a demonstration of full neural control of versatile prosthetic gait.

Challenges in Neuroprosthetic Gait

Human gait involves a complex interplay between afferent and efferent signals that are directed to and from the volitional supraspinal and reflexive spinal neural circuitry[13–15]. However, the standard-of-care amputation procedure results in the loss of significant amounts of distal tissue, including essential locomotor peripheral afferents[18], which makes it challenging to replicate the natural gait pattern in robotic lower-extremity prostheses. Consequently, most current bionic limbs lack communication with the nervous system and rely on non-neural, intrinsic robotic control architecture using an array of intrinsic sensors[2–7], such as a finite state-machine or classification, to partially replicate human gait. Efforts to integrate neural control as a means of increasing the versatility of prosthetic devices have been made[8–12,19–22,34,35]. Electromyography (EMG) has been employed as the primary extrinsic control input to develop lower extremity prostheses capable of adapting to varying terrain[8–12,19–22]. However, the neural signals associated with ambulation for persons with traditional amputation are complicated by inconsistency[36] and unintended co-contraction[37]. To mitigate these challenges, several researchers have developed pattern-recognition-based approaches to classify user intent[8–12,19–22]. Nonetheless, these approaches are limited in their ability to fully replicate biological control, as the number of possible output states is restricted by the number of classes in the learning model. Recent attempts[34,35] to replicate biomimetic gait under continuous surface electromyography (sEMG) control have been made. However, even at a constant speed over level ground walk, these works have failed to demonstrate neural control of biomimetic gait mechanics. Furthermore, these works have not evaluated adaptation to variations in ground surfaces.

Proprioceptive Mechanoneural Interface (PMI)

This thesis introduces a novel neuroprosthetic interface, namely the Proprioceptive Mechanoneural Interface (PMI). The PMI is composed of a residual muscle-tendon and a myoneural actuator connected mechanically in series. By contracting the actuator, the residual muscle is stretched, allowing for direct control of mechanoneural transduction and modulation of proprioceptive afferents. PMI thus offers a promising approach to reproduce biomimetic

afferents. For example, in the case of bionic ankle joint control, two PMIs can be implemented for each plantar flexor and dorsiflexor. The two myoneural actuators of the PMIs can be controlled to generate biological mechanoneural transduction of each residual muscle. In contrast to AMI, which only considers agonist-antagonist muscular interactions, the muscle dynamics of biological limbs can be simulated using a virtual limb model that also accounts for external forces such as gravity and inertial forces.

Dissertation Summary

The first part of this dissertation aims to investigate the clinical implications of biomimetic free-space motor control, limb perception, and neuroprosthetic gait for individuals who underwent the AMI amputation. The objective is to understand the relationship between the degree of neuromuscular physiology preservation and sensorimotor performance after limb amputation. The second part of the dissertation focuses on developing a myoneural actuator technology that enables fatigue-resistant, long-term viable actuation for future mechanoneural interface technologies. This actuator technology has the potential to revolutionize the field of neuroprosthetics, as demonstrated by the Proprioceptive Mechanoneural Interface (PMI), which allows for direct modulation of proprioceptive afferent signals.

Chapter 2 presents a series of experiments designed to access free-space motor controllability and limb perception of individuals with transtibial amputation. The degree of muscle physiology preservation is evaluated by Agonist-antagonist Muscle Strain (AMS) through ultrasonic imaging. The collected electromyographic, goniometric, and physiological data revealed that that preserving even a marginal AMS through the AMI enables biomimetic free-space motor control and perception after amputation**.**

Chapter 3 reports that integration of autonomous bionic technologies and a mechanoneural interface, such as the AMI, enables versatile neuroprosthetic gait fully driven by the human nervous system. A computational model based on ultrasonic imaging and electromyographic assessments is used to compute the degree of afferent signaling in the residual limb. The collected data shows that even marginal augmentation of afferent signaling in the residual limb is sufficient to enable versatile neuroprosthetic gait.

Chapter 4 describes the neuroprosthetic responses to environmental perturbations during level-ground walking. The data from the perturbation trial indicate that increasing the level of afferent signaling in the residual limb through a mechanoneural interface, such as the AMI, enables fast and biomimetic gait recovery following the perturbation.

Chapter 5 presents a myoneural framework for transforming a native muscle into a fatigue-resistant myoneural actuator. The data demonstrate that the actuator's fatigue-resistance is improved while maintaining an equivalent force-mass scaling factor compared to its native form. The work further addresses the design and validation of the PMI concept in a rodent model. The data show the PMI's capability to directly modulate proprioceptive afferents through fatigue-resistant myoneural actuation.

Chapter 6 offers a comprehensive summary of the discoveries and significance of this doctoral research, which investigates human sensorimotor responses to different degrees of preserved residual afferents following amputation. Additionally, the chapter provides an overview of a new myoneural mechanism and its potential applications in the field of biohybrid systems.

Chapter 2. Preservation of biomimetic free-space motor control and perception after amputation

The investigation of the underlying mechanisms in subject-specific motor control and perception after amputation could provide valuable insights for the development of advanced surgical and neuroprosthetic technologies. This chapter focuses on studying the relationship between preserved agonist-antagonist muscle strain within the residual limb and preserved motor control and perception capacity. Fourteen individuals with unilateral transtibial amputations underwent evaluations involving free-space mirrored motions between their phantom and intact ankle-foot limbs. Previous studies have demonstrated that diverse motor control in intact limbs is achieved through the activation of muscle synergies. Here the naturalness of motor control is assessed based on extracted muscle synergies and their activation profiles from the amputee subjects. Electromyography, ultrasonography, and goniometry are used to estimate muscle synergy extraction, degree of agonist-antagonist muscle strain, and perception capacity, respectively. The data reveal significant positive correlations ($P<0.005$-0.05) between sensorimotor responses and residuum limb agonist-antagonist muscle strain. The findings suggest that preserving even 20-26% of agonist-antagonist muscle strain within the residuum compared to a biologically intact limb is effective in preserving natural motor control post-amputation. However, preserving limb perception capacity requires a higher (61%) agonist-antagonist muscle strain preservation. The results highlight agonist-antagonist muscle strain as a characteristic, readily ascertainable residual limb structural feature that can explain the variability in amputation outcome. Agonist-antagonist muscle strain preserving surgical amputation strategies such as the AMI can enable more effective and biomimetic sensorimotor control post-amputation.

Rationale and Study Design

In recent years, several amputation procedures have been developed to improve the control of neuroprosthetics through reconfiguration of residual limb soft tissues[23–27,29]. However, evaluating neuroprosthetic performance is a complex process that depends on various factors, including the subject's inherent capacities for residual limb motor control and phantom limb perception, the presence of functional feedback, and the choice of the neuroprosthetic control paradigm. Consequently, it is necessary to investigate how surgical residual limb reconstruction alone impact clinical outcomes after amputation. The identification of subject-specific motor control and perception mechanisms post-amputation could provide valuable insights for the development of future surgical and neuroprosthetic technologies. This chapter's focus is on the impact of agonist-antagonist muscle strain (AMS) preservation, a critical functional architecture for proprioceptive afferent signals[16,17], on motor control and phantom limb perception within the residual limb. It is hypothesized that enhancing levels of residual limb AMS improves motor control naturalness and proprioceptive perception in individuals who have undergone transtibial amputation. To evaluate this hypothesis, the naturalness of motor control and limb perception capacity during ankle and subtalar joint movements without visual or other functional feedback was clinically assessed. Muscle electromyography patterns and two degrees-of-freedom (2-DoF) kinetic data were collected during bilateral, mirrored movements between the intact and phantom ankle-foot limbs of each participant. For these mirrored movements, the degree of residual limb AMS was assessed using ultrasonography. Motor control naturalness and limb perception of amputees were evaluated using muscle synergy analysis[38–40], as motor control in biologically-intact limbs is executed by the activation of combinations of muscle synergies. The study findings support the hypothesis that enhancing AMS in the residual limb improves motor control naturalness and perception after amputation, highlighting the importance of surgical techniques such as the AMI that create a residuum tissue structure that preserves agonist-antagonist muscle dynamics.

Methods

Patient Selection and Clinical Evaluation

Eligibility criteria for the trial included transtibial amputee subjects between the ages of 18 and 65 who had a fully healed amputation site, were proficient in using a standard lower-extremity prosthesis, and could walk with variable cadence (K level 3 and 4[41]). Exclusion criteria consisted of underlying health conditions such as coronary artery disease, chronic obstructive pulmonary disease, and extensive microvascular compromise, as well as pregnancy and active smoking. All subjects signed informed consent forms, and all data were collected at the Massachusetts Institute of Technology (MIT). Table 1 summarizes the 14 study participants, consisting of 7 AMI subjects and 7 non-AMI control (CTL) subjects. The age range of the participants was 25 to 62 years, with a male-to-female ratio of 5:2. The subjects represented different amputation types: 7 underwent AMI amputation surgery, 6 underwent conventional amputation surgery[18], and 1 underwent Ertl osteomyoplasty[42]. AMI amputation surgeries were performed according to Partner's Institutional Review Board protocol p2014001379.

As mentioned in the introduction, the AMI transtibial amputation procedure creates mechanical linkages between two pairs of natively vascularized and innervated muscles within the residual limb, one pair for the missing ankle joint and another pair for the missing subtalar joint. The tibialis anterior (TA) is linked to the lateral gastrocnemius (GA) for the ankle joint AMI construct, and the tibialis posterior (TP) is linked to the peroneus longus (PL) for the subtalar joint AMI construct. The AMI amputation is designed to replicate physiological antagonistic actuation between the residual limb muscles to restore AMS, as shown in Figure 1a. In contrast, non-AMI amputations may disrupt AMS by severing or limiting residual agonist-antagonist muscle movements. Agonist-antagonist muscle couplings were not specifically reconstructed during standard-of-care amputation[18] or Ertl osteomyoplasty amputation[42] procedures. Therefore, the study population represented varying degrees of AMS within the residual musculature. EMG was collected simultaneously from the TA, GA, TP and PL muscles of both the residual limbs (AMI and CTL) and unaffected biologically intact limbs (BIO-A, BIO-C) (Figure 1b, 1c). A 2-DoF goniometer was also placed on the posterior aspect of the unaffected BIO limb spanning the ankle-foot complex to record mirrored movements between the intact and perceived phantom limb. Multiple motor control task instructions were provided via on-screen and audio recordings. During motor control trials, no visual or other functional feedback was provided to focus on investigating the impact of proprioceptive feedback on motor control and limb perception capacity (Figure 1b, 1c). Ultrasonography was utilized to record from the residual limbs while each subject repeated cyclic plantarflexion-dorsiflexion (PF-DF) and inversion-eversion (IN-EV) mirrored phantom limb movements (Figure 1d) to compute AMS. The maximum muscle fascicle strains were estimated from ultrasound video recordings[43,44] (Figure 1e), which were further normalized by the nominal muscle fascicle strain ranges from a computational musculoskeletal limb model[45]. The average PF-DF and IN-EV AMS values were used to represent the degree of AMS within the residuum. The degree of AMS ranges from 0 to 1, where zero indicates that the subject preserved none of the AMS present in the biologically intact limb, and 1 indicates fully preserved biological AMS.

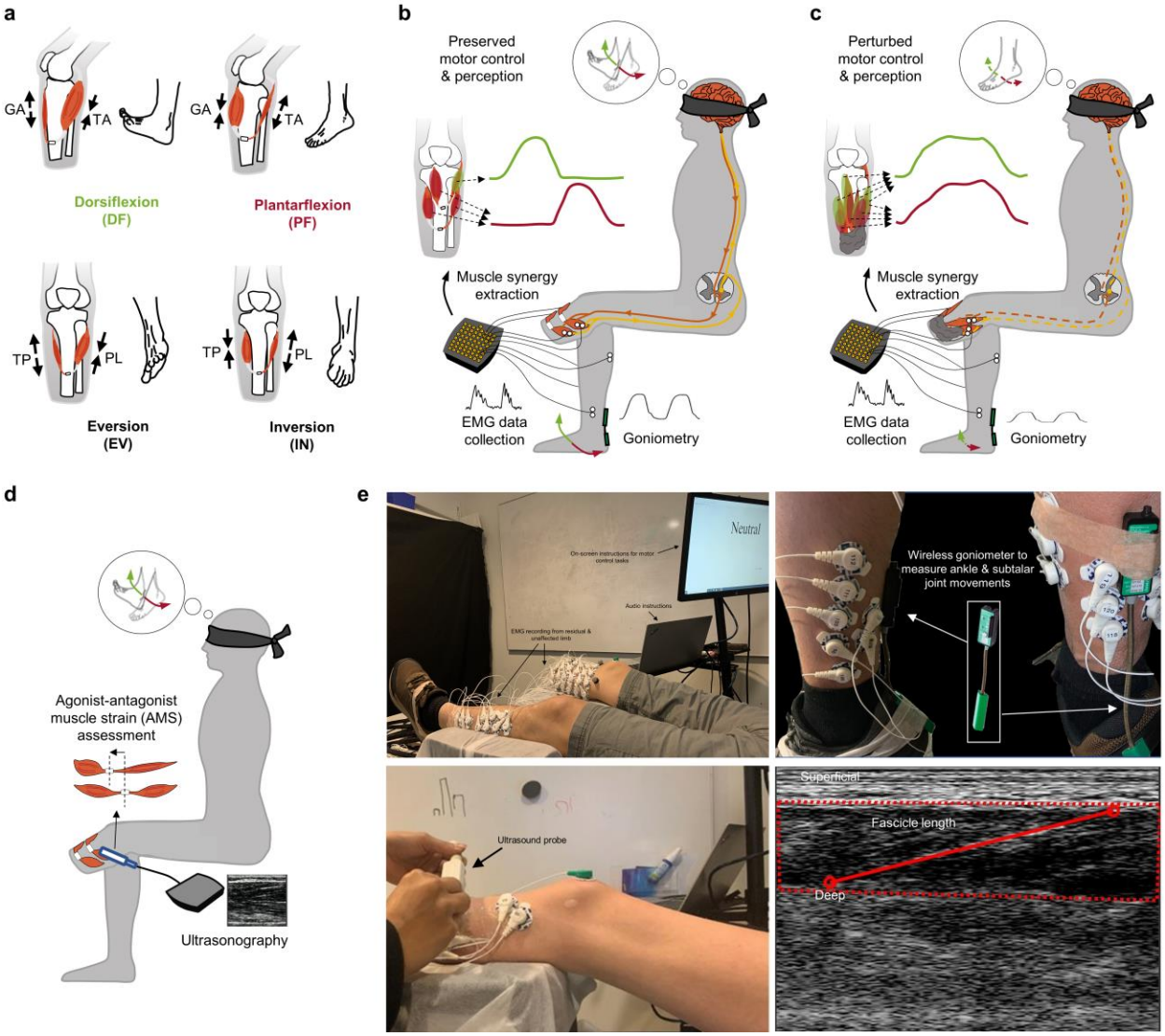

Figure 1 | Clinical evaluation of sensorimotor responses and the degree of agonist-antagonist muscle strain (AMS) for participant's residual limb muscles. a, Shown is the AMI amputation seeks to emulate physiological actuation of antagonistic muscle contraction and stretch. Ankle and subtalar AMI constructs are devised to create direct agonist-antagonist coupling for ankle dorsi and plantarflexion and for subtalar eversion and inversion. **b**, **c**, the experimental setup is shown for AMI (**b**) and CTL (**c**) cohorts. Motor control and phantom limb perception capacity are assessed in free space without visual feedback or any other functional feedback. Perturbed motor control and perception are anticipated if a critical degree of AMS is not preserved in the limb (**c**). Representations of the dorsi and plantarflexion synergic motor outputs are shown in green and red, respectively; efferent and afferent neural signals are shown in brown and yellow, respectively. Eversion and inversion were also tested but are not shown here. **d**, AMS is computed from muscle fascicle changes during cyclic phantom ankle and subtalar joint movements. **e**, Shown is the experimental setup for clinical evaluations.

Table 1 | Study population

Subject ID	Amputation type	Age (years)	Time since amputation (years)	Amputation etiology	Biological sex	Height (m)	Weight (kg)
AMl-1/BIO-A1	AMI	43	1.6	Thermal Injury	Female	1.68	81
AMl-2/BIO-A2	AMI	55	2.7	Trauma	Male	1.73	77
AMl-3/BIO-A3	AMI	50	1.0	Trauma	Female	1.68	81
AMl-4/BIO-A4	AMI	58	1.2	Trauma	Male	1.90	93
AMl-5/BIO-A5	AMI	32	0.5	Trauma	Male	1.75	75
AMl-6/BIO-A6	AMI	29	0.6	Trauma	Male	1.68	84
AMl-7/BIO-A7	AMI	48	0.5	Trauma	Male	1.70	75
CTL-1/BIO-C1	Standard	25	1.4	Oncological	Female	1.64	54
CTL-2/BIO-C2	Standard	62	2.7	Trauma	Female	1.65	81
CTL-3/BIO-C3	Standard	25	2.0	Talipes Equinovarus	Male	1.78	108
CTL-4/BIO-C4	Standard	39	2.7	Trauma	Male	1.60	63
CTL-5/BIO-C5	Ertl OM	62	2.6	Trauma	Male	1.80	97
CTL-6/BIO-C6	Standard	61	5.3	Trauma	Male	1.73	91
CTL-7/BIO-C7	Standard	46	8.7	Trauma	Male	1.78	75
Mean±s.d.		45±14	2.4±2.2			1.72±0.08	81±14

Agonist-antagonist Myoneural Interface (AMI); Residual limbs of participants who underwent an AMI amputation (AMI 1-7); Residual limbs of participants who underwent a Non-AMI control amputation (CTL 1-7); Unaffected biologically-intact limbs (BIO A1-A7 and BIO C1-C7). Ertl OM, Ertl osteomyoplasty

Surface Electrodes Placements and EMG Processing

Bipolar surface electrodes were used to record EMG from the lateral gastrocnemius (GA), tibialis anterior (TA), tibialis posterior (TP), and peroneus longus (PL) muscles of both the residuum and unaffected limb. The electrode placement was guided by ultrasound imaging when necessary (Figure 1e). The EMG signals were processed offline by applying a high-pass filter (fourth-order zero-lag Butterworth filter, 20 Hz cut-off frequency) and then full-wave rectified. A low-pass filter (fourth-order zero-lag Butterworth filter, 5 Hz cut-off frequency) was then applied to compute the muscle activation patterns. To account for inter-subject differences, all EMG signals were normalized to calibrated maxima for each muscle.

Muscle Synergy Extraction and Synergy Activation Profile

To evaluate the motor control of residual limbs, muscle synergy extraction was performed using muscle activation patterns during discrete ankle and subtalar joint movements (Figure 2). The study involved subjects performing sequential movements of PF, IN, DF, and EV for both the residual (phantom) and intact limbs. The order of the movement trials was not randomized to accurately identify the motor capabilities for these four principal movements. Each discrete movement was repeated 40 times. A widely accepted mathematical model[40] was used to represent motor outputs as muscle synergy combinations as

$$\boldsymbol{m}(t) = \sum_{i=1}^{N} c_i(t)\, \boldsymbol{w}_i + \varepsilon(t) \qquad \text{Eq. 1}$$

where $\boldsymbol{m}(t)$ is the muscle activation patterns at time *t*; $\boldsymbol{w}_i$is the *i*-th muscle synergy vector; $c_i(t)$ is the time-varying coefficient, or synergy activation, for *i*-th muscle synergy vector; *N* is the total number of muscle synergy vectors composing the muscle activation patterns; and $\varepsilon(t)$ is the residual. The model represents muscle activation patterns as linear combinations of a set of time-invariant muscle synergy vectors that are activated by time-varying coefficients. In the field, $\boldsymbol{w}_i$ is generally accepted as a muscle synergy profile with a structural basis in the nervous system and $c_i(t)$ is considered an index of motor commands or synergy activations. Muscle synergies were extracted using the non-negative matrix factorization (NMF) algorithm[46]. The NMF started with the initialization of time-varying coefficients and muscle synergy vectors to random positive values in the [0 1] interval. The goodness of fit metric of decomposed matrices was evaluated by variance accounted for (VAF)[47]. The NMF was continued until the change in VAF in 50 consecutive iterations was less than a tolerance of 1×10^{-5}. To reduce the probability of finding a local minimum solution for the NMF optimization, the same procedures were repeated 30 times with different sets of initial conditions, and the solution with the highest VAF was selected. The number of muscle synergies was selected as the least number of synergies that could adequately reconstruct the muscle activation patterns, as determined by VAF > 0.95[47]. To enable intrasubject comparisons of motor commands, the average vectors of synergy activation profiles $\boldsymbol{u}_{\text{task}}$ were used, or

$$\boldsymbol{u}_{\text{task}} = \sum_{i=1}^{N} \frac{\int_0^{T_{\text{task}}} c_i(t)dt}{T_{\text{task}}} \hat{\boldsymbol{n}}_i \qquad \text{Eq. 2}$$

where $\hat{\boldsymbol{n}}_i$ is a unit vector in synergy space indicating activation of synergy vector $\boldsymbol{w}_i$**;** T_{task} is a time period of a given task. To identify motor commands for PF, DF, IN, and EV, the muscle activation patterns for each discrete movement were gathered and synergy activation vectors were computed independently. The synergy activation vectors were then normalized for further analysis.

Naturalness of Muscle Synergy and Synergy Activation

The naturalness of the muscle synergy and synergy activation profiles of the AMI and CTL groups was quantified by computing their similarities to the average normalized values of the BIO group. To determine which muscle synergy of one subject corresponded to a muscle synergy of another subject, the maximum scalar product was identified among others. After sorting the muscle synergy vectors, the representative muscle synergy vectors of the BIO group were determined as the normalized average muscle synergy vectors of the BIO group. The naturalness of one's muscle synergy was calculated by plotting the mean scalar products with the representative of the BIO group. Similarly, the naturalness of one's synergy activation vectors was calculated by plotting the mean scalar products with the normalized average synergy activation vectors of the BIO group. A leave-one-out procedure was used for computing the dot products of the BIO group. The number of universal synergy vectors for similarities analysis was set to 3, which was the number of synergy vectors of all subjects in the BIO group. If fewer synergy vectors were identified previously by the synergy extraction procedures, *0* vectors were added to muscle synergy and synergy activation vectors to match the dimensionality of vectors.

Robustness of Synergy Activation

The robustness of ankle and subtalar volitional control was quantified based on the degree of decoupling between synergy activations for different target movements (Figure 3). The angle between two average vectors of synergy activations for two different target movements was used to indicate the tolerance to variance in motor commands of the corresponding targeted movements. If the tolerance of motor commands is larger than the expected variance, it indicates that a subject can reliably produce distinguishable synergy activation for two discrete movements of interest. Therefore, the margin of synergy activation is given as

$$\emptyset_{ij} = \operatorname{acos}\left(\boldsymbol{u}_i^T \cdot \boldsymbol{u}_j\right) - \frac{1}{T_{\text{task},i}} \int_0^{T_{\text{task},i}} \left| \operatorname{acos}\left(\boldsymbol{u}_i^T \cdot \frac{\boldsymbol{c}_i(t)}{\| \boldsymbol{c}_i(t) \|}\right)\right| dt - \frac{1}{T_{\text{task},j}} \int_0^{T_{\text{task},j}} \left| \operatorname{acos}\left(\boldsymbol{u}_j^T \cdot \frac{\boldsymbol{c}_j(t)}{\| \boldsymbol{c}_j(t) \|}\right)\right| dt \quad (i \neq j,\ i,j \in \{\text{PF}, \text{DF}, \text{IN}, \text{EV}\}) \qquad \text{Eq. 3}$$

where $\emptyset_{ij}$ is the margin in synergy activations to have distinguishable patterns between targeted *i* and *j* discrete movements; $T_{\text{task},i}$ is the interval time of *i* discrete movement. Note that the initial term on the right-hand side of the equation represents the angle between the average vectors of synergy activation, which is indicative of the degree of tolerance to variance in motor commands between two different targeted movements. Meanwhile, the second and third terms correspond to the variability in motor commands for the two discrete movements in question. A threshold of 0 was chosen for the margin of synergy activation to determine the robust decoupling of these distinct movements.

Synergy Space ($\boldsymbol{U_S}$-space) and Motor Intent Decoding ($\boldsymbol{\alpha}$-space)

The motor intents were decoded from arbitrary muscle activation patterns using the extracted muscle synergy and synergy activation average vectors of the four principal movements (PF, DF, IN, EV). To accomplish this, the time-varying coefficients of the arbitrary muscle activation patterns were decomposed using a revised NMF[48], with the synergy vectors fixed as the extracted muscle synergy from discrete movement trials during NMF iterations. The same initialization and iteration protocols were employed as those of the muscle synergy extraction procedures for the remainder of the decomposition procedures. Using this revised NMF, the arbitrary muscle activation patterns were reflected into the muscle synergy space of the discrete ankle and subtalar joint movements. The reflected time-varying coefficients at time t, $\boldsymbol{U}_{\text{S}}(t)$, were further decoded into motor intents of ankle and subtalar movements using the synergy activation vector of the four discrete movements, namely $\boldsymbol{u}_{\text{PF}}$, $\boldsymbol{u}_{\text{DF}}$, $\boldsymbol{u}_{\text{IN}}$, and $\boldsymbol{u}_{\text{EV}}$, as

$$\alpha_{\text{PFDF}}(t) = \frac{1}{\operatorname{acos}\left(\boldsymbol{u}_{\text{PF}}^T \cdot \boldsymbol{u}_{\text{DF}}\right)} \left(\operatorname{acos}\left(\boldsymbol{u}_{\text{PF}}^T \cdot \frac{\boldsymbol{U}_{\text{S}}(t)}{\| \boldsymbol{U}_{\text{S}}(t) \|}\right) - \operatorname{acos}\left(\boldsymbol{u}_{\text{DF}}^T \cdot \frac{\boldsymbol{U}_{\text{S}}(t)}{\| \boldsymbol{U}_{\text{S}}(t) \|}\right)\right) \qquad \text{Eq. 4}$$

$$\alpha_{\mathrm{INEV}}(t) = \frac{1}{\operatorname{acos}(\boldsymbol{u}_{\mathrm{IN}}^{T} \cdot \boldsymbol{u}_{\mathrm{EV}})} \left(\operatorname{acos}\left(\boldsymbol{u}_{\mathrm{IN}}^{T} \cdot \frac{\boldsymbol{U}_{\mathrm{S}}(t)}{\| \boldsymbol{U}_{\mathrm{S}}(t) \|}\right) - \operatorname{acos}\left(\boldsymbol{u}_{\mathrm{EV}}^{T} \cdot \frac{\boldsymbol{U}_{\mathrm{S}}(t)}{\| \boldsymbol{U}_{\mathrm{S}}(t) \|}\right)\right) \qquad \text{Eq. 5}$$

where α_{PFDF} and α_{INEV} indicate directions of desired movements in ankle and subtalar DoF, respectively. Given these definitions, α_{INEV} and α_{PFDF} ranges from -1 to 1 and the α-space consists of α_{INEV} and α_{PFDF} served as a phase domain of motor control. The universal dimensionality of decomposed $\boldsymbol{U}_{\mathrm{S}}$ was unified as 3, which was the dimensionality of decomposed $\boldsymbol{U}_{\mathrm{S}}$ of all subjects in the BIO group. When fewer synergy vectors were identified previously by synergy extraction procedures, $\boldsymbol{0}$ vectors were added in $\boldsymbol{U}_{\mathrm{S}}$ to match dimensionality of vectors.

2-DoF Motor Controllability

Simultaneous multi-DoF motor controllability was quantified by investigating the transitions in directionality of motor intent during 10 cycles of the drawing-a-circle tasks (Figure 3). The $\boldsymbol{U}_{\mathrm{S}}$ was first reflected into α-space. To draw an ideal circle in joint space, the directionality of motor intent in both ankle and subtalar DoF needs to be changed simultaneously, resulting in diagonal trajectory in α-space. If the subject is only able to perform a single DoF motor control at a time, only changes in α_{INEV} or α_{PFDF} is found at a time, resulting in horizontal or vertical trajectory in α-space. Therefore, 2-DoF motor controllability was calculated by integrating diagonal components of trajectories within α-space to evaluate the simultaneous multi-DoF motor controllability, or

$$\text{2-DoF motor controllability} = 1 - \frac{1}{\pi} \sum_{j=1}^{4} \sum_{i=1}^{n_j} \frac{1}{T_{\mathrm{E},i}^{j} - T_{\mathrm{S},i}^{j}} \int_{T_{\mathrm{S},i}^{j}}^{T_{\mathrm{E},i}^{j}} \operatorname{acos}\left(\boldsymbol{\delta}_{11} \cdot \frac{|\dot{\boldsymbol{\alpha}}|}{\|\dot{\boldsymbol{\alpha}}\|}\right) dt \qquad \text{Eq. 6}$$

where n_j is the number of trajectories in *j*-th quadrant of α-space; $T_{\mathrm{S},i}^{j}$ and $T_{\mathrm{E},i}^{j}$ indicate the start and end time of *i*-th trajectory in *j*-th quadrant, respectively; $\dot{\boldsymbol{\alpha}}$ and $\boldsymbol{\delta}_{11}$ are a velocity vector in α-space and unit diagonal vector, given as $[\frac{1}{\sqrt{2}}, \frac{1}{\sqrt{2}}]$, respectively. The trajectories in α-space were analyzed independently for each quadrant to assess the multi-DoF motor controllability of different combinations of discrete movements. The average diagonal components of the trajectories in each quadrant were computed and normalized by $\frac{\pi}{4}$. The mean values of the diagonal components of all quadrants were then calculated. If a quadrant did not contain any trajectories, the diagonal component for that quadrant was considered as zero. Note that the second term on the right-hand side of the equation approaches zero, and 2-DoF motor controllability becomes 1 when all trajectories in all quadrants are solely composed of diagonal components. Based on this definition, 2-DoF motor controllability is bounded between 0 and 1.

Evaluation of Spatiotemporal Motor Control under Time Constraints

The study evaluated spatiotemporal motor control through two metrics: motor control performance and economy of motion, under increasing time constraints ranging from 2.0 seconds to 0.5 seconds (Figure 4). An index of difficulty (ID) was calculated for each time constraint by computing the logarithm of the inverse of the time constraint and scaling it to range from 0 to 1

($ID_{2.0}$-$ID_{0.5}$), inspired by Fitts' law[49–51]. The speed-accuracy tasks consisted of 10 repetitions of discrete movements (PF, DF, IN, and EV) in a random order for each of the five time-interval settings. The motor control performance was assessed by analyzing the tracking errors between the decoded motor intent $\boldsymbol{\alpha}$ and the ideal targets of the *j* discrete movements $\boldsymbol{\chi}_j$ in $\boldsymbol{\alpha}$-space, as

$$\text{motor control performance} = 1 - \frac{1}{2(T_\text{E} - T_\text{S})} \int_{T_\text{S}}^{T_\text{E}} |\boldsymbol{\chi}_j - \boldsymbol{\alpha}(t)| dt \,. \qquad \text{Eq. 7}$$

Ideal target movements in α-space $\boldsymbol{\chi}_\text{PF}$, $\boldsymbol{\chi}_\text{DF}$, $\boldsymbol{\chi}_\text{IN}$, and $\boldsymbol{\chi}_\text{EV}$ were defined as (0, -1), (0, 1), (-1, 0), and (1, 0), respectively. The motor control performance, as defined here, reflects one's ability to maintain motor intent for a given motor task. Meanwhile, economy of motion was assessed by calculating the ratio of effective synergy activation for the targeted *j* discrete movements to the total synergy activation, or

$$\text{economy of motion} = \frac{1}{T_\text{E} - T_\text{S}} \int_{T_\text{S}}^{T_\text{E}} \frac{|\alpha_j(t)|}{\|\boldsymbol{\alpha}(t)\|} dt \qquad \text{Eq. 8}$$

where α_j is effective synergy activation for targeted *j* discrete movements, determined as α_PFDF for PF and DF and α_INEV for IN and EV. The economy of motion, as defined, reflects the straightness of trajectories produced to achieve the targeted discrete movements.

Assessment of Phantom Limb Perception Capacity

To assess limb perception capacity of phantom limbs across their full perceived ranges of motion (ROM) for DF-PF and IN-EV, a psychometric task was employed (Figure 5). The subjects' mirrored perceived phantom limb positions were measured by goniometry from their BIO limb and were normalized by the BIO limb ROM ($\hat{\theta}$) to allow comparison with the intended phantom limb positions (θ) assessed from the EMG data. The intended limb position was evaluated using the average value of $\| \boldsymbol{U}_\text{S} \| \alpha_\text{PFDF}$ and $\| \boldsymbol{U}_\text{S} \| \alpha_\text{INEV}$ for each movement, which reflects both the direction and amplitude of desired movements. To vary the phantom limb position while considering the range of motion of each joint, the subjects performed separate, randomized PF and DF trials at 25%, 50%, 75%, and 100% of their PF and DF ROM (40 trials each), as well as randomized IN and EV trials at 50% and 100% of their ROM (30 trials). Limb perception capacity was estimated based on the relationship between the intended phantom limb positions and the mirrored perceived phantom limb positions, which was determined as the mean value of the ranges between 5% and 95% of the psychometric functions. If a subject reported either zero phantom limb sensation or inconsistent phantom limb sensation to the intended limb positions, their limb perception capacity was considered zero. When the psychometric function did not reach 5% or 95%, the minimum or maximum value of the function was selected.

Assessment of Phantom Limb Sensations

The study evaluated the phantom limb sensation scores based on the vividness of the phantom limb sensations compared to the actual sensations of the intact limb during ankle, subtalar, and ankle/subtalar joint rotations. The subjects provided self-reported scores on a 0-to-10 scale, with

0 indicating no sensation and 10 indicating equivalent sensations between the phantom joint and the intact limb.

Statistics

The sample size was not predetermined using statistical methods, but effect sizes for the main outcomes were determined using Cohen's *d* values ranging from 1.26 to 1.35. The data collection and analysis were not blinded to the experimental conditions. The unaffected limbs of all subjects served as the biologically intact limb population when appropriate, and no separate non-amputated subjects were recruited. Six sensory-motor response variables were analyzed to assess the degree of AMS for the pooled dataset of all 14 subjects' residual limbs (CTL-1-7 and AMI-1-7). A non-parametric correlation, Kendall's tau (τ), and *P*-value were used to determine the positive association between each response variable and the degree of AMS. A first-order exponential response curve was fitted to determine the critical degree of AMS (AMS_c) that preserves 95% of each sensory-motor response variable. The Jackknife mean $\pm$ standard deviation (s.d.) of AMS_c and R^2 values of the fitted response curve for each response variable were reported. The normality of the motor control data was tested using a Shapiro-Wilk test at a significance level of $\alpha = 0.05$. To account for within-subject limb differences (AMI:BIO-A and CTL:BIO-C), paired one-tailed *t* tests were used at a significance level of $\alpha = 0.05$, as all motor control data did not violate the data normality assumption. To account for between-subject residual limb differences (AMI:CTL), unpaired two-tailed *t* tests were used at a significance level of $\alpha = 0.05$. Interactive effects between limb subgroups (AMI:CTL x affected:unaffected limb) were analyzed using 2-way ANOVA at a significance level of $\alpha = 0.05$.

Results

Naturalness of Motor Control

Figure 2a-2c display the muscle synergies and average vectors of synergy activation profiles, respectively, for all 28 limbs during discrete motor tasks (PF, DF, IN, EV). All BIO-A, BIO-C, AMI, and 4/7 CTL limbs indicated three muscle synergies performing four principal ankle and subtalar movements. All BIO and AMI limbs shared common muscle synergies; one synergy ($\boldsymbol{W}_1$) was dominated by GA and TP muscle activations, and the other two synergies ($\boldsymbol{W}_2$ and $\boldsymbol{W}_3$) were respectively dominated by PL and TA activations. However, muscle synergies were altered in 5/7 CTL limbs as follows: CTL-1-4 all differed from BIO limbs in $\boldsymbol{W}_2$ or $\boldsymbol{W}_3$, showing coactivation tendencies. CTL-2-4, and CTL-6 also differed from BIO limbs in $\boldsymbol{W}_1$, showing altered GA and TP coordination profiles.

The muscle synergy similarity (m.s.s.) and synergy activation similarity (s.a.s.) between each subject's residual limb and the average profiles across all 14 subjects' biologically intact limbs was plotted against the degree of AMS (Figure 2d, 2e). Both trends showed significant positive associations (m.s.s.: $\tau = 0.54$, $P < 0.01$; s.a.s.: $\tau = 0.56$, $P < 0.005$). Relatively low values of the critical degree of AMS (AMS_c) were anticipated to preserve 95% of natural discrete motor control for the residual limb (m.s.s.: $AMS_c = 0.21$, $R^2 = 0.94$; s.a.s.: $AMS_c = 0.22$, $R^2 = 0.84$).

These results provide evidence that the degree of AMS within residual muscles enables natural, discrete motor control.

Further analyses (Figure 2f, 2g) found significant differences for AMI:CTL comparisons (m.s.s.: $t = 3.30$, $P < 0.01$, s.a.s.: $t = 2.99$, $P < 0.02$), significant differences for CTL:BIO-C comparisons (m.s.s.: $t = 3.37$, $P < 0.01$, s.a.s.: $t = 3.27$, $P < 0.01$), and no significant differences for AMI:BIO-A comparisons (m.s.s.: $t = 0.48$, $P = 0.33$, s.a.s.: $t = 1.79$, $P = 0.06$). Subgroup analyses amongst the 28 limbs revealed significant interactive effects (AMI:CTL × affected:unaffected limb) for muscle synergy similarity and synergy activation similarity (m.s.s: $F = 10.68$, $P < 0.005$, s.a.s.: $F = 9.22$, $P < 0.01$). These results suggest that advanced amputation procedures that actively preserve even a small degree of AMS may effectively preserve natural discrete motor control after amputation.

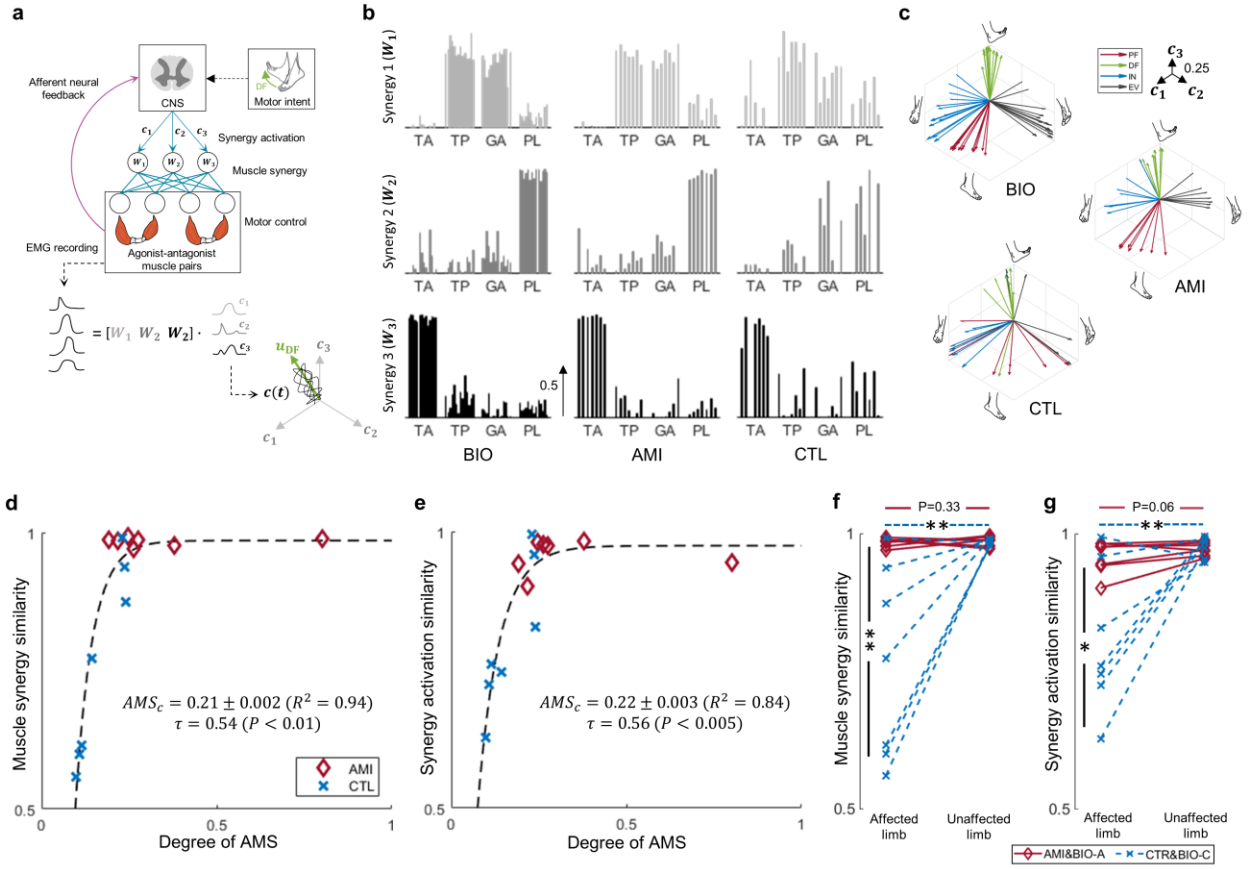

Figure 2 | Naturalness of motor control. a, the framework of muscle synergies is shown. Varied motor control is executed by the activation of combinations of muscle synergies. **b**, the extracted muscle synergies of all 28 limbs are shown (BIO: $n = 14$, AMI: $n = 7$, CTL: $n = 7$). **c**, the average vectors of synergy activation profiles are shown. These vectors were derived from the muscle synergies found during discrete motion testing of all 28 limbs (BIO: $n = 14$, AMI: $n = 7$, CTL: $n = 7$). Each axis (c_1-c_3) indicates the activation of a muscle synergy ($\boldsymbol{W}_1$-$\boldsymbol{W}_3$). Here the four different colors indicate the movements. **d, e**, the relationships between m.s.s. and s.a.s. are shown with the degree of AMS in a combined analysis of affected AMI and CTL limbs ($n = 14$). Reported are the Kendall's tau (τ), P, R^2, the Jackknife mean, and s.d. for AMS_c. **f, g**,

comparisons are shown of individual and interactive effects (AMI:CTL × affected:unaffected limb) for muscle synergy similarity (m.s.s.) and synergy activation similarity (s.a.s.) for all 28 limbs. Here paired one-tailed *t* tests were used for BIO-A:AMI and BIO-C:CTL comparisons, unpaired two-tailed *t* tests were used for the AMI:CTL comparison, and 2-way ANOVA was used for the interaction analysis (**P*<0.05, ***P*<0.01). Where no significance is seen, a *P* value for the comparison is shown.

Robust Multi-Degrees-of-Freedom Motor Control

The ability to consistently and cohesively control movement without visual or other feedback is important for enabling stable neural signaling, which is critical for neuroprosthetic control. This section aimed to evaluate the robustness of motor control for ankle and subtalar joint movements by analyzing the variability in synergy activation profiles for each movement (Figure 3a). The results showed that synergy activation profiles varied for different movement tasks, and all BIO-A, BIO-C, and AMI limbs were able to produce four distinct synergy activations for ankle and subtalar joint movements (Figure 3b). However, only 3 out of 7 CTL limbs were able to produce the same number of distinct synergy activations.

In order to evaluate the ability to control multiple degrees of freedom (DoF) simultaneously, the study asked participants to attempt to "draw a circle" while mirroring the movement of their phantom foot and biologically intact foot by controlling their ankle and subtalar joints. Muscle activations were measured and then decoded into synergy activations (Figure 3c, $\boldsymbol{U}_S$) using a matrix decomposition technique and previously identified muscle synergies ($\boldsymbol{W}_1$-$\boldsymbol{W}_3$). Motor intents were computed from the synergy activations based on the average vectors of synergy activation profiles of the 4 principal ankle and subtalar joint movements, and transformed into the α-space to present the directions of desired movements. When the circle was drawn with ankle and subtalar movement transitions in concert, the directionality of motor intents for ankle and subtalar joints changed simultaneously, resulting in diamond-type trajectories consisting of diagonals in α-space (Figure 3d, 3e). The 2-DoF motor controllability of each limb was quantified by computing the mean value of the diagonal components of traces in α-space. The plotted 2-DoF motor controllability against the degree of AMS (Figure 3f) revealed significant positive associations (τ = 0.58, P < 0.005), and a relatively low value of AMS_c (AMS_c= 0.26, R^2= 0.89) was expected to maintain 95% of 2-DoF motor controllability for the residual limb. The analysis also demonstrated significant interactive effects (Figure 3g, F = 12.22, P < 0.005) for 2-DoF motor controllability between amputation subgroups and limb categories (AMI:CTL × affected:unaffected limb). Notably, significant differences in 2-DoF motor controllability were observed between CTL and BIO-C limbs (t = 3.25, P < 0.01) and between AMI and CTL limbs (t = 3.42, P < 0.01), while no significant difference was noted between BIO-A and AMI limbs (t = 0.60, P = 0.28).

In summary, our findings indicate that the presence of AMS within residual muscles enhances the decoupling and stabilization of motor behaviors for discrete ankle and subtalar joint movements, enabling robust, simultaneous 2-DoF motor control of the residual limb without relying on visual or other functional feedback. Additionally, our results suggest that amputation

techniques that actively preserve biological AMS may effectively maintain multi-DoF motor control after amputation.

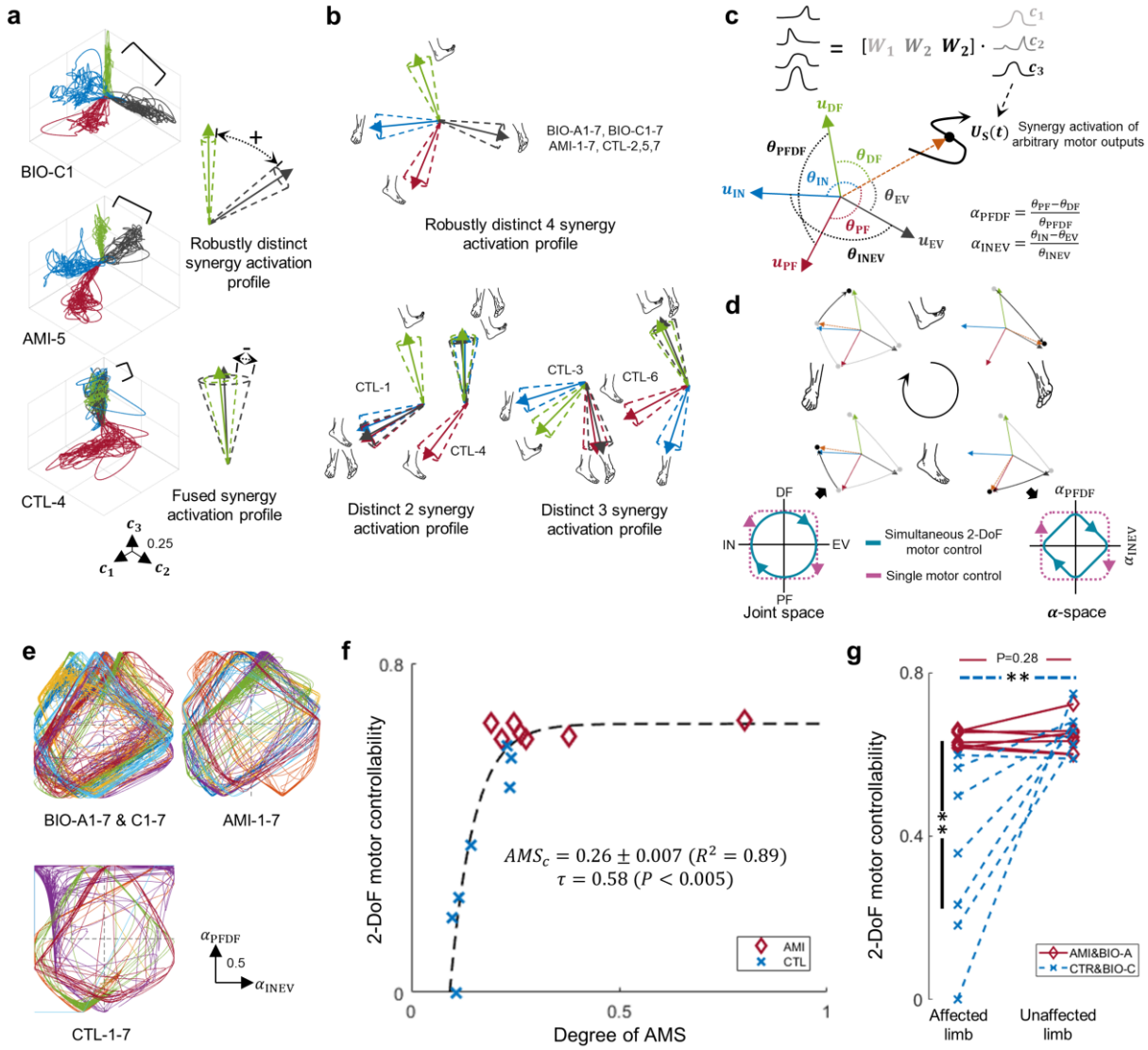

Figure 3 | Multi-degree-of-freedom motor control. **a**, Representative data are plotted that were collected during testing of the 4 discrete movements, and an illustration of robustly distinct and fused synergy activation profiles are shown. **b**, Illustrations of the 4 discrete joint movements and the degree of decoupled motor behaviors are shown for different synergy activation profiles. **c**, Shown are diagrams of the α-space transformation used to decode motor intention of an arbitrary motor output ($\boldsymbol{U}_S$) from the average vectors of synergy activation profiles for the 4 discrete movements ($\boldsymbol{u}_{PF}, \boldsymbol{u}_{DF}, \boldsymbol{u}_{IN}, \boldsymbol{u}_{EV}$). Directionality of motor intentions (α_{PFDF} and α_{INEV}) are computed based on angles between $\boldsymbol{U}_S$, $\boldsymbol{u}_{PF}, \boldsymbol{u}_{DF}$, $\boldsymbol{u}_{IN}$, and $\boldsymbol{u}_{EV}$. **d**, Shown is the illustration of the draw-a-circle test and the relationship between joint space and α-space. Simultaneous 2-DoF motor controllability of ankle and subtalar joints is defined as changes in

both α_{PFDF} and α_{INEV} resulting in diamond-type trajectories in α-space; single DoF motor control is defined as a change in either α_{PFDF} or α_{INEV}. **e**, Motor intention trajectories are shown in α-space for all 28 limbs (BIO-A & BIO-C: n = 14, AMI: n = 7, CTL: n = 7) during draw-a-circle trials. Distinct colors were superimposed indicating the different subjects. **f**, The relationship between 2-DoF motor controllability and the degree of AMS is shown in a combined analysis of affected AMI and CTL limbs (n = 14). Kendall's tau coefficients (τ), P, R^2, and the Jackknife mean and s.d. for AMS_c are reported. **g**, Comparison of individual and interactive effects (AMI:CTL × affected:unaffected limb) for 2-DoF motor controllability for all 28 limbs are shown. Paired one-tailed t-tests were used for BIO-A:AMI and BIO-C:CTL comparisons, unpaired two-tailed *t* tests for AMI:CTL comparisons, and 2-way ANOVA was used for the interaction analysis (**P<0.01). Where no significance is seen, a P value for the comparison is shown.

Spatiotemporal Motor Control under Time Constraints

In this section, the impact of AMS within residual muscles on spatiotemporal motor control under time constraints was investigated through speed-accuracy motor tasks, also known as Fitts' law-type motor tasks[49–51] (Figure 4a). In Figure 4b, the successful performance of speed-accuracy motor tasks by AMI-1 can be observed through the distinct synergy activations produced for each target motor task. In contrast, CTL-2 required a longer time interval ($\mathrm{ID}_{2.0}$ or $\mathrm{ID}_{1.5}$) to perform the tasks successfully, as demonstrated by the loss of boundaries between the four targets with increasing time constraints ($\mathrm{ID}_{1.0}$-$\mathrm{ID}_{0.5}$). Motor control performance demonstrated a significant positive association (τ = 0.61 $\pm$ 0.07, P < 0.01) with the degree of AMS across all IDs (Figure 4c, 4d). The economy of motion was also evaluated by examining the trajectory straightness of the synergy activations during targeted movement tasks. The results showed a significant positive association between the economy of motion responses and the degree of AMS (τ = 0.49$\pm$0.02, P < 0.05) (Figure 4e, 4f).

The findings suggest that a higher degree of preserved AMS can lead to more efficient and economical motion during spatiotemporal motor tasks for individuals with amputation. On the other hand, individuals with limited AMS exhibited less efficient and more wandering motion during spatiotemporal motor control performance tasks, indicating the importance of AMS in motor control. It is possible that the afferent feedback provided by residual limb AMS can help reduce tremors in neuroprosthetic control in the absence of visual or other functional feedback. Further discussion on this topic will be presented in the Discussion section.

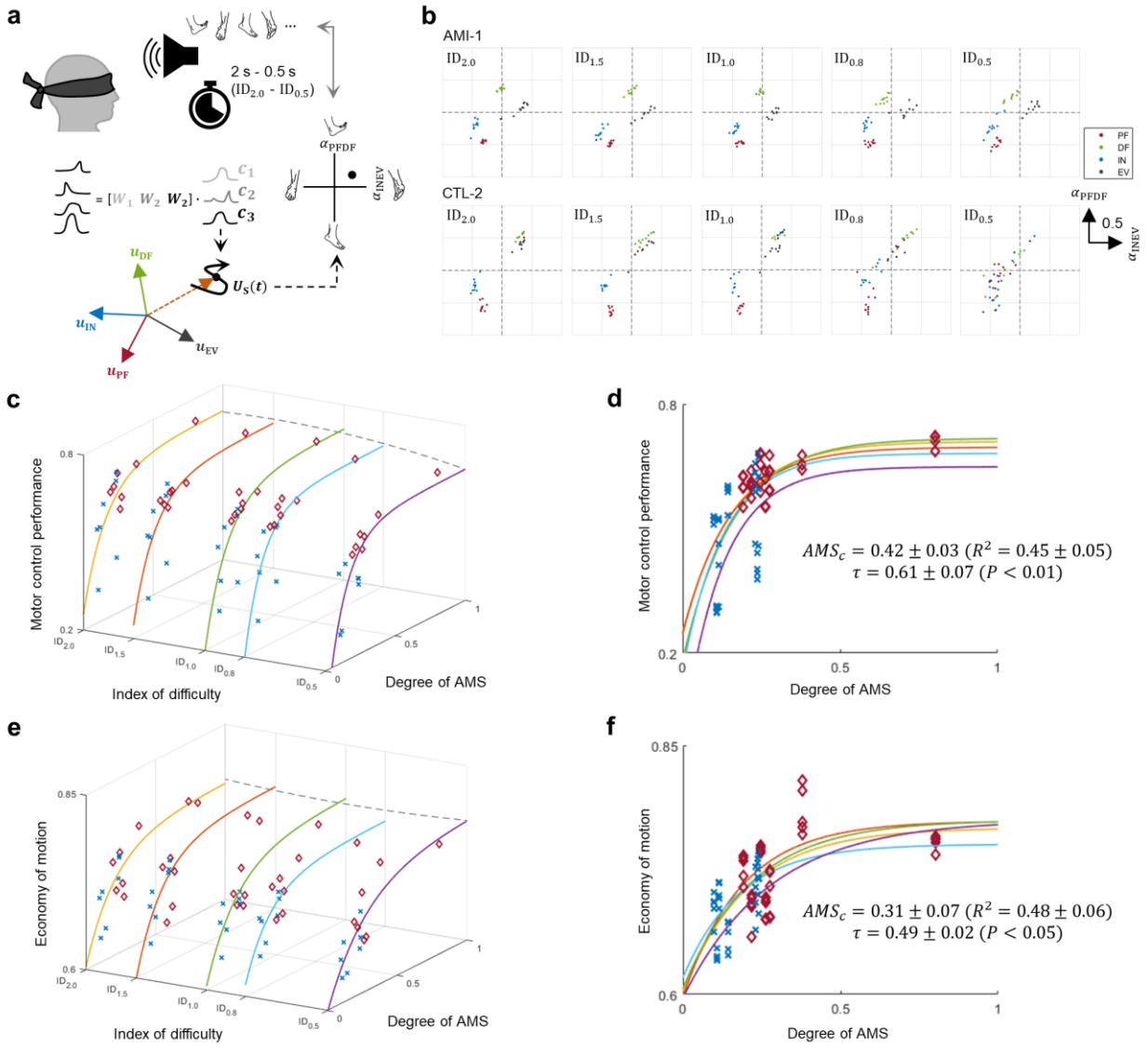

Figure 4 | Spatiotemporal motor control under time constraints. a, An Illustration is shown of a subject performing randomized, discrete ankle and subtalar joint motion tasks under varying time constraint (2 s – 0.5 s). Motor intention is decoded based on the average vectors of synergy activation profiles for the 4 discrete movements. **b**, Motor control performance is shown for two representative subjects in α-space. The AMI subject maintained all 4 discrete movements up to the highest difficulty level with time constraint (0.5 s, $ID_{0.5}$). In contrast, the CTL subject started to lose boundaries at $ID_{0.8}$ and completely lost them at $ID_{0.5}$. Relationships are shown in **c** and **d** between the motor control performance and the degree of AMS in a combined analysis of affected AMI and CTL limbs (n = 14) at all IDs. Further, relationships are shown in **e** and **f** between the economy of motion and the degree of AMS using a similar combined analysis. Motor control performance and the economy of motion were evaluated by the error and straightness of motor control traces to the target motor tasks. Kendall's tau coefficients (τ), P, R^2, and the Jackknife mean and s.d. of AMS_c are reported.

Subject-Specific Proprioceptive Limb Perception

Afferent signals from sensory receptors involved in proprioception[16] have been found to strongly influence both motor control[52] and proprioceptive limb perception[52,53]. Based on the findings presented in earlier sections, it can be inferred that the extent of residual AMS plays a crucial role in maintaining natural motor control following limb amputation, and it may also have a role in retaining proprioceptive phantom limb perception. To explore this hypothesis experimentally, participants were asked to move and vary their phantom foot positions to different percentages of their DF or PF range of motion, and to 50% and 100% of their IN or EV range of motion, while mirroring phantom limb perception with their biologically intact foot.

Figure 5a displays representative data for three subjects, namely AMI-1, CTL-3, and CTL-5, who underwent different types of amputations. AMI-1 exhibited a high limb perception capacity (0.77) and was able to vary the position of her phantom foot to a large extent. In contrast, CTL-3 had a lower limb perception capacity (0.32) and was not able to vary the position of his phantom foot as much. Interestingly, CTL-5, who underwent an Ertl osteomyoplastic amputation[42], had a high limb perception capacity (0.60) and was able to vary the position of his phantom foot to a great extent. Moreover, the ultrasound examination of CTL-5 revealed a 2-DoF 'joystick-like' coupling between antagonistic muscle pairs, which were distributed across the inferior aspect of his residual limb, as shown in the comparison in Figure 5b.

A significant positive association ($\tau = 0.58$, $P < 0.005$) was observed between limb perception capacity and the degree of AMS (Figure 5c) for all 14 residual limbs. However, the AMS_c value necessary for preserving limb perception capacity ($AMS_c = 0.61$, $R^2 = 0.45$) was found to be higher than the values required for preserving natural muscle synergy, synergy activation similarity, and 2-DoF motor controllability (AMS_c ranged from 0.21-to-0.26). The results suggest that the degree of preserved residual muscle AMS after limb amputation impacts subject-specific limb perception capacity. Additionally, our findings imply that a higher degree of preserved AMS is necessary to maintain proprioceptive limb perception compared to the degree required for biomimetic motor control. AMI-2 and CTL-2 (encircled, Figure 5c), who did not follow the trend, reported no functional range of motion prior to their amputations.

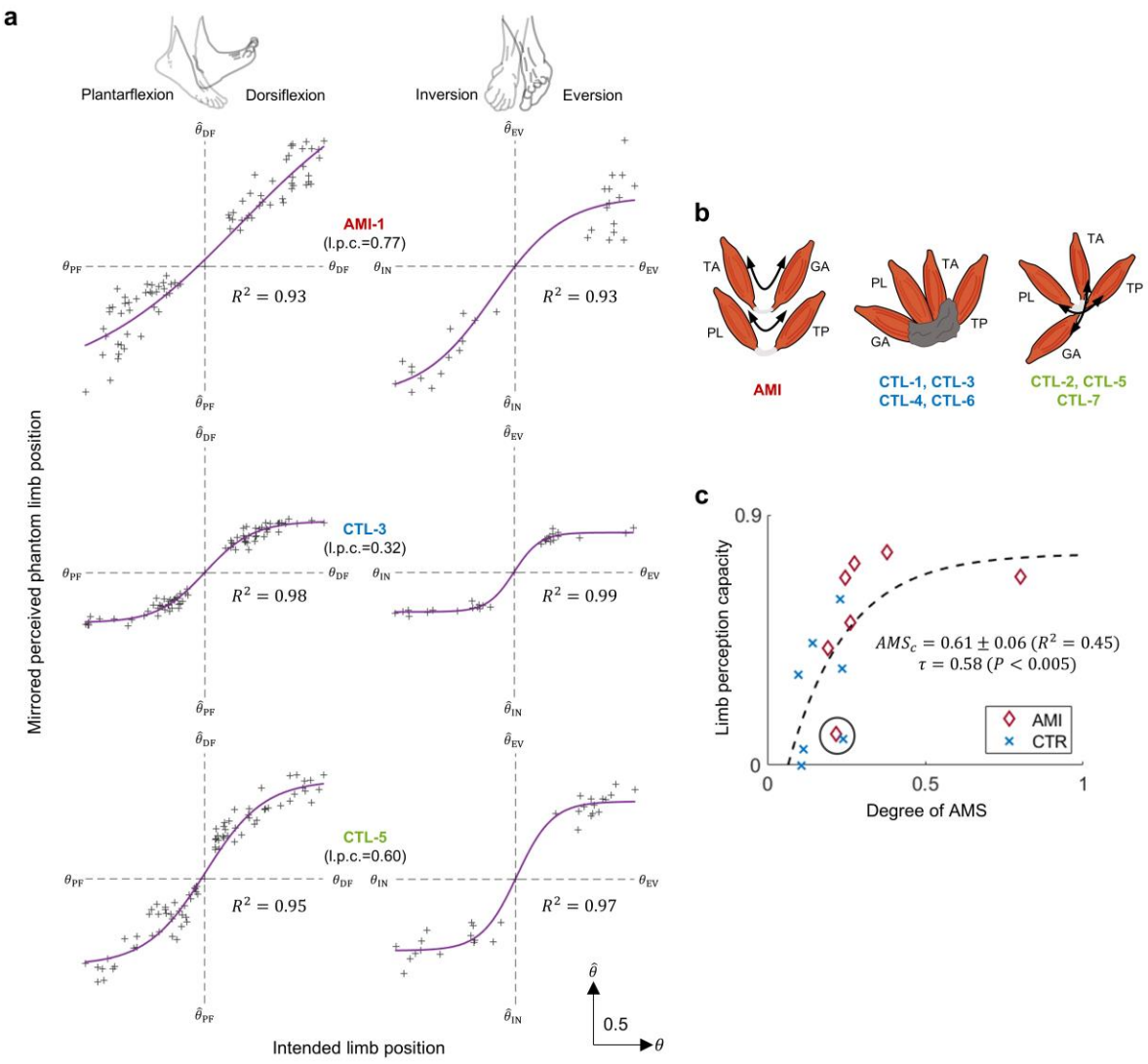

Figure 5 | Subject-specific proprioceptive perception. a, Relationships are shown between the mirrored perceived phantom limb position as measured from the biologically-intact limb without visual feedback and the intended phantom limb positions for three representative subjects (AMI-1, CTL-3, and CTL-5), who had respectively undergone AMI, traditional, and Ertl osteomyoplasty amputation procedures. Estimated limb perception capacity (l.p.c.) is reported. **b**, Schematic diagrams are shown of the anticipated residual limb structures, based on ultrasonography, highlighting the dynamic AMI construct excursion in 2-DoF for AMI, restricted motion in control subjects (CTL-1, CTL-3, CTL-4, and CTL-6), and 'joystick-like' residual muscle coupling in control subjects (CTL-2, CTL-5, and CTL-7). Size and positioning of elements are representative and not to scale. **c**, Limb perception capacity of the phantom limb is plotted against the degree of AMS in a combined analysis of affected AMI and CTL limbs (n = 14). Kendall's tau correlation (τ), P, R^2, and the Jackknife mean and s.d. of AMS_c are reported. The limb perception capacity for AMI-2 and CTL-2 (encircled) deviated from the trend.

Supplemental Clinical Metrics

Clinical metrics were gathered and analyzed to investigate correlations between time since amputation and sensory-motor responses, maximum EMG values, average cross-section of scar tissue, and average phantom limb score (Figure 6 and Table 2). However, no significant correlations, positive or negative, were observed between time since amputation and muscle synergy similarity (AMI: $P = 0.91$, CTL: $P = 0.42$), synergy activation similarity (AMI: $P = 0.15$, CTL: $P = 0.25$), 2-DoF motor controllability (AMI: $P = 0.33$, CTL: $P = 0.46$), or limb perception capacity (AMI: $P = 0.11$, CTL: $P = 0.89$) for the 14 residual limbs. Additionally, no significant differences were found between the AMI and CTL subjects regarding the maximum EMG values recorded from the four target muscles (TA: $t = 1.41$, $P = 0.18$, TP: $t = -0.30$, $P = 0.77$, GA: $t = 1.49$, $P = 0.16$, PL: $t = -0.74$, $P = 0.48$), average scar tissue cross-sectional area ($t = 0.11$, $P = 0.91$), quantified with ultrasonography[54], or average phantom limb pain score ($t = 2.08$, $P = 0.06$).

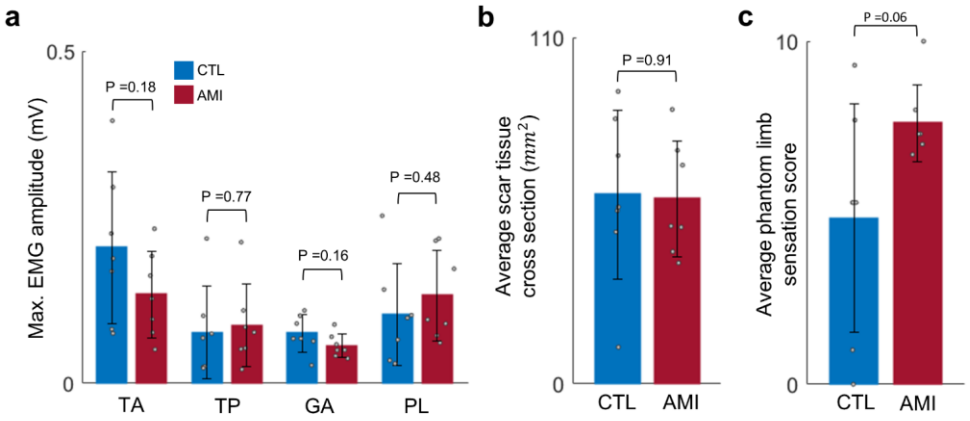

Figure 6 | Statistical analyses on clinical measures. **a**, No significant differences were found in maximum EMG amplitudes of all four muscles investigated in this study between the AMI and CTL groups. **b**, The average scar tissue cross sectional area within residual muscles was accessed through ultrasound imaging. No significant difference was found between the AMI and CTL groups. **c**, The average phantom limb score of AMI and CTL groups showed no significant difference. Unpaired two-tailed *t* tests were performed for the AMI and CTL comparisons. Bars and error bars represent mean and s.d., respectively (CTL: $n = 7$, AMI: $n = 7$).

Table 2 | Reported phantom limb sensation score and phantom limb pain

Subject ID	Ankle joint	Subtalar joint	Ankle/subtalar rotation	Mean score	Biological sex
AMI-1	10	10	10	10	No serious or prohibitive pain
AMI-2	8	7	7	7.3	Tingling
AMI-3	8	8	8	8	No serious or prohibitive pain
AMI-4	8	7	7	7.3	No serious or prohibitive pain
AMI-5	7	6	7	6.7	No serious or prohibitive pain
AMI-6	9	6	6	7	No serious or prohibitive pain
AMI-7	9	5	7	7	No serious or prohibitive pain
CTL-1	0	0	0	0	Frozen phantom limb, ski boot sensation
CTL-2	9	9	10	9.3	'Firework' sensations
CTL-3	5	5	6	5.3	Pins and needle sensation, occasional itching
CTL-4	7	3	6	5.3	Numbness
CTL-5	8	7	8	7.7	No serious or prohibitive pain
CTL-6	2	0	0	1	No serious or prohibitive pain
CTL-7	6	5	5	5.3	No serious or prohibitive pain

Vividness of phantom limb sensation is reported on a scale of 0 to 10, where values of 0 and 10 respectively indicate no sensation or equivalent sensations between the subject's phantom joint and their biologically intact limbs.

Discussion

This study provides evidence that the degree of AMS within residual limb muscles postamputation is a neuromechanical determinant that underlies the large variability observed in subject-specific motor control and perception during specific free space motor tasks. The findings support the hypothesis that preserving transtibial residual-limb AMS can restore sensorimotor capacity postamputation.

The study found that the metric of AMS, a characteristic feature of residual limb structure, allowed for the correlation of six different sensorimotor responses from 14 transtibial amputees. Despite significant variability amongst participants in terms of age, time since amputation, surgical procedures, and etiologies, there was a clear correlation between residual limb AMS and sensorimotor responses. This correlation was demonstrated to be an exponential response, with gradual and monotonic improvements in motor control and perception observed as the degree of preserved AMS increased. These findings highlight the importance of surgical amputation strategies, such as the AMI, that prioritize the preservation of AMS.

The critical level of AMS identified in the exponential response suggests that the central nervous system (CNS) is sensitive to modified AMS in preserving motor control and perception, since muscle synergies and proprioceptive limb perception are organized at the CNS level[38,55]. This CNS sensitivity to modified AMS is important to consider when predicting outcomes of advanced surgical augmentation strategies for motor control and proprioceptive perception. The AMS_c for muscle synergy, synergy activation similarity, and 2-DoF motor controllability range was found to be between 0.21-0.26, which indicates that preservation of about 21-26% AMS will induce 95% preservation of natural motor control for discrete and multi-DoF movements. However, the AMS_c for phantom limb perception capacity was relatively high at 0.61, suggesting

that a higher degree of afferent signaling from AMS may be required for proprioceptive memory modulation[56–58] compared to preserving motor control. This difference in AMS_c for motor control versus proprioceptive percepts was observed in the study participants with AMS preservation values close to the 21-26% range. Although these participants exhibited a natural level of motor control, they showed a limited degree of proprioceptive percepts. This was the case for participants AMI-3, AMI-7, CTL-5, and CTL-7, whose AMS values were 23.2%, 23.8%, 19.2%, and 26.4%, respectively.

This study presents a platform that combines muscle synergy analysis with biophysical and biomedical sciences to clinically demonstrate the impact of AMS on physiological motor control after limb amputation in 14 amputee subjects. Previously, the reasons underlying motor control and proprioceptive perception postamputation were poorly understood. The present approach provides a predictive index of postamputation outcome, AMSc, derived through a combination of mathematical, biomechanical, and clinical data. The findings offer new insights into motor and sensory perturbations by people living with major limb amputation. With further refinement, the concept of a critical degree of AMS may elucidate fundamental factors underlying clinical outcomes after amputation and inform future amputation paradigms and neuroprosthetic system designs.

Preservation of AMS may also improve motor control and proprioceptive percepts for patients who undergo amputations at other anatomical levels. The AMI amputation procedure has been conducted on over 30 patients at the transtibial, transfemoral, transradial and transhumeral levels to enable improved motor control and sensory perception in a broader population of amputee subjects[32]. When musculature distal to the amputation level is intact and viable, it may be harvested on a neurovascular leash during the amputation procedure, and AMS preservation can then be surgically implemented through muscle pair coupling and mechanical fixation of the construct to the surrounding fascia and muscle within the residuum[32]. If musculature distal to the amputation level is not viable, then AMS preservation may be implemented by constructing a native AMI using large vascularized muscle with TMR nerve reinnervation, or alternatively by constructing a regenerative AMI from reinnervated muscle grafts[32,59].

In certain situations, the physical constraints of the residuum may make it impractical to surgically implement all agonist-antagonist muscle couplings to fully replicate intact-limb dynamics, particularly in a transradial amputation. In such cases, the AMI procedure may be applied to only major agonist-antagonist muscle pairs, while other surgical approaches such as rPNI and TMR can be employed for the remaining musculature sites and transected nerves. By combining these techniques, the amputation procedure can be tailored to enhance motor control and sensory perception for the individual patient's functional limb restoration, taking into account their unique needs and circumstances. Another important factor to consider is operative time. AMS preservation during amputation typically requires a longer surgery duration and may not always be appropriate in certain cases[60]. For example, in life-threatening emergencies, AMS may initially be excluded and introduced during a revision surgery, which is often performed to address phantom limb pain or neuroma postamputation[61].

Creating a high degree of AMS in residual limbs to emulate natural biomechanics of muscle interaction requires a complex surgical approach that considers factors such as muscle tension, force capacities, and minimizing impedance. However, achieving consistent AMS outcomes in clinical settings remains a challenge, as evidenced by the large variance in AMS observed in the AMI cohort in this study. Further optimization of AMI amputation techniques is needed to address this issue. The main limitation of the study was the small population size, which included 14 transtibial amputees, including 7 AMI and 7 non-AMI participants. Future, larger studies are anticipated to further elucidate the correlations established in this study and provide further insight into how various factors, such as age, time since amputation, body habitus, and amputation etiology, may impact sensorimotor responses.

The importance of mechanoneural transduction within sensory organs for afferent signaling is well-established. However, the impact of altered afferent signals resulting from macroscale reconfiguration of biomechanically-functional tissue architectures on motor control remains poorly understood. This study aims to shed light on this issue by examining the effects of modified afferent signaling from distinct functional tissue architectures of the transtibial residuum. Our findings reveal the neuromechanical determinant of subject-specific residual motor control and phantom limb perception, and demonstrate the sensitivity of its impact on the CNS. To design more effective biomimetic neural interfaces, it is essential to highlight the value of surgical techniques that preserve the natural neuromusculature and biomechanical function of the residuum tissue structure.

Chapter 3. Restoration of versatile neuroprosthetic gait fully driven by the human nervous system

Throughout history, there has been an ongoing effort to create artificial leg replacements that can match the versatility of biological legs. However, currently available bionic legs are not yet capable of emulating the complex gait dynamics that are controlled by both voluntary and reflexive motor control. This chapter presents a neuroprosthetic leg which is entirely driven by the human nervous system and capable of producing biomimetic gait in individuals with transtibial amputations. The neuroprosthetic interface comprises of flexible sensing electrodes and AMI that augments muscle afferent signaling by 17.5% of biologically intact values. The bionic walking speed has increased by 41.3%, enabling equivalent walking speeds to persons without leg amputations, when compared to leg amputees without neural augmentation. Additionally, there is a significant improvement in biomimetic performance in real-world environments, including slopes and stairs with up to a 12-fold increase. These findings suggest that even a small augmentation of afferent signaling can have a significant impact on improving neuroprosthetic gait.

Rationale and Study Design

For a long time, science fiction has portrayed bionic limbs with the same responsiveness and versatility as biological limbs. However, current technology has not yet achieved this level of sophistication[1]. Current bionic limbs rely on intrinsic robotic architecture to mimic human gait without direct nervous system control[2–12]. This is due to the complexity of legged neuromechanics, which involves the coordinated interplay between afferent and efferent signals directed to and from the volitional supraspinal and reflexive spinal neural circuitry[13–15]. This complexity is compounded by the loss of essential locomotor peripheral afferents[16,17] that occurs during the standard-of-care amputation procedure[18]. Previous clinical investigations have demonstrated that bionic legs engineered to provide afferent feedback using electrical nerve stimulation can improve gait function[19–22]. However, such systems have yet to demonstrate biomimetic gait under full nervous system control[1–12,19–22,34,35].

In this chapter, the first neuroprosthetic leg fully driven by the human nervous system and capable of biomimetic gait across both speed and terrain variations is presented. The study aimed to explore the possibility of achieving biomimetic gait by enhancing native muscle afferents within the amputated residuum through a modified amputation, AMI[28–30]. The adaptability of the human neuromuscular system is remarkable, as individuals with intact legs are able to quickly adjust to locomotory disruptions through peripheral afferents[62,63]. This adaptability implies that increasing the range of residual afferent signaling could help amputees adjust their neural circuitry to achieve a more natural prosthetic gait. Muscle afferent signals are considered one of the most important feedback mechanisms for functional locomotion[16]. Therefore, the hypothesis is that an interface such as the AMI could enhance muscle afferent signaling, leading to sensorimotor adaptation and a highly biomimetic neuroprosthetic gait (Figure 7). The study developed an autonomous system to offer full neural control of a bionic limb and evaluated gait using a variety of ambulatory tests. Additionally, a neuromechanical study assessed individual levels of residual limb muscle afferents, and correlation analyses examined the relationship between bionic controllability and residual limb muscle afferents. Finally, statistical group comparisons were made between the AMI and control (CTL) cohorts to demonstrate the efficacy of the proposed neuroprosthetic framework.

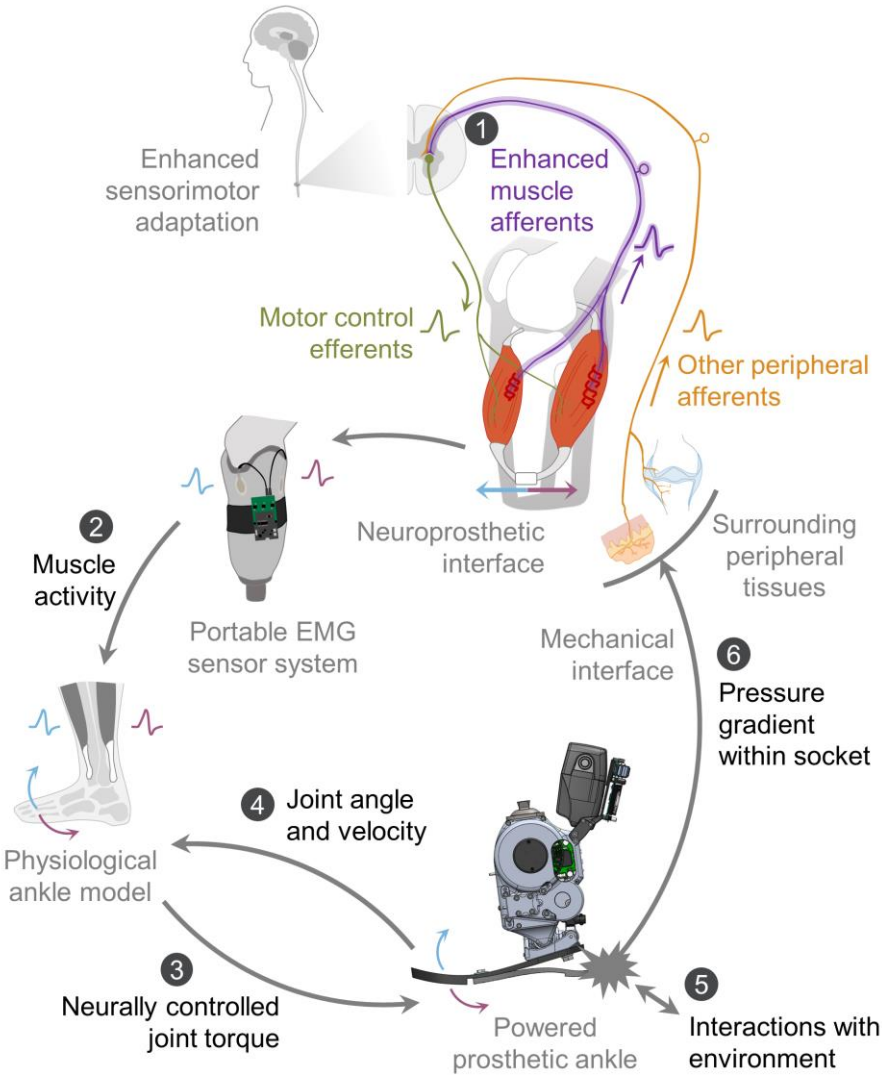

Figure 7 | Schematic diagram of sensorimotor adaptation through neuroprosthetic control of the mechatronic ankle-foot prosthesis. Enhancing muscle proprioceptive afferents resulted in boosting the primary feedback modality for human motor control and adaptation (**i**). Muscle activity is sensed using skin-mounted electromyography (EMG) electrodes (**ii**). These muscle signals, along with prosthetic joint state, are used to control joint torque in a closed loop manner (**iii, iv**). Mechanical information (**v**) was conveyed to the nervous system through pressure gradients within the prosthetic socket during ground contact (**vi**), which mechanically stimulated residual tissues. Such a prosthetic mechanical interface may have acted as an additional afferent signaling apparatus to provide perceptual experiences for sensorimotor adaptation.

Methods

Patient Selection

This study involved 14 participants with unilateral below-knee amputation (age = 47.6 ± 3.5 years, time since amputation = 3.9 ± 0.5 years, height = 1.73 ± 0.02 m, weight = 78.1 ± 3.2 kg) (Table 3). The participants were divided into two cohorts: seven had received an AMI amputation[29] (AMI cohort), while the other seven had received a non-AMI amputation[18,42] (CTL cohort). The cohorts were matched based on age, time since amputation, height, and weight. The sample size was determined based on data from the free-space motor control study presented in the earlier chapter. All participants were experienced with passive prostheses and capable of ambulation at variable cadences (K level 3 and 4[41]). Exclusion criteria included the following underlying health conditions: cardiopulmonary instability manifest as coronary artery disease, chronic obstructive pulmonary disease, and extensive microvascular compromise, as well as persons who are pregnant and/or active smokers. Before participating in the study, all participants provided written informed consent. The study was approved by the Institutional Review Board (COUHES; protocol 1812634918) at the Massachusetts Institute of Technology (MIT).

Table 3 | Study population

Subject ID	Amputation type	Age (years)	Time since amputation (years)	Biological sex	Height (m)	Weight (kg)
CTL 1	Standard	64	5.1	Female	1.65	77.1
CTL 2	Ertl OM	63	4.6	Male	1.78	97.5
CTL 3	Standard	40	4.4	Male	1.60	59.0
CTL 4	Standard	46	8.4	Male	1.78	74.8
CTL 5	Standard	61	5.0	Male	1.73	90.7
CTL 6	Standard	27	3.4	Female	1.64	56.7
CTL 7	Standard	58	2.4	Male	1.70	88.5
AMl 1	AMI	45	4.1	Female	1.65	77.1
AMl 2	AMI	57	5.1	Male	1.73	72.6
AMl 3	AMI	49	2.3	Male	1.70	75.7
AMl 4	AMI	60	3.2	Male	1.91	93.0
AMl 5	AMI	32	0.8	Male	1.85	77.1
AMl 6	AMI	31	2.7	Male	1.68	86.2
AMl 7	AMI	34	3.0	Male	1.75	68.0
CTL		**51.3 ± 5.3**	**4.8 ± 0.7**		**1.70 ± 0.03**	**77.8 ± 5.9**
AMI		**44.0 ± 4.5**	**3.0 ± 0.5**		**1.75 ± 0.04**	**78.5 ± 3.2**
***P*-value**		**0.32**	**0.071**		**0.23**	**0.91**
Total		**47.6 ± 3.5**	**3.9 ± 0.5**		**1.73 ± 0.02**	**78.1 ± 3.2**

mean ± SEM; unpaired *t* test, *n* = 7 per cohort; Ertl OM, Ertl osteomyoplasty

Bionic System and Integration

The bionic limb utilized in the study (Figure 8) was composed of a powered prosthetic ankle, a portable EMG sensor unit, and flexible electrodes that were developed in our group[64,65]. The powered prosthetic ankle was equipped with two brushless electric motors (U8 Lite KV85, T-motor, China) that generated active joint torque up to a maximum of 162 Nm DF-PF torque. The prosthetic ankle had a range of motion of 10 degrees of dorsiflexion (DF) and 20 degrees of plantarflexion (PF) and measured 233 mm in height, weighing 2.42 kg without a battery module. The battery module, which weighed 0.33 kg, had the capacity to power the bionic system for about 2 hours with a single charge. The flexible bipolar surface electrodes (width: 18 mm, length: 60 cm) were fabricated using flexible printed-circuit-board (fPCB) technologies. These electrodes, owing to their flexibility and film thickness (80-100 μm), enabled recording EMG signals during long-duration gait trials without causing any discomfort or pain. The portable EMG sensor system allowed for up to 5 channels for simultaneous EMG recording at 2 kHz with active shielding.

To integrate the system, the following steps were taken: Firstly, a flexible bipolar surface electrode was placed on each target muscle (TA and GAS) using standard double-sided tape, electrode gel (SPECTRA 360 electrode gel, Parker Labs Inc., USA), and hydrocolloid gel patch (Blister bandages, Pnrskter, China). Secondly, the flexible electrodes and their lead wires were guided through liner-liner prosthetic socks to minimize direct contact with the skin surface and prevent potential skin damage due to friction. Thirdly, the subject put on the prosthetic liner while ensuring that the flexible electrodes remained flat and untangled. Fourthly, the subject donned their customary socket and the powered prosthetic ankle was assembled with the socket using the pyramid adapter. Next, the flexible electrodes were plugged into the EMG sensor unit, which was then strapped to the side of the socket. Finally, the EMG board was connected to the powered robotic ankle through universal serial bus (USB).

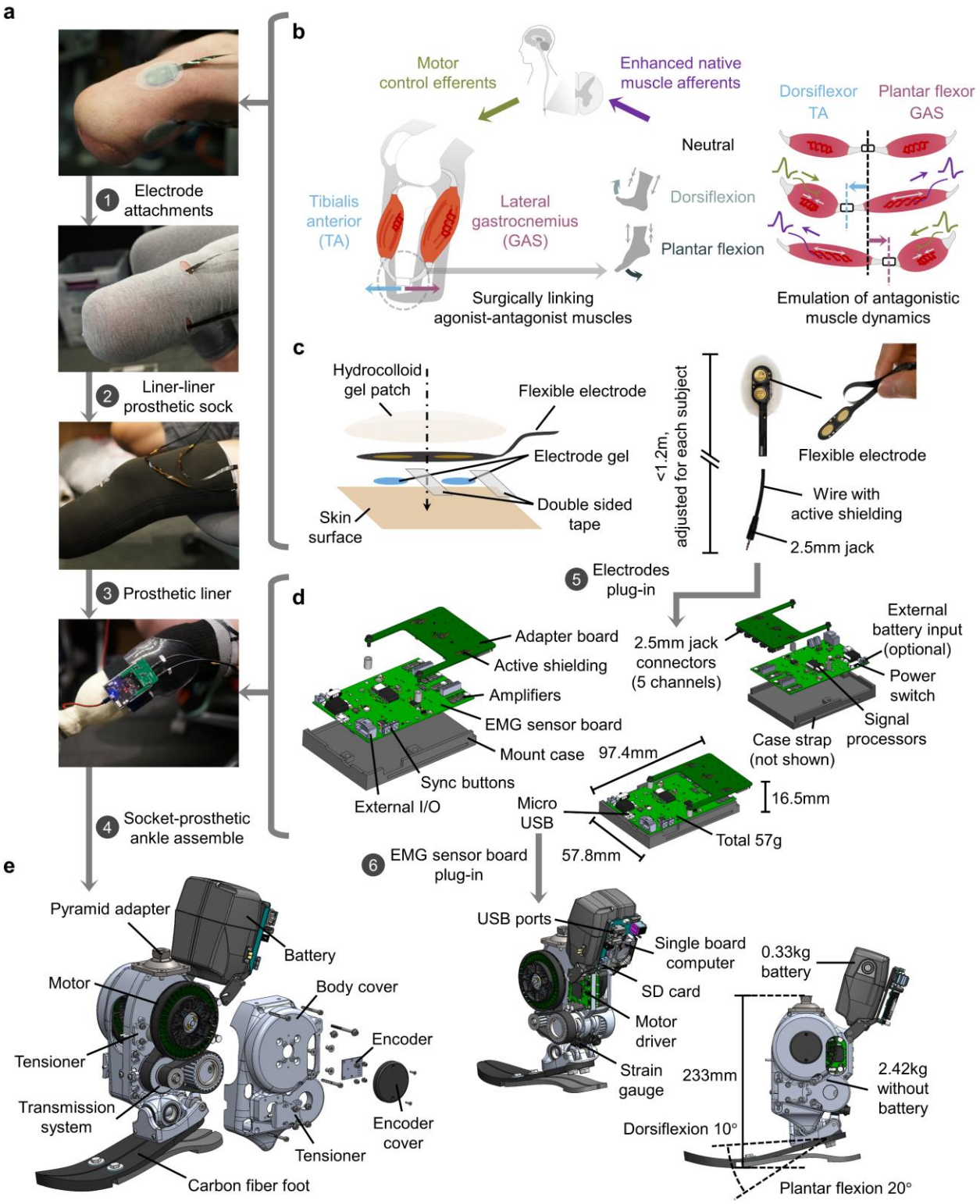

Figure 8 | Autonomous bionic technology. a, Socket-prosthetic ankle assembly. **b**, Agonist-antagonist Myoneural Interface (AMI) for bionic ankle control. **c**, Flexible electrode and attachment methodology. **d**, Portable EMG sensor unit. **e**, Autonomous powered prosthetic ankle.

Bionic Controller

A neuroprosthetic controller was developed (Figure 9) which allows for full neural control of joint angle and impedance[66–68], while also mimicking joint angle- and velocity-dependent biological ankle torque characteristics[69,70]. The controller comprises of three steps: (i) processing of electromyography (EMG) signals, (ii) decoding of motor intention, and (iii) emulation of biological ankle angle- and velocity-dependent torque characteristics.

Raw EMG signals from major dorsiflexor (tibialis anterior, TA) and plantar flexor (gastrocnemius, GAS) were recorded at 2kHz and band-passed with a FIR filter (stop-band: 0-60 Hz, >360 Hz, pass-band: 90-330 Hz, a stop-band attenuation of 85 dB, order: 198) and cumulative histogram filter[71] to facilitate robust reading within the liner-socket system. Then, root-mean-square (RMS) of rectified EMG (200 ms window size) was normalized by using its minimum and maximum values to compute the EMG envelope. Muscle activity was computed (A) from the EMG envelope using bilinear muscle activation dynamics[72] (time constants: t_{act} = 10 ms, t_{deact} = 50 ms).

Motor commands were decoded based on the muscle activities of the TA (A_{TA}) and GAS (A_{GAS}) muscles. Two control variables, namely the target joint angle (θ_{ref}) and the impedance regulation level (μ_Z), were continuously estimated. θ_{ref} was calculated by taking the difference in muscle pair activity ($k_{\mathrm{GAS}}A_{\mathrm{GAS}} - k_{\mathrm{TA}}A_{\mathrm{TA}}$) and applying a second-order low-pass filter with a cut-off frequency of 6 Hz (mass-damper-stiffness model, critical damping). The coefficients k_{GAS} and k_{TA} were determined to ensure that θ_{ref} varied between the maximum DF ($\theta_{\mathrm{max,DF}}$) and PF ($\theta_{\mathrm{max,PF}}$) of the prosthetic ankle. μ_Z was calculated by taking the sum of weighted muscle pair activity ($k_{\mathrm{GAS}}A_{\mathrm{GAS}} + k_{\mathrm{TA}}A_{\mathrm{TA}}$) and normalizing it by its maximum value. The maximum value of $k_{\mathrm{GAS}}A_{\mathrm{GAS}} + k_{\mathrm{TA}}A_{\mathrm{TA}}$ varied between DF and PF due to differences in motor coordination. As a result, $k_{\mathrm{GAS}}A_{\mathrm{GAS}} + k_{\mathrm{TA}}A_{\mathrm{TA}}$ was normalized using different maximum values (N_{DF} and N_{PF}) based on the prosthetic actuation direction, which was determined by the difference (δ) between θ_{ref} and the actual prosthetic ankle angle (θ). DF was indicated by $\delta < 0$ and PF by $\delta \geq 0$. Subject-specific neural-decoding parameters were established based on the EMG profiles during full DF and PF movements of the phantom ankle joint while the subjects were standing on both their biological and bionic limbs.

The target joint torque command (τ_{ref}) was composed of both active (τ_{act}) and passive (τ_{psv}) torques, which were implemented based on an impedance control architecture[66–68], i.e. $\tau_{\mathrm{act}} = K(\theta, \dot{\theta}, A)\delta$, $\tau_{\mathrm{psv}} = K_{\mathrm{psv}}\delta - D_{\mathrm{psv}}\dot{\theta}$. Specifically, $K(\theta, \dot{\theta}, A)$ was determined by the joint angle-torque (K_θ) and velocity-torque (K_v) characteristics of a biological ankle[69,70] and was scaled by μ_Z, resulting in $K(\theta, \dot{\theta}, A) = K_\theta K_v \mu_Z$. The range of $|\delta|$ depended on the joint angle and could vary as $|\delta| \leq |\delta_{\mathrm{DF}}| = |\theta_{\mathrm{max,DF}} - \theta|$ for DF and $|\delta| \leq |\delta_{\mathrm{PF}}| = |\theta_{\mathrm{max,PF}} - \theta|$ for PF. To account for this additional joint angle dependency (note that the angle dependent characteristics of a biological ankle were accounted for by K_θ), δ was scaled as $\delta/|\delta_{\mathrm{DF}}|$ for DF and $\delta/|\delta_{\mathrm{PF}}|$ for PF. In cases where $|\delta_{\mathrm{DF}}|$ and $|\delta_{\mathrm{PF}}|$ were below 1 deg, they were maintained at 1 deg to avoid the denominators becoming zero, which effectively imposed a software hard-stop to gradually

decrease the maximum joint torque to zero as the ankle approached the end of the powered prosthetic ankle range of motion. It is noteworthy that the joint characteristics of the biological ankle differ between DF and PF, and therefore, corresponding joint models were implemented for each movement (DF: $K_{\theta,\mathrm{DF}}$ and $K_{v,\mathrm{DF}}$, PF: $K_{\theta,\mathrm{PF}}$ and $K_{v,\mathrm{PF}}$) using numerical models from previous literature[69,70]. Thus, for DF ($\delta < 0$), τ_{act} was given by $K_{\theta,\mathrm{DF}}K_{v,\mathrm{DF}}\mu_Z\delta/|\delta_{\mathrm{DF}}|$, while for PF ($\delta \geq 0$), τ_{act} was given by $K_{\theta,\mathrm{PF}}K_{v,\mathrm{PF}}\mu_Z\delta/|\delta_{\mathrm{PF}}|$. When $\mu_Z = 1$ and $\delta/|\delta_{\mathrm{DF}}| = -1$ or $\delta/|\delta_{\mathrm{PF}}| = 1$, τ_{act} followed the maximum active joint values of the biological ankle for the given joint states (i.e. $-K_{\theta,\mathrm{DF}}K_{v,\mathrm{DF}}$ for DF and $K_{\theta,\mathrm{PF}}K_{v,\mathrm{PF}}$ for PF), unless the ankle was near the end of the range of motion and being driven towards it. For non-maximum DF or PF motor intention, τ_{act} interpolated the active joint torque values based on the impedance control structure, i.e. the target joint angle and impedance modulation. The passive joint impedance was set as $K_{\mathrm{psv}} =$ 0.45 Nm deg^{-1} and $D_{\mathrm{psv}} = 0.02$ Nm s deg^{-1} to ensure joint stability under zero muscle activity.

The bionic control system utilized a single board computer (SBC; ODROID-XU4, Hardkernel, South Korea) for high-level computations at a frequency of 1kHz. Communication between the SBC and the low-level motor drivers (FlexSEA[73], Dephy, USA), as well as the sensor units, was facilitated through a controller area network (CAN) communication protocol. Joint angle was measured using high-resolution 14-bit magnetic encoders (AS5047P, ams AG, Austria), which were positioned at the prosthetic joint. Torque values were computed by measuring the moment arm of the prosthetic ankle and force measurements obtained from strain gauges (MMF307425, Micro-Measurements, USA). The system implemented low-level torque control through the back calculation of target force values from target torque values using the moment arm. The torque control was achieved by applying proportional control with damping injection based on force feedback obtained from the strain gauges.

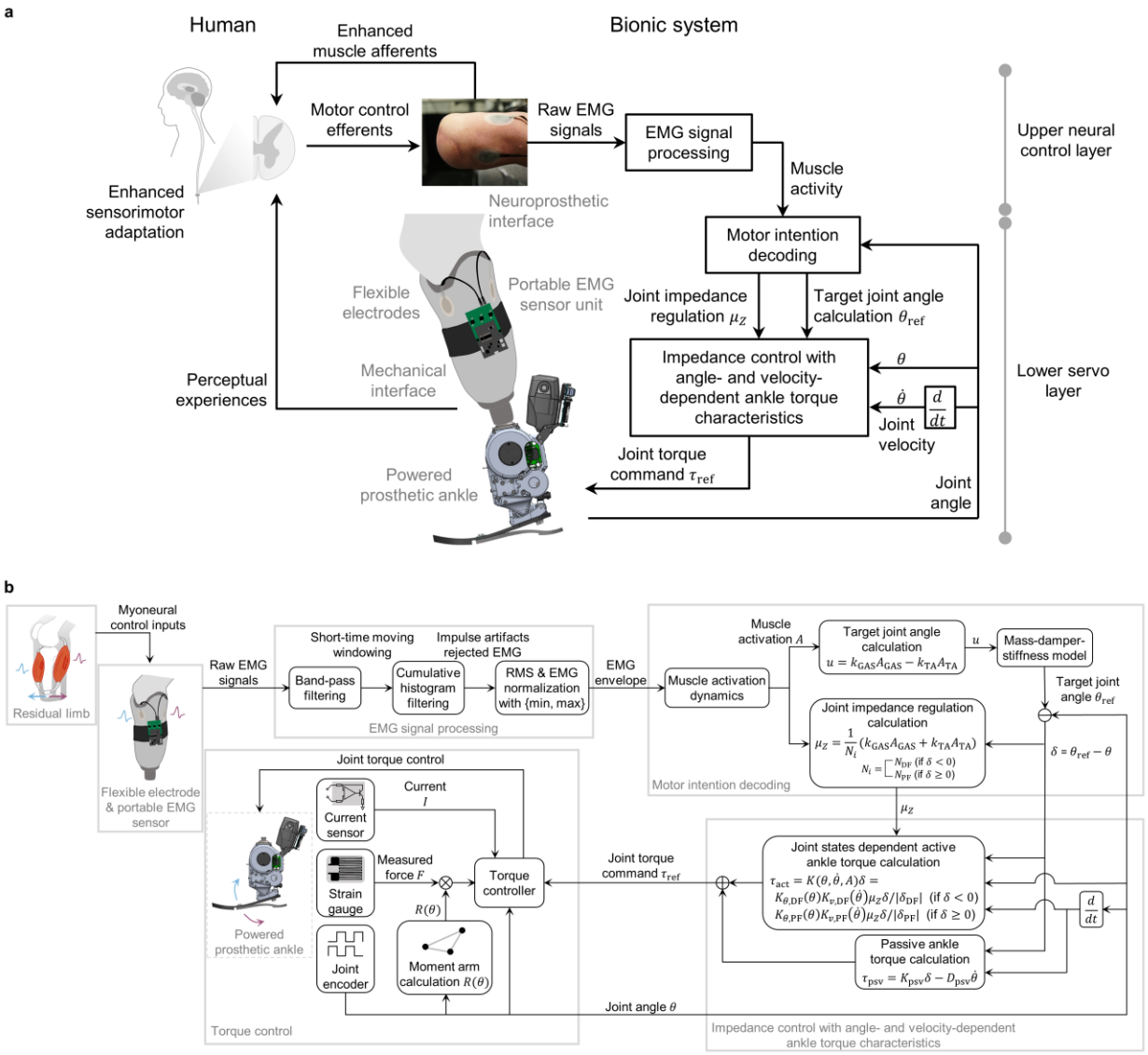

Figure 9 | Bionic control method. a, Autonomous, full neural control implemented with the bionic system. The dorsiflexor and plantar flexor electromyography (EMG) data were processed to compute muscle activities. From the muscle activities, we decoded motor intention into joint impedance regulation (μ_Z) and target joint angle (θ_{ref}). The ankle actuation direction was obtained through the current joint angle (θ) and θ_{ref}, which was used to account for differences in dorsiflexion (DF)-plantar flexion (PF) motor coordination during the μ_Z normalization process. The joint torque command (τ_{ref}) was determined based on an impedance control scheme which modeled joint torque using joint impedance, a neurally-controlled impedance scaling factor μ_Z, and a neurally-controlled equilibrium θ_{ref}. We designed the joint impedance to emulate the biological ankle angle- and velocity-dependent maximum torque for given values of θ and $\dot{\theta}$. The joint torque command scaled the maximum ankle torque using μ_Z and the difference between θ_{ref} and θ. The designed controller utilizes muscle activity and current joint angle and velocity only to replicate biological ankle mechanical behaviors (the lower servo layer). Therefore, this control method fully designated the upper neural control layer to the human nervous system. **b**, The detailed control diagram is shown.

Level-Ground Walking and Terrain Adaptation Experiments

To guarantee the safety of the participants, an initial bionic adaptation was conducted on a 3.6 m walkway equipped with handrails. The participants were instructed to utilize the handrails when necessary to maintain balance, walk at their preferred speed, or pause if needed. In order to explore the sensorimotor integration and controllability of the bionic limb based solely on afferent and efferent neural signaling, the subjects were not given any instructions on how to achieve the desired gait during the experimental sessions. After the participants had demonstrated consistent and stable walking, the following procedure was followed.

Two practice sessions were conducted before commencing data collection, gradually increasing the difficulty of gait from level-ground walking to slope adaptation and stair adaptation to ensure participant safety. The primary objective of these practice sessions was to provide sufficient experience to achieve steady and stable gait using the bionic limb. For level-ground walking, the subjects were guided to walk a 10 m open hallway at a steady pace, and the travel time was recorded to assess walking speed. All subjects were tested for level-ground walking at a slow walking speed (the targeted speed and travel time were respectively 1.0 m s^{-1} and 10 s) and their self-selected maximum speed. Because AMI subjects generally walked faster than CTL subjects at their self-selected maximum speeds, the AMI subjects were also tested at a moderate walking speed (the targeted speed and travel time were respectively 1.25 m s^{-1} and 8 s) to match the CTL subjects' maximum walking speed. If the subject's travel time did not meet the targeted walking speed, they were asked to 'speed up' or 'slow down' as cued by the research team. The acceptance criteria for each targeted speed trial was a 1-second window from the targeted travel time (±0.5 seconds). Four types of terrain adaptation trials were conducted, including 5-degree slope decline/incline and stair descent/ascent. For each terrain adaptation, the subjects were instructed to initiate their gait at a self-selected speed while using handrails whenever necessary for balance. They were asked to gradually reduce handrail usage and speed up until they identified the maximum speed at which they could safely maintain steady gait. Although the practice session lengths varied between subjects, who were allowed to rest upon request, 1 hour was assigned as a gait experience for each level-ground walking, slope, and stair adaptations, resulting in a minimum total of 6 hours of gait experience for all subjects with at least 15 additional minutes of rest between conditions. All subjects reported being confident in performing stable and steady gait before data collection.

During data collection, bionic ankle kinematics, torque, and ipsilateral and contralateral lower-extremity kinematics were recorded simultaneously using onboard sensors and goniometers (Wireless goniometer, Biometrics ltd., UK) at a sampling rate of 1kHz. The collected data were sent by telemetry to a laptop for further analysis. Bionic ankle power and net work were computed based on the recorded bionic joint kinematic and torque data. To evaluate the biomimetic stair adaptive features[74] of the bionic limb, negative peak power values were used for stair descent analysis, and positive peak power values were used for analyses of all other gait conditions. Net work during weight acceptance and step-up phases were used for stair descent and ascent analysis, respectively. Lower-extremity kinematic[75] (LEK) symmetry was evaluated through a mean value of symmetry index (SI) across ankle, knee, and hip joints integrated over a

full gait cycle. Because the SI is an index for kinematic asymmetry[75], kinematic symmetry was computed by 100 – SI (%). Fifteen gait cycles were collected for each level-ground walking condition, and ten gait cycles were collected for each of the four terrain adaption trial types. The gait data were normalized by gait cycle, and prosthetic ankle torque, power, and net work were further normalized by subject weight to allow for intra- and inter-subject analyses. The range of motion (ROM) of ipsilateral and contralateral lower-extremity joints were computed as the difference between the maximum DF and PF or maximum flexion and extension for each gait testing condition.

Kinematic Analysis based on Gait Events

Bionic ankle behaviors were assessed in relation to gait events. Level-ground walking and slope adaptation gait events were subdivided into four phases[76,77], namely loading response, mid-stance, push-off, and foot clearance. Loading response was computed by determining the joint angle change from initial ground contact to the first local maximum plantar flexion during stance. Mid-stance was calculated by examining the joint angle change from the first local maximum plantar flexion to the maximum dorsiflexion during stance. Push-off was evaluated by assessing the joint angle changes from the maximum dorsiflexion during stance to the joint angle at the end of stance. Foot clearance was evaluated by analyzing the joint angle change from the joint angle at the end of stance to the joint angle at the end of swing. Stair descent gait events were subdivided into weight acceptance and forward continuance/leg pull-through[74,78]. Specifically, weight acceptance was computed by analyzing the joint angle changes from initial ground contact to the maximum dorsiflexion during stance. Forward continuance/leg pull-through of stair descent was evaluated by examining the joint angle changes from the maximum dorsiflexion during stance to the joint angle at the end of swing. For stair ascent, gait events were subdivided into weight acceptance, step-up, and foot clearance[74,78]. The weight acceptance phase was computed by assessing the joint angle changes from initial ground contact to the maximum dorsiflexion during stance. Step-up and foot clearance during stair ascent were evaluated in the same way as push-off and foot clearance during level-ground walking and slope adaptation.

Estimation of Residual Limb Muscle Afferents

In order to evaluate the residual limb muscle afferents, the neuromechanics of subjects' TA and GAS muscles were investigated during ten cycles of each maximum phantom DF and PF. The EMG and corresponding TA and GAS muscle fascicle strain data were recorded simultaneously using a custom EMG sensor system[64] and a commercially available ultrasound sensor (LS128, Telemed, Lithuania), respectively. The flexible electrode form factor allowed for the simultaneous recording of EMG and muscle fascicle strain data, even when limited skin surface was available[79]. The muscle fascicle strain was computed from the ultrasound video recordings using UltraTrack software[43,44]. Raw EMG was processed identically to that of the bionic system to compute the EMG envelope. The muscle fascicle strains and EMG envelopes were normalized by the movement cycle to allow for intra- and inter-subject analyses. Averaged muscle fascicle strain and EMG envelope profiles for ten phantom DF and PF cycles were used for the muscle afferent estimation. A computational model (type II muscle spindle model[80,81]) was used to estimate the muscle afferents. The average muscle afferent values during the steady states of

maximum phantom DF and PF (between 25% and 75% of the cycle) were used to evaluate TA and GAS afferents. The bandwidth of residual limb muscle afferent signaling (agonist-antagonist muscle afferents) was computed as the difference between the antagonistic (lengthening) afferents and the agonistic (shortening) afferents of the muscle pair.

Torque-Angle Portrait Analysis

In order to examine the relationship between agonist-antagonist muscle afferents and biomimetic gait, the averaged torque-angle trajectories[2,35] were computed for each cohort (CTL and AMI) and each steady gait testing condition. The maximum walking speed of each cohort was used to evaluate maximum walking capability for the level-ground walking analysis. The torque-angle trajectories were analyzed to assess the performed gait cycle and mechanical energetics.

Correlation Analysis between Bionic Control Metrics and Muscle Afferents

To investigate the relationship between subject-specific bionic gait controllability and residual limb muscle afferents, peak power, net work, and LEK symmetry were plotted against agonist-antagonist muscle afferents in a combined analysis of all subjects for each steady gait testing condition. For the level-ground walking analysis, the values of subjects' maximum walking speeds were used to evaluate the relationships between their maximum walking capability and varying levels of agonist-antagonist muscle afferents.

Statistics

The results for bionic gait and residual limb muscle neuromechanics were reported as mean ± standard error of the mean (SEM). Normality of the data was verified using the Shapiro-Wilk test at a significance level of $\alpha = 0.05$. The effects of the three AMI walking speeds on peak power and net work were analyzed using repeated measures ANOVA. Sphericity was tested using Mauchly's sphericity test. Differences between peak power and net work for the three different level-ground walking speeds tested in the AMI cohort were evaluated by two-sided paired *t* tests with Holm-Šidák correction for multiple comparisons. Within-group comparisons were performed using two-sided paired *t* tests while between-group comparisons were performed using two-sided unpaired *t* tests for normally distributed data. For non-normally distributed data, Mann–Whitney U tests were used for between-group comparisons. Pearson correlations (r) and P-values were reported for the correlation analyses between bionic control metrics and agonist-antagonist muscle afferents. A summary of the full statistical analyses is reported in the Supplementary Information. The statistical analyses were performed using MATLAB 2020b (Mathworks, USA).

Results and Discussion

Neuroprosthetic Level-Ground Walking

In this study, level-ground neuroprosthetic walking was initially tested (Figure 10a) at a slow speed for all fourteen subjects (0.98 ± 0.005 m s^{-1}). Additionally, each subject was asked to demonstrate steady and stable walking at their self-selected maximum speed. It should be noted that the AMI subjects generally walked faster than the CTL subjects at their self-selected

maximum speeds (1.78 ± 0.04 m s^{-1} and 1.26 ± 0.07 m s^{-1}, respectively), and therefore, the AMI subjects performed an additional moderate speed walking test to match the maximum speed of the CTL subjects (maximum CTL and moderate AMI population speed: 1.25 ± 0.04 m s^{-1}).

A higher degree of biomimetic gait was observed in the AMI group compared to the CTL group during multi-speed, level-ground walking trials (Figure 10, 11). This finding supports the hypothesis and suggests that enhancing residual limb muscle afferents is effective. The spinal reflex based on muscle-tendon afferents in biologically-intact limbs is known to increase ankle peak power and net work as walking speed increases[82,83]. The results showed similar increases in bionic ankle peak power and net work in AMI subjects as they increased their walking speed (n = 7, paired t tests with Holm-Šidák correction, $P < 0.05$ and 0.001) (Figure 10b). This degree of biomimetic gait is clinically significant as it enables AMI subjects to achieve a level-ground walking speed (1.78 ± 0.04 m s^{-1}) comparable to that of research subjects with biologically-intact legs (1.81 ± 0.03 m s^{-1} [84]) (n = 10 intact and n = 7 AMI, Mann–Whitney U test, P = 0.52), who have body weights similar to our AMI cohort (69.1 ± 6.0 kg [84]) (n = 10 intact and n = 7 AMI, unpaired t test, P = 0.24). Another promising AMI cohort finding was lower-extremity kinematic[75,85] (LEK) symmetry at their maximum walking speed (84.9 ± 1.3%), which corresponded to 92.9% of the LEK symmetry reported for biologically-intact subjects (91.4% [75]).

In contrast, significant changes were not observed in CTL subject peak power or net work with increasing walking speed (n = 7, paired t tests, P = 0.073 and 0.11). At maximum walking speed, peak power and net work values in AMI subjects (1.95 ± 0.11 W kg^{-1} and 0.174 ± 0.015 J kg^{-1}) were respectively 187% and 455% higher than those in CTL subjects (0.68 ± 0.17 W kg^{-1} and -0.049 ± 0.054 J kg^{-1}; n = 7 per cohort, unpaired t tests, $P < 0.001$ and 0.0018) (Figure 10c and 10d). Additionally, AMI subjects exhibited a maximum walking speed that was 41.3% faster than that of CTL subjects (1.26 ± 0.07 m s^{-1}; n = 7 per cohort, unpaired t test, $P < 0.001$) (Figure 10e). Regarding LEK symmetry, AMI subjects outperformed CTL subjects (67.3 ± 3.4%) (n = 7 per cohort, unpaired t test, $P < 0.001$), representing a 26.2% improvement (Figure 10f, 11).

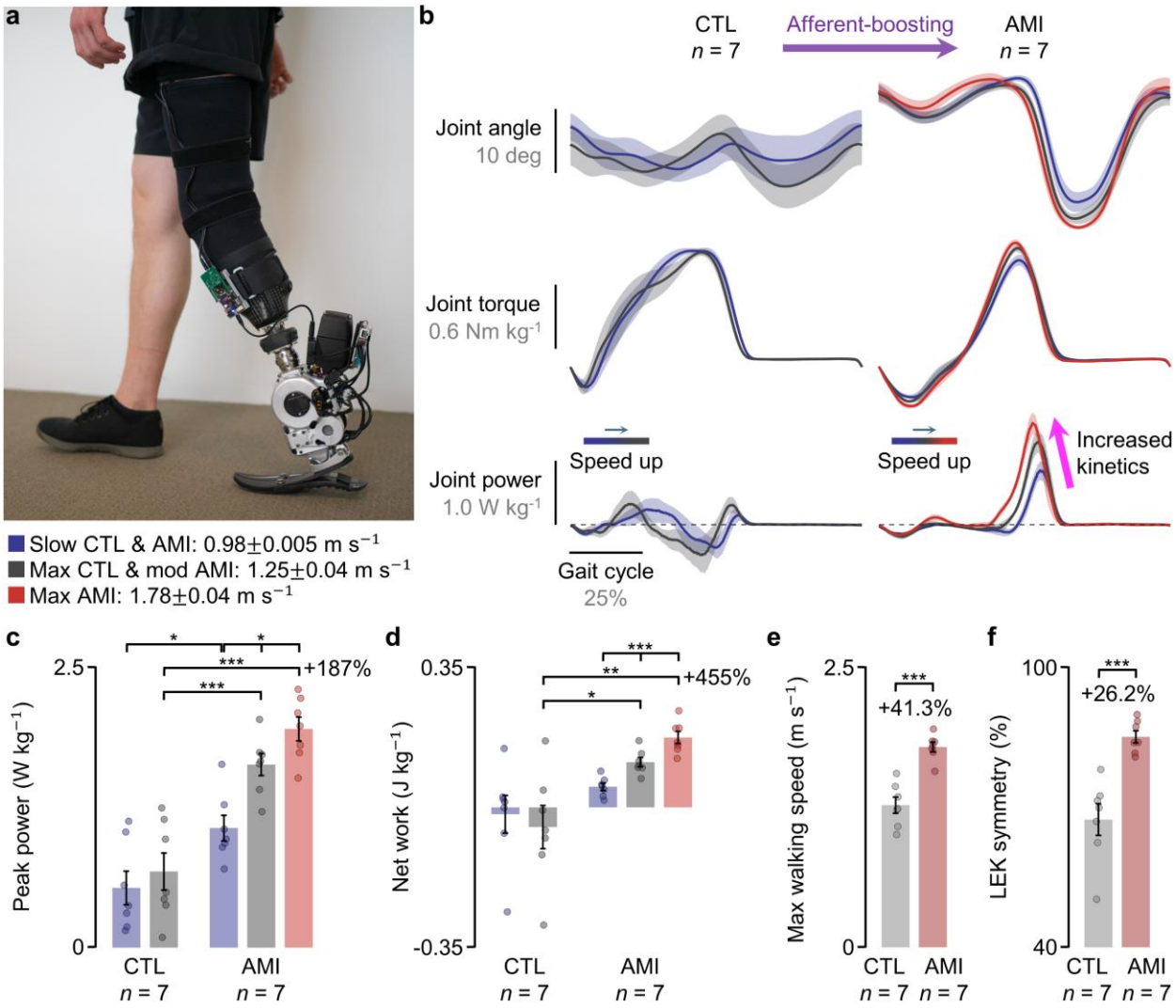

Figure 10 | Neuroprosthetic level-ground walking. a, A participant walking in an open hallway wearing the autonomous neuroprosthesis. Study population walking speeds for each targeted speed are reported (mean ± SEM). Max, maximum; mod, moderate. **b**, Mechanics of level-ground neuroprosthetic walking are shown at three walking speeds (bolded lines, mean; shaded regions, SEM). **c**, **d**, Peak power (**c**) and net work (**d**) of the bionic ankle are shown (bars, mean; error bars, SEM). **e, f**, Max walking speed (**e**) and lower-extremity kinematic (LEK) symmetry between ipsilateral and contralateral limbs at the max speed (**f**) are shown (bars, mean; error bars, SEM). For these analyses, paired and unpaired *t* tests were used for within and between group comparisons, respectively, with Holm-Šidák correction for multiple comparisons ($n = 7$ per cohort, $^*P < 0.05$, $^{**}P < 0.01$, $^{***}P < 0.001$). Lower-extremity kinematics are reported in Figure 11. Full statistics are reported in Table 4.

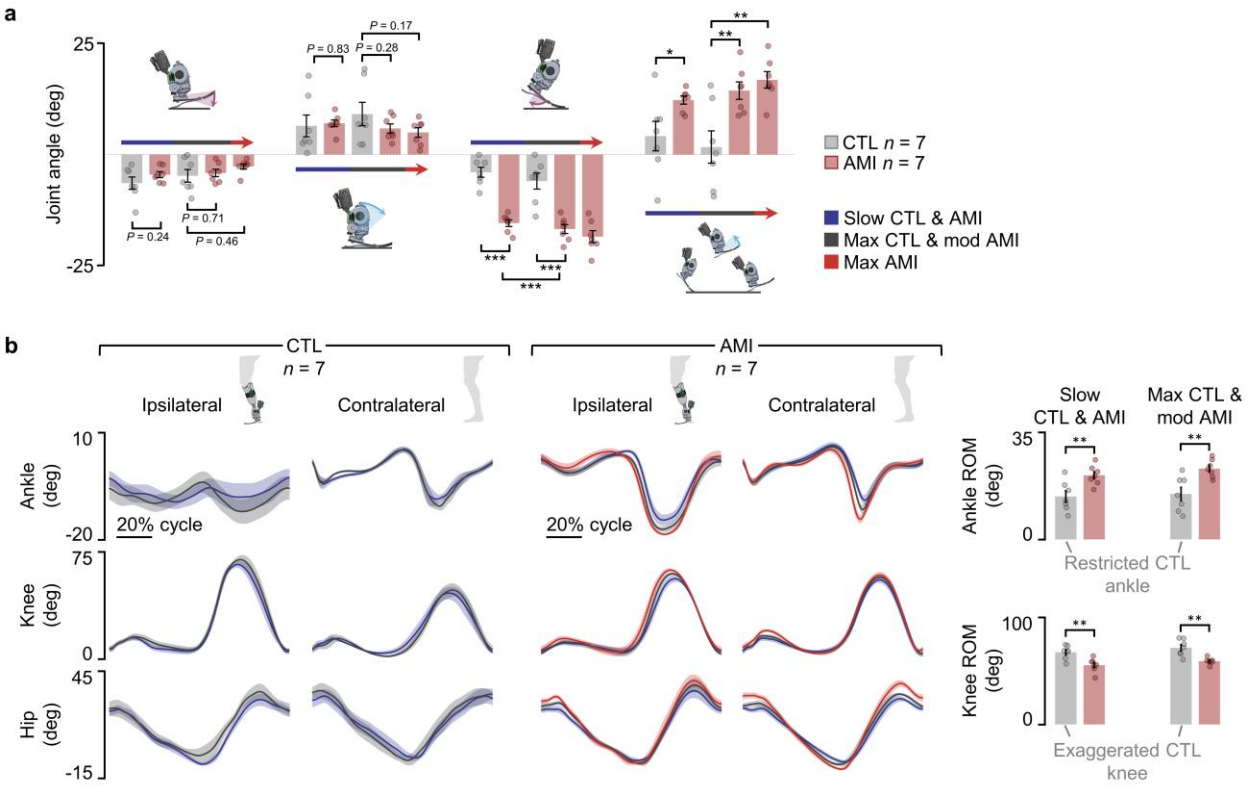

Figure 11 | Lower-extremity kinematics during level-ground walking. a, Kinematics during level-ground walking for each gait event (bars, mean; error bars, SEM). Max, maximum; mod, moderate. Gait events assessed are loading response, mid-stance, push-off, and foot clearance. For these analyses, Mann–Whitney U test was used for the loading response comparison of each cohort's maximum walking, unpaired *t* tests for other comparisons ($n = 7$ per cohort, $^{*}P < 0.05$, $^{**}P < 0.01$, $^{***}P < 0.001$). Compared to the CTL bionic kinematics, the AMI cohort modulates significantly larger plantar flexion and dorsiflexion during the gait events that are critical for large propulsion (push-off) and swing control. **b**, Ankle, knee, and hip kinematics of ipsilateral and contralateral lower-extremities during level-ground walking (bolded lines, mean; shaded regions, SEM). The ipsilateral (prosthetic) ankle and knee ROM comparisons are shown for the CTL and AMI cohorts (bars, mean; error bars, SEM). ROM, range of motion. For these analyses, unpaired *t* tests was used ($n = 7$ per cohort, $^{*}P < 0.05$, $^{**}P < 0.01$, $^{***}P < 0.001$). Full statistics are reported in Table 4 and 5.

Neuroprosthesis Responsive to Terrain

Individuals with biologically-intact limbs are capable of executing versatile gait on various terrains[13,33,74,76]. To assess the neuroprosthetic adaptability, all fourteen participants were instructed to navigate different terrains, including a 5-degree slope and stairs (Figure 12a). The results provided further evidence in support of the hypothesis. The bionic ankle mechanics exhibited slope and stair adaptive features that resembled biological mechanisms[13,74,76] in the AMI cohort (Figure 12, 13). During slope adaptation, the mechanics of level-ground walking were maintained by AMI subjects, while peak power and net work were increased for the incline compared to the decline (n = 7, paired t tests, P = 0.0037 and 0.0045) (Figure 12b). The shock absorption during initial weight acceptance during stair descent and propulsive torque during the step-up phase of stair ascent was modulated by the AMI subjects (Figure 12c). The ability to perform such versatile and biomimetic adaptations was previously unattainable with neuroprostheses even with non-neural, intrinsic control assistance[8,9,34,35]. In contrast, CTL subjects failed to perform biomimetic adaptations on either slope (n = 7, paired t tests, P = 0.37 and 0.34) or stairs. Additionally, CTL subjects showed restricted bionic ankle range of motion on both slope (n = 7 per cohort, Mann-Whitney U test, incline: $P < 0.001$) and stair adaptations (n = 7 per cohort, unpaired t tests, descent: P = 0.034, ascent: $P < 0.001$), further demonstrating limited locomotory adaptation capability (Figure 13). Furthermore, during terrain adaptations, AMI subjects demonstrated significantly higher bionic peak power, ranging from 163% to 202%, and net work, ranging from 181% to 1221%, than CTL subjects (n = 7 per cohort, unpaired t tests, $P < 0.0052$) (Figure 12d, 12e). AMI subjects also outperformed CTL subjects in LEK symmetry (n = 7 per cohort, incline: Mann–Whitney U test, others: unpaired t tests, $P < 0.027$), with improvements ranging from 13.1% to 27.9% (Figure 12f, 13). These results suggest that the enhanced muscle afferents offered by the neuroprosthetic interfaces can help achieve more versatile and biomimetic terrain adaptations.

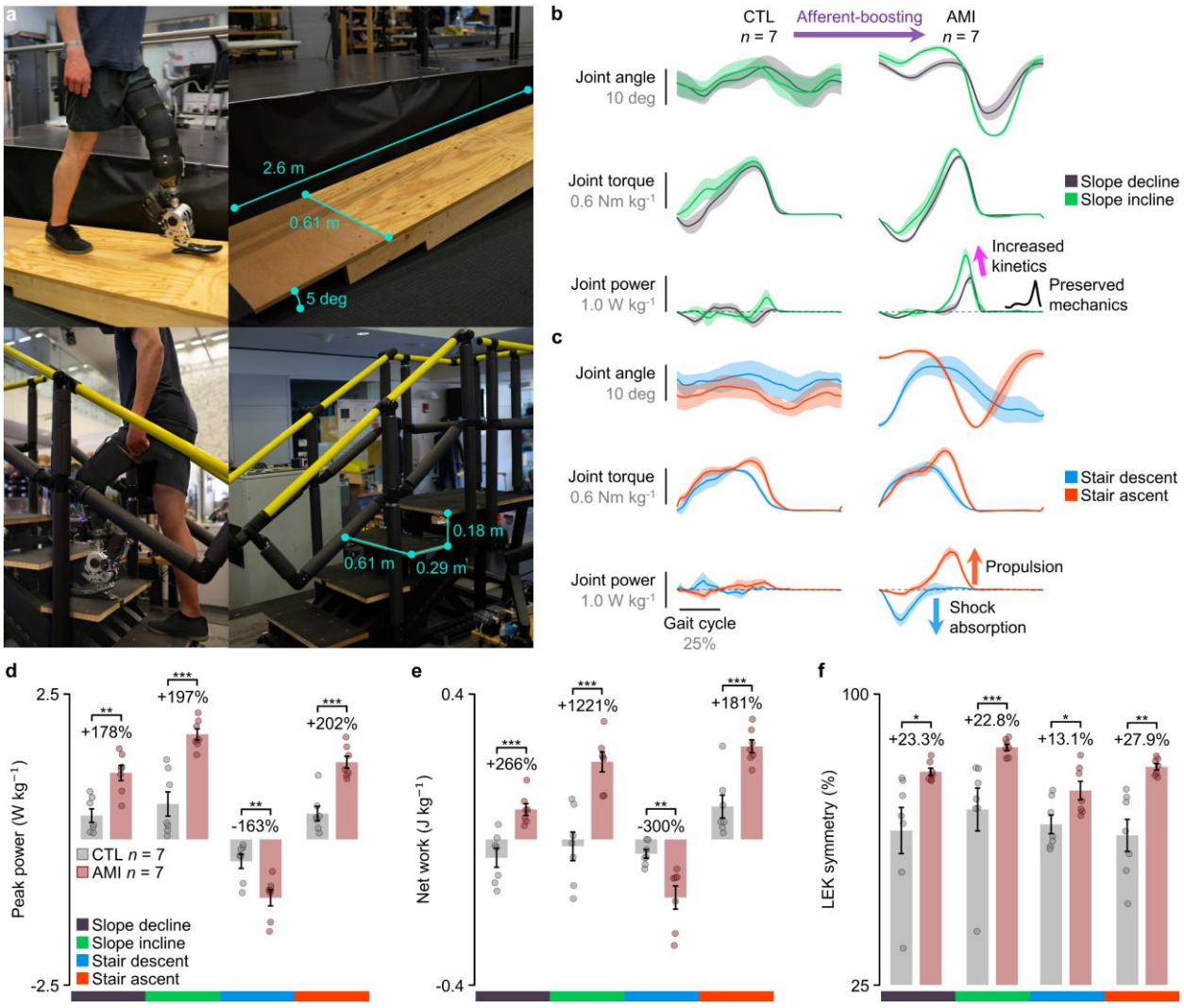

Figure 12 | Neuroprosthesis responsive to terrain. a, A participant ambulating on a 5 degree slope and stair case. **b**, **c**, Mechanics of bionic slope adaptation (**b**) and stair adaptation (**c**) (bolded lines, mean; shaded regions, SEM). **d-f**, Biomechanical adaptations to slopes and stairs by AMI and CTL subjects are shown for peak power (**d**), net work (**e**), and lower-extremity kinematic (LEK) symmetry (**f**) (bars, mean; error bars, SEM). Negative peak power values are reported for stair descent, whereas positive peak power values are reported for all other conditions. Net work during weight acceptance and step-up are respectively reported for stair descent and ascent. For these analyses, Mann–Whitney U test was used for the LEK symmetry comparison of slope incline, and unpaired *t* tests were used for other comparisons ($n = 7$ per cohort, $^{*}P < 0.05$, $^{**}P < 0.01$, $^{***}P < 0.001$). Lower-extremity kinematics are reported in Figure 13. Full statistics are reported in Table 4.

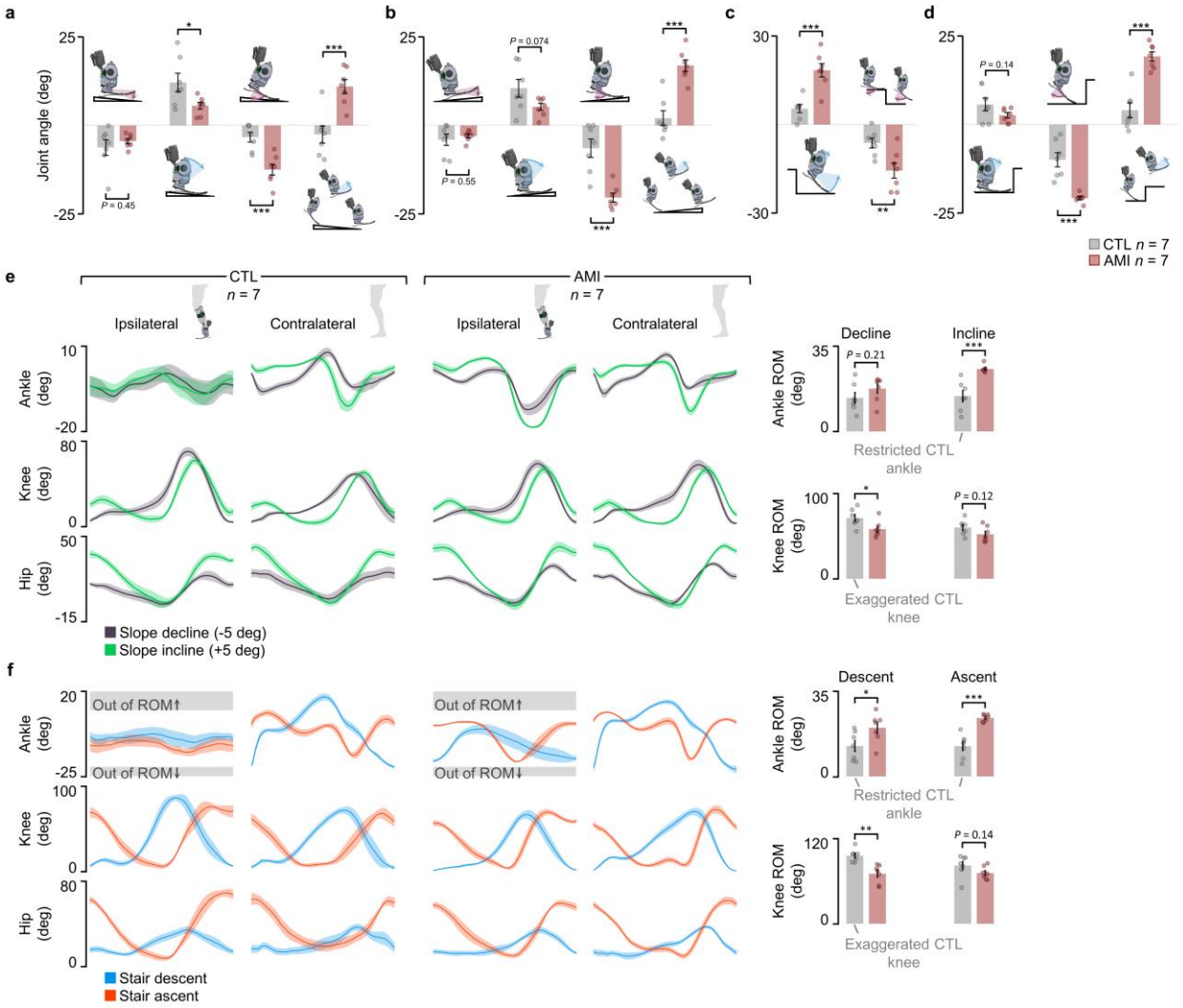

Figure 13 | Lower-extremity kinematics during terrain adaptation. a-d, Kinematics during slope decline (**a**), slope incline (**b**), stair descent (**c**) and ascent (**d**) for each gait event (bars, mean; error bars, SEM). Gait events assessed for slope adaptation are loading response, mid-stance, push-off, and foot clearance. Gait events assessed for stair adaptation are weight acceptance and forward continuance/leg pull-through for stair descent and weight acceptance, step-up, and foot clearance for stair ascent. Compared to the CTL bionic kinematics, the AMI cohort modulates significantly larger plantar flexion and dorsiflexion during the gait events that are critical for large propulsion (push-off and step-up) and shock absorption (weight acceptance of stair descent), and swing control. For these analyses, unpaired *t* tests were used for other comparisons ($n = 7$ per cohort, $^{*}P < 0.05$, $^{**}P < 0.01$, $^{***}P < 0.001$). **e**, **f**, Ankle, knee, and hip kinematics of ipsilateral and contralateral lower-extremities during slope adaptation (**e**) and stair adaptation (**f**) (bolded lines, mean; shaded regions, SEM). ROM, range of motion. The ipsilateral (prosthetic) ankle and knee ROM comparisons are shown for the CTL and AMI cohorts (bars, mean; error bars, SEM). For these analyses, Mann–Whitney U test was used for the ankle ROM comparisons of slope adaptation, unpaired *t* tests for other comparisons ($n = 7$ per cohort, $^{*}P < 0.05$, $^{**}P < 0.01$, $^{***}P < 0.001$). Full statistics are reported in Table 4 and 5.

Table 4 | Bionic control metrics

		CTL (Mean ± SEM)	AMI (Mean ± SEM)	*P*-value
Level-ground walking				
Slow	Peak power (W kg^{-1})	0.53 ± 0.15	1.06 ± 0.11	0.016
	Net work (J kg^{-1})	-0.017 ± 0.047	0.051±0.009	0.18
	LEK symmetry (%)	70.6 ± 2.2	84.0 ± 1.3	<0.001
	Speed (m s^{-1})	0.97 ± 0.01	0.98 ± 0.01	0.70[#]
	Loading response (deg)	-6.46 ± 1.40	-4.53 ± 0.67	0.24
	Mid-stance (deg)	6.48 ± 2.46	7.05 ± 0.77	0.83
	Push-off (deg)	-4.02 ± 1.13	-15.50 ± 0.76	<0.001
	Foot clearance (deg)	4.18 ± 3.34	12.33 ± 0.92	0.037
Max (CTL)/mod (AMI)	Peak power (W kg^{-1})	0.68 ± 0.17	1.63 ± 0.10	<0.001
	Net work (J kg^{-1})	-0.049 ± 0.054	0.113 ± 0.011	0.012
	LEK symmetry (%)	67.3 ± 3.4	84.1 ± 1.5	<0.001
	Speed (m s^{-1})	1.26 ± 0.07	1.24 ± 0.01	0.78
	Loading response (deg)	-4.80 ± 1.44	-4.16 ± 0.82	0.71
	Mid-stance (deg)	9.15 ± 2.65	5.91 ± 1.03	0.28
	Push-off (deg)	-6.01 ± 1.81	-16.84 ± 1.01	<0.001
	Foot clearance (deg)	1.69 ± 3.65	14.45 ± 1.97	0.0096
Max (AMI)	Peak power (W kg^{-1})	n.a.	1.95 ± 0.11	<0.001
	Net work (J kg^{-1})	n.a.	0.174 ± 0.015	0.0018
	LEK symmetry (%)	n.a.	84.9 ± 1.3	<0.001
	Speed (m s^{-1})	n.a.	1.78 ± 0.04	<0.001
	Loading response (deg)	n.a.	-2.70 ± 0.59	0.46[#]
	Mid-stance (deg)	n.a.	5.00 ± 1.09	0.17
	Push-off (deg)	n.a.	-18.56 ± 1.33	<0.001
	Foot clearance (deg)	n.a.	16.88 ± 1.85	0.0030
Slope adaptations				
Decline	Peak power (W kg^{-1})	0.41 ± 0.11	1.14 ± 0.13	0.0012
	Net work (J kg^{-1})	-0.050 ± 0.026	0.083 ± 0.016	<0.001
	LEK symmetry (%)	64.8 ± 5.9	79.9 ± 0.9	0.027
	Loading response (deg)	-6.25 ± 2.22	-4.44 ± 0.71	0.45
	Mid-stance (deg)	12.15 ± 2.62	5.57 ± 0.97	0.037
	Push-off (deg)	-3.32 ± 1.38	-12.54 ± 1.56	<0.001
	Foot clearance (deg)	-2.56 ± 2.41	11.00 ± 1.97	<0.001
Incline	Peak power (W kg^{-1})	0.61 ± 0.21	1.81 ± 0.10	<0.001
	Net work (J kg^{-1})	-0.019 ± 0.039	0.213 ± 0.027	<0.001
	LEK symmetry (%)	70.2 ± 5.5	86.2 ± 0.8	<0.001[#]
	Loading response (deg)	-4.05 ± 1.61	-2.99 ± 0.56	0.55
	Mid-stance (deg)	10.51 ± 2.51	5.25 ± 0.98	0.074
	Push-off (deg)	-6.45 ± 2.59	-20.44 ± 1.24	<0.001
	Foot clearance (deg)	2.06 ± 2.09	16.95 ± 1.64	<0.001
Stair adaptations				
Descent	Peak power (W kg^{-1})	-0.38 ± 0.12	-1.00 ± 0.14	0.0052
	Net work (J kg^{-1})	-0.040 ± 0.012	-0.160 ± 0.032	0.0041
	LEK symmetry (%)	66.4 ± 2.4	75.1 ± 2.4	0.024
	Weight acceptance (deg)	5.39 ± 1.39	18.43 ± 2.30	<0.001
	FC & leg pull-through (deg)	-6.27 ± 1.65	-15.65 ± 2.58	0.0098
Ascent	Peak power (W kg^{-1})	0.44 ± 0.12	1.33 ± 0.10	<0.001
	Net work (J kg^{-1})	0.091 ± 0.032	0.256 ± 0.018	<0.001
	LEK symmetry (%)	63.5 ± 4.2	81.2 ± 0.8	0.0013
	Weight acceptance (deg)	5.69 ± 1.83	2.61 ± 0.75	0.14
	Step-up (deg)	-9.97 ± 1.99	-20.84 ± 0.47	<0.001
	Foot clearance (deg)	4.05 ± 2.10	19.27 ±1.33	<0.001

Relevant characteristics of bionic control metrics. The metrics of the maximum (max) AMI walking were compared to those of the max CTL walking. For data that violated normality, Mann–Whitney U tests (#) were used, unpaired *t* tests for other comparisons (n = 7 per cohort for each condition). Mod, moderate; n.a., not applicable; FC, forward continuance.

Table 5 | Lower-extremity range of motion during bionic gait

			CTL (Mean ± SEM)	AMI (Mean ± SEM)	*P*-value
Level-ground walking					
Slow	Ankle	Ipsilateral (deg)	14.06 ± 1.84	20.99 ± 1.21	0.0084
		Contralateral (deg)	19.64 ± 1.42	17.36 ± 1.48	0.29
	Knee	Ipsilateral (deg)	67.46 ± 2.40	55.45 ± 2.43	0.0042
		Contralateral (deg)	52.17 ± 2.18	55.05 ± 2.12	0.36
	Hip	Ipsilateral (deg)	39.40 ± 4.61	41.19 ± 4.70	0.79
		Contralateral (deg)	41.08 ± 2.46	37.38 ± 1.77	0.25
Max (CTL)/mod (AMI)	Ankle	Ipsilateral (deg)	14.90 ± 2.16	23.18 ± 1.10	0.0051
		Contralateral (deg)	20.56 ± 1.34	19.00 ± 1.45	0.45
	Knee	Ipsilateral (deg)	71.74 ± 2.88	59.18 ± 1.10	0.0015
		Contralateral (deg)	53.02 ± 2.60	57.26 ± 2.48	0.32#
	Hip	Ipsilateral (deg)	43.57 ± 4.80	46.10 ± 4.19	0.70
		Contralateral (deg)	49.49 ± 4.55	42.38 ± 1.46	0.16
Max (AMI)	Ankle	Ipsilateral (deg)	n.a.	24.62 ± 0.93	0.0014
		Contralateral (deg)	n.a.	20.83 ± 1.35	0.89
	Knee	Ipsilateral (deg)	n.a.	62.10 ± 1.44	0.011
		Contralateral (deg)	n.a.	57.49 ± 2.38	0.23
	Hip	Ipsilateral (deg)	n.a.	51.80 ± 3.37	0.19
		Contralateral (deg)	n.a.	49.62 ± 1.55	0.98
Slope adaptations					
Decline	Ankle	Ipsilateral (deg)	13.81 ± 2.18	17.61 ± 1.92	0.21#
		Contralateral (deg)	16.81 ± 1.49	16.50 ± 1.64	0.89
	Knee	Ipsilateral (deg)	71.37 ± 3.89	58.35 ± 3.56	0.030
		Contralateral (deg)	55.30 ± 3.04	59.10 ± 4.66	0.51
	Hip	Ipsilateral (deg)	26.21 ± 2.06	30.44 ± 3.72	0.34
		Contralateral (deg)	26.51 ± 3.13	31.88 ± 3.04	0.24
Incline	Ankle	Ipsilateral (deg)	14.52 ± 2.28	25.68 ± 0.57	<0.001#
		Contralateral (deg)	21.91 ± 1.95	20.94 ± 0.78	0.65
	Knee	Ipsilateral (deg)	60.30 ± 3.36	52.34 ± 3.45	0.12
		Contralateral (deg)	48.66 ± 2.44	53.79 ± 3.86	0.28
	Hip	Ipsilateral (deg)	44.73 ± 3.78	48.05 ± 5.71	0.64
		Contralateral (deg)	46.32 ± 3.57	48.41 ± 4.35	0.72
Stair adaptations					
Descent	Ankle	Ipsilateral (deg)	12.44 ± 2.22	19.96 ± 2.24	0.034
		Contralateral (deg)	38.18 ± 2.69	37.29 ± 1.97	0.79
	Knee	Ipsilateral (deg)	96.00 ± 3.40	70.45 ± 4.94	0.0011
		Contralateral (deg)	77.88 ± 3.94	72.00 ± 4.69	0.36
	Hip	Ipsilateral (deg)	27.40 ± 4.17	27.33 ± 4.00	0.99
		Contralateral (deg)	30.24 ± 2.79	31.87 ± 3.91	0.74
Ascent	Ankle	Ipsilateral (deg)	12.41 ± 1.82	24.00 ± 0.58	<0.001
		Contralateral (deg)	24.82 ± 2.05	26.94 ± 1.42	0.41
	Knee	Ipsilateral (deg)	81.98 ± 5.81	71.38 ± 3.44	0.14
		Contralateral (deg)	76.70 ± 4.09	75.61 ± 5.59	0.88
	Hip	Ipsilateral (deg)	66.66 ± 5.72	55.96 ± 3.06	0.12
		Contralateral (deg)	53.66 ± 6.49	55.80 ± 4.15	0.79

The range of motion (ROM) for ankle, knee, and hip joints of ipsilateral and contralateral extremities. The ROM of the maximum (max) AMI walking was compared to that of the max CTL walking. For data that violated normality, Mann–Whitney U tests (#) was used, unpaired *t* tests for other comparisons (n = 7 per cohort). Mod, moderate; n.a., not applicable.

Muscle Afferents and Neuroprosthetic Gait

To investigate the relationship between muscle afferents and the evolution of biomimetic gait, the muscle afferents within residuum were estimated using a computational model[80,81] based on muscle fascicle strains and EMG signals, which were recorded using ultrasound imaging and surface electrodes, respectively (Figure 14). The agonist-antagonist muscle afferents were computed to evaluate the overall muscle afferent signaling capacity for ankle control. These afferents were calculated as the difference between antagonistic (lengthening) and agonistic (shortening) afferents for the TA and GAS muscle pair. As expected, the results showed that the AMI subjects had significantly larger agonist-antagonist muscle afferents (10.5 ± 0.88 Imp s^{-1}) compared to the CTL subjects (0.09 ± 0.69 Imp s^{-1}; $n = 7$ per cohort, unpaired t test, $P < 0.001$). Therefore, the AMI and CTL groups exhibited significantly different levels of residual muscle proprioceptive afferents. Meanwhile, it should be noted that the muscle afferents in the AMI subjects were only 17.5% of the biologically-intact values (approximately 60 Imp s^{-1} [17,80,81]).

Next, the torque-angle trajectories were compared at maximum walking speeds for the CTL and AMI cohorts, along with corresponding values for each cohort's agonist-antagonist afferents (Figure 15a). In the CTL cohort, the torque-angle loop moved in a clockwise direction and dissipated mechanical energy from the gait cycle, while the AMI cohort, possessing only 17.5% of the agonist-antagonist muscle afferents of a biologically-intact limb, showed a torque-angle loop that mimicked that of an intact limb, moving in a counterclockwise direction and injecting net positive work into the walking gait cycle. Strong correlations (r) were found between bionic ankle peak power ($r = 0.88$, $n = 14$, $P < 0.001$), net work ($r = 0.78$, $n = 14$, $P = 0.0011$), LEK symmetry ($r = 0.83$, $n = 14$, $P < 0.001$), maximum walking speed ($r = 0.85$, $n = 14$, $P < 0.001$), and agonist-antagonist muscle afferents (Figure 15b to 15e). Furthermore, substantial differences were observed between the AMI and CTL cohorts in torque-angle mechanics for slope and stair adaptations (Figure 16), as well as significant correlations between bionic control metrics and the agonist-antagonist muscle afferents ($|r| = 0.56$-0.84, $n = 14$, $P < 0.035$) (Figure 16 and Table 6). These results suggest that even a modest increase in residual limb muscle afferents can enable biomimetic gait under full neural control.

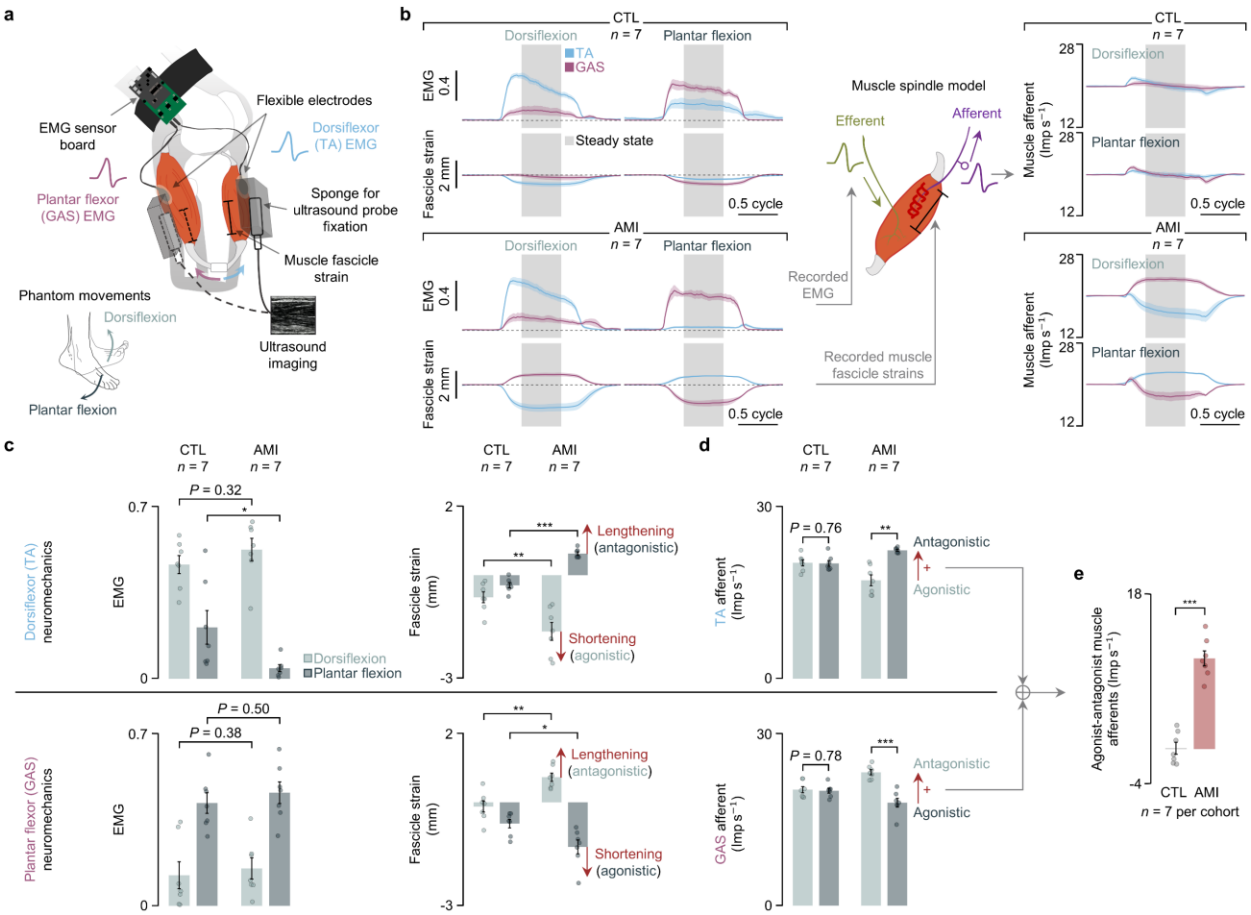

Figure 14 | Residual muscle neuromechanics. a, Assessment of residual muscle neuromechanics. **b**, Estimation of muscle afferents. Profiles of the recorded EMG, muscle fascicle strains, and estimated muscle afferents for each cohort are reported (bolded lines, mean; shaded regions, SEM). **c**, EMG and muscle fascicle strain during the steady state of the phantom ankle movements (bars, mean; error bars, SEM). Significantly larger agonistic shortening and antagonistic lengthening were found in the AMI compared to those of the CTL cohort. **d**, Estimated muscle afferents (bars, mean; error bars, SEM). The AMI dorsiflexor and plantar flexor produce significantly larger muscle afferents when each muscle works as an antagonist (lengthening) compared to when it works as an agonist (shortening). Significant differences between dorsiflexor TA and plantar flexor GAS afferent signaling are found in the AMI but not the CTL cohort. **e**, The agonist-antagonist muscle afferents in AMI subjects were significantly higher than in CTL subjects. In four out of the seven CTL subjects, muscle afferents actually *increased* when working as an agonist, yielding negative values for agonist-antagonist muscle afferents. For these analyses, Mann–Whitney U test was used for the GAS EMG comparison during DF, paired and unpaired *t* tests for other within and between group comparisons, respectively ($n = 7$ per cohort, $*P < 0.05$, $**P < 0.01$, $***P < 0.001$).

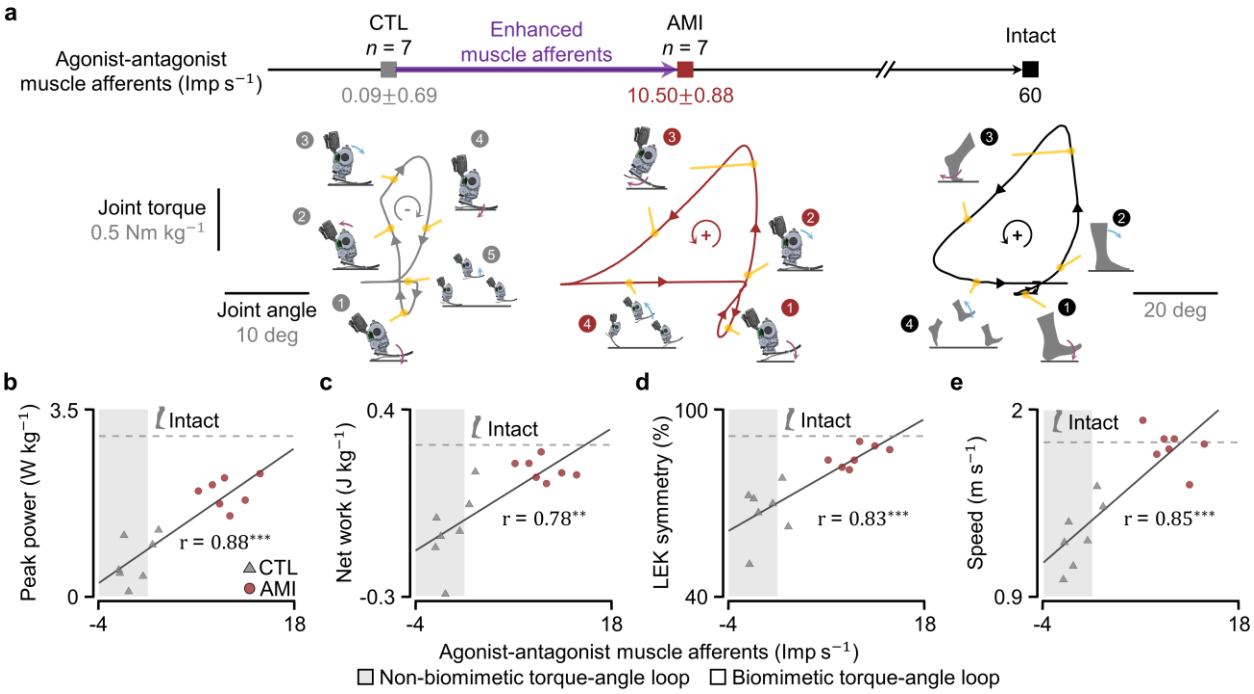

Figure 15 | Enhanced muscle afferents enable biomimetic gait. a, For the CTL and AMI cohorts, averaged torque-angle trajectories at maximum walking speeds are plotted below their corresponding levels of agonist-antagonist muscle afferents (mean ± SEM). For comparison, a torque-angle trajectory and corresponding level of agonist-antagonist muscle afferents are shown on the right for a group of biologically-intact limbs[33,80]. **b-e**, For CTL and AMI subjects walking at maximum speed, positive correlations are shown between agonist-antagonist muscle afferents and peak power (**b**), net work (**c**), lower-extremity kinematic (LEK) symmetry (**d**), and walking speed (**e**). Pearson correlations (r) are reported (n = 14, $^{**}P < 0.01$, $^{***}P < 0.001$). For comparison, values for each biomechanical metric from a biologically-intact population are indicated by dashed lines[75,84,86].

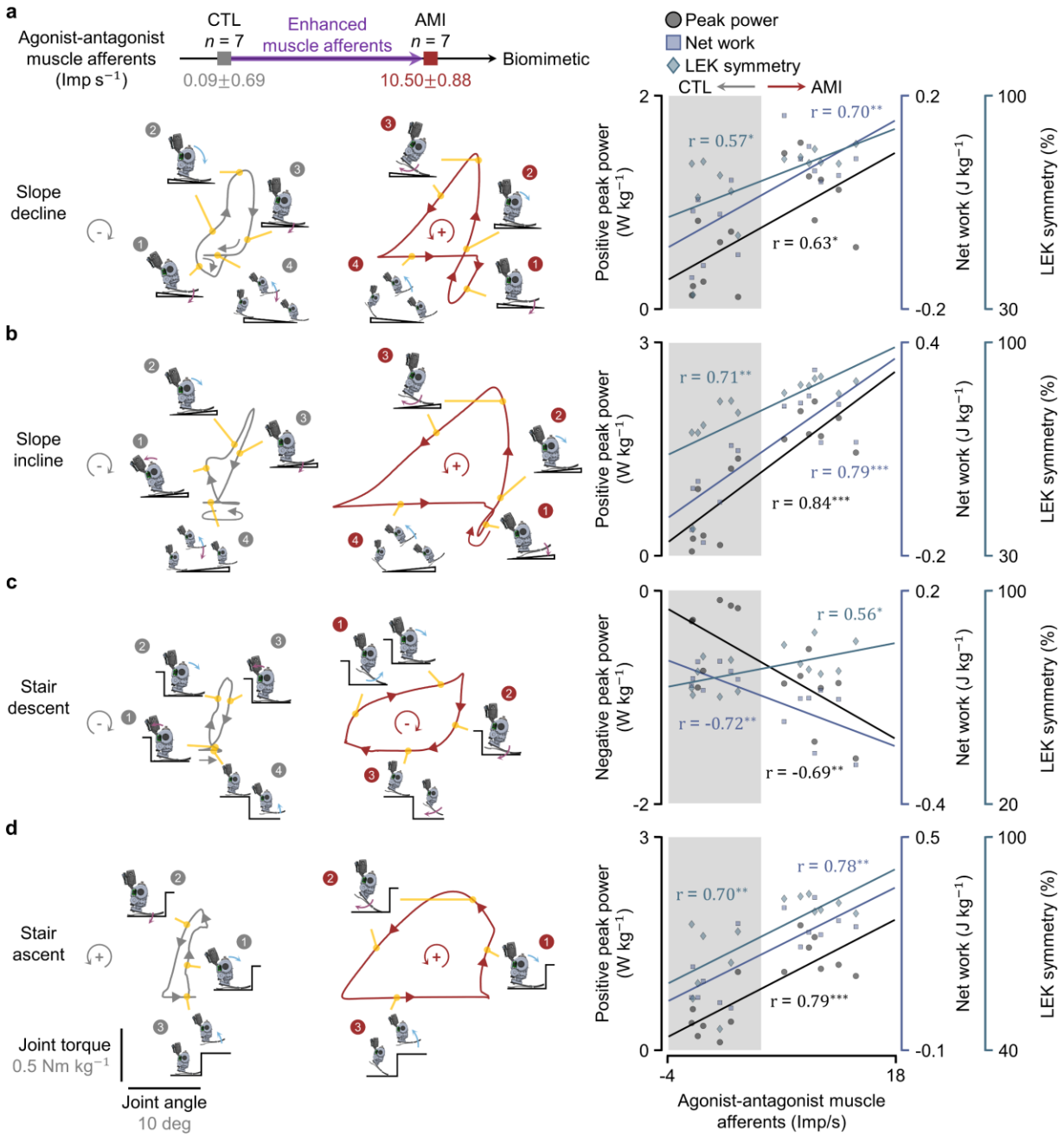

Figure 16 | Bionic terrain adaptation at varying levels of muscle afferents. a-d, Averaged torque-angle trajectories at the slope decline (**a**), slope incline (**b**), stair descent (**c**), and stair ascent (**d**) are plotted for CTL and AMI cohorts with a corresponding value for each cohort's agonist-antagonist muscle afferents (mean ± SEM). In addition, peak power, net work, and lower-extremity kinematic symmetry at each slope and stair adaptation are plotted against agonist-antagonist muscle afferents in a combined analysis of all subjects. Negative peak power values are reported for stair descent, whereas positive peak power values are reported for all other conditions. Net work during weight acceptance and step-up are reported for stair descent and ascent, respectively. Pearson correlations (r) are reported (n = 14, *P < 0.05, **P < 0.01, ***P < 0.001).

Table 6 | Correlations between bionic control metrics and muscle afferents

		Pearson correlation (r)	*P*-value
Level-ground walking			
Max (CTL)/max (AMI)	Peak power (W kg^{-1})	0.88	<0.001
	Net work (J kg^{-1})	0.78	0.0011
	LEK symmetry (%)	0.83	<0.001
Slope adaptations			
Decline	Peak power (W kg^{-1})	0.63	0.015
	Net work (J kg^{-1})	0.70	0.0049
	LEK symmetry (%)	0.57	0.034
Incline	Peak power (W kg^{-1})	0.84	<0.001
	Net work (J kg^{-1})	0.79	<0.001
	LEK symmetry (%)	0.71	0.0044
Stair adaptations			
Descent	Peak power (W kg^{-1})	-0.69	0.0069
	Net work (J kg^{-1})	-0.72	0.0034
	LEK symmetry (%)	0.56	0.035
Ascent	Peak power (W kg^{-1})	0.79	<0.001
	Net work (J kg^{-1})	0.78	0.0011
	LEK symmetry (%)	0.70	0.0049

Concluding Remarks

This chapter presents the first neuroprosthetic leg fully driven by the human nervous system and capable of biomimetic gait. The locomotory testing on level-ground was extended to real-world environments, including slopes and stairs. Previous studies on other types of neural prostheses have demonstrated clinically-relevant improvements with only modest levels of afferent restoration. For example, early cochlear implants restored speech recognition, albeit with limited resolution. The results presented here show that even a small level of muscle afferent augmentation can significantly impact functional restoration of gait, including mechanical energetics, gait symmetry, walking speed, and terrain adaptability. These findings could guide further advancements in surgical reconstruction and neural interfacing technologies to achieve even greater levels of afferent restoration and biomimetic gait. The technological frameworks used in this study could also be applied to the neuroprosthetic integration of a wide range of wearable devices, from upper-extremity bionics to exoskeletal limbs. Given the technological challenges associated with complete afferent restoration, the findings suggest that partial reinstatement may be sufficient to enable clinically-significant improvements in neuroprosthetic functionality.

Chapter 4. Demonstration of neuroprosthetic gait responsive to environmental perturbation

The integration of surgical and neural prosthetic technologies has enabled individuals to achieve biomimetic neuroprosthetic gait in well-controlled laboratory conditions. However, in real-world scenarios, users must be able to react to complex environmental perturbations. This chapter introduces a neuroprosthetic leg that enables individuals with below-knee amputation to continuously control a prosthetic ankle to smoothly cross and recover from an obstacle during walking without any intrinsic state-machine or classification of the gait event or environment. The approach involves augmenting muscle afferents in the residual limb through AMI, which reconstructs natural agonist-antagonist muscle dynamics. Presented experiments with ten individuals with below-knee amputation demonstrate that greater augmentation of residual muscle afferents enables more biomimetic kinematic reactions, followed by greater propulsive kinetics during obstacle crossing and recovery steps. These adaptive features allow individuals with the neural augmentation to walk at higher speeds on obstructed paths compared to those without the augmentation. The results suggest that enhancing residual muscle afferents in combination with neural prosthetic limbs enables individuals to respond effectively to complex environmental perturbations.

Rationale and Study Design

The translation of bionic limb technology to real-world conditions necessitates consistent and robust responses to complex environmental perturbations[1]. Stepping over obstacles while walking is a representative perturbation response that requires close interaction between supraspinal anticipatory adjustment and spinal reflexive control[87,88]. The work presented in this chapter hypothesizes that a myoneural interface that provokes higher muscle afferent signaling, such as the AMI, will facilitate a more rapid and higher degree of biomimetic reaction to perturbation in neural prosthetic gait. To test this hypothesis, ten participants with below-knee amputation were instructed to walk at their maximum self-selected speed while traversing an obstructed path at a steady pace. The study involved (i) integration of the myoneural interface and neural prosthetic system, (ii) evaluation of neural prosthetic gait with and without obstacle crossing (perturbed and unperturbed walking), and (iii) combined analyses with biophysical clinical data (agonist-antagonist muscle afferents) addressed in the previous chapter to investigate the relationship between varying levels of enhanced muscle afferents and neural prosthetic reaction to perturbation during gait. Statistical group comparisons were performed between non-AMI (CTL) and AMI cohorts to demonstrate the efficacy of surgical strategies augmenting afferent feedback, such as the AMI, in improving neural prosthetic gait. The results reveal that enhancing residual muscle afferents enables more biomimetic and rapid reaction to complex environmental perturbation.

Methods

Patient Selection and Bionics

In order to evaluate the ability of the bionic system to respond to environmental perturbations, an exploratory perturbed walking trial was conducted on a subset of participants previously described (n = 10, CTL 1-6 and AMI 1-4; Table 3). The experimental protocol and control methods were consistent with those described in the preceding chapter.

Perturbed Walking Experiment

In this study, the neural control of the bionic ankle during the obstacle step crossing and the recovery step was assessed (Figure 17). As an environmental obstacle, a stiff sponge measuring 0.21 m in height and wide (thickness = 0.08 m, width = 0.91 m) was utilized. Participants were instructed to walk at their maximum self-selected speed, which they felt comfortable traversing over the obstacle at a steady pace. Twelve gait cycles were collected for each obstacle crossing and recovery step with the bionic ankle in the leading position. Baseline data for unperturbed walking were also collected to provide within-subject analyses.

Neural Prosthetic Control Metrics and Muscle Afferents

The biomimetic bionic response was evaluated by determining the average increase in bionic ankle angle during the swing phase compared to that of unperturbed walking. To evaluate the propulsive mechanics for rapid gait recovery, we used the bionic ankle net work during the recovery step. A video camera (Canon EOS 5D Mark III, Canon, Japan) recorded the sagittal plane view of the individuals performing perturbed walking to estimate the travel distance from

the start of the obstacle crossing swing phase to the end of the recovery step stance phase. The perturbed walking speeds were computed from the travel distance and time. To evaluate the biomimetic response of the bionic ankle to environmental perturbation, the average increase in bionic ankle angle during the swing phase was calculated and compared to unperturbed walking. The propulsive mechanics for rapid gait recovery were assessed by analyzing the bionic ankle net work during the recovery step. The travel distance from the start of the obstacle crossing swing phase to the end of the recovery step stance phase was estimated using a video recording (Canon EOS 5D Mark III, Canon, Japan) of the sagittal plane view of individuals performing perturbed walking. Perturbed walking speeds were computed from the travel distance and time, allowing for a quantitative assessment of the perturbed walking trial. Correlation analyses were conducted to examine the association between subject-specific neural prosthetic control metrics and residual muscle afferents utilizing data from the previous chapter.

Index of Gait Recovery Performance

The speed-accuracy tradeoff in human motor control, also known as Fitt's law[49–51], is observed in various motor tasks. To evaluate an individual's motor control performance while considering the speed-accuracy tradeoff, the index of performance (IP) has been widely used[89,90]. The IP involves the logarithm of the reciprocal of error metrics (accuracy metrics) divided by movement time. It provides insight into the speed of information transmission rate between the human nervous system and the computer interface of interest. In this study, the IP was modified to evaluate gait recovery performance while considering the speed-accuracy tradeoff (index of gait recovery performance, IGRP). The dissimilarity between the ankle kinematics of the recovery step and unperturbed walking was utilized as new error metrics. The dissimilarity was computed using the symmetry index (SI)[75]. The movement time was replaced by the average travel time for a unit distance (1 m) computed by the individual's perturbed walking speed. Therefore, IGRP was defined as

$$\mathrm{IGRP} = \frac{V_p}{1\ \mathrm{m}} \log_2\left(\frac{1}{\mathrm{SI}} + 1\right)$$

where V_p is individual's perturbed walking speed. Meanwhile, because SI is a dissimilarity metric[75], gait recovery is computed as 100(1-SI)%.

Statistics

The results of the prosthetic mechanics and control metrics were reported as mean ± standard error of the mean (SEM). The normality of the data was verified using the Shapiro-Wilk test at a significance level of $\alpha = 0.05$. Two-sided unpaired t-tests were used to compare the groups. Pearson correlations (r) and *P* values were reported for the correlation analyses between prosthetic control metrics and agonist-antagonist muscle afferents. All statistical analyses were performed using MATLAB 2020b (Mathworks, USA).

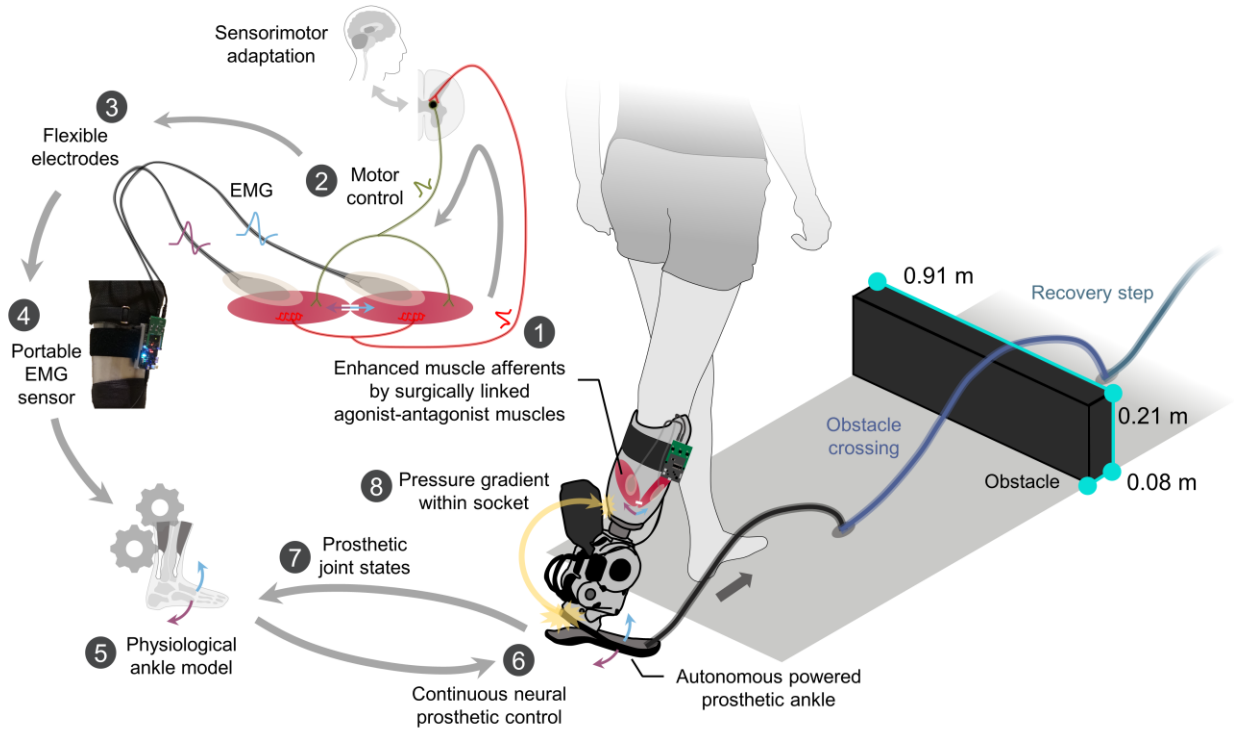

Figure 17 | Schematic diagram of perturbed walking. To evaluate the responsiveness of the neuroprosthetic system to environmental perturbations, each participant was instructed to walk over an obstructed pathway. The trial utilized the same bionic system described in the previous chapter, and the bionic mechanics were analyzed during two consecutive steps: the obstacle crossing step and the subsequent recovery step. In addition, the bionic mechanics during walking without obstacle were analyzed for baseline evaluation.

Results and Discussion

Neuroprosthesis Responsive to Perturbation

Neuroprosthetic control during perturbed walking is shown in Figure 18. Compared to their unperturbed walking, individuals with intact limbs increase their foot clearance during the swing phase of obstacle crossing[88]. All AMI subjects demonstrated an increase in bionic ankle foot clearance angle during obstacle crossing (4.14 ± 0.66 deg) (Figure 19a), while a significantly smaller increase was observed in CTL subjects (-0.45 ± 0.87 deg; n = 6 CTL, n = 4 AMI, unpaired t test, P = 0.0052) (Figure 19b). In four of the six CTL subjects, the foot clearance angle actually decreased. This type of dysfunctional motor response is known to occur in people living with cerebral palsy[91] and Parkinson's disease[92] and is attributed to disordered supraspinal and spinal locomotor pathways involving peripheral afferents[92–94]. These populations also experience high rates of injury and morbidity from falling[92]. During the recovery step, the AMI subjects produced propulsive walking kinetics (0.125 ± 0.022 J kg^{-1}) (Figure 19c), corresponding to an 881% increase compared to CTL subjects (-0.016 ± 0.018 J kg^{-1}; n = 6 CTL, n = 4 AMI, unpaired t test, P = 0.0011) (Figure 19d). The propulsion enabled the AMI cohort to traverse the perturbation at a walking speed of 0.94 ± 0.05 m s^{-1}, which was 54.1% faster than the CTL

cohort (0.61 ± 0.06 m s^{-1}; n = 6 CTL, n = 4 AMI, unpaired t test, P = 0.0049) (Figure 19e). Additionally, a significant correlation was found between responsive bionic control metrics during perturbed walking and the agonist-antagonist muscle afferents (r = 0.75-0.82, n = 10, P < 0.013) (Figure 19f to 19h). These findings demonstrate the effectiveness of augmenting residual limb muscle afferents in enabling human users of the neuroprosthesis to respond to real-world environmental perturbations.

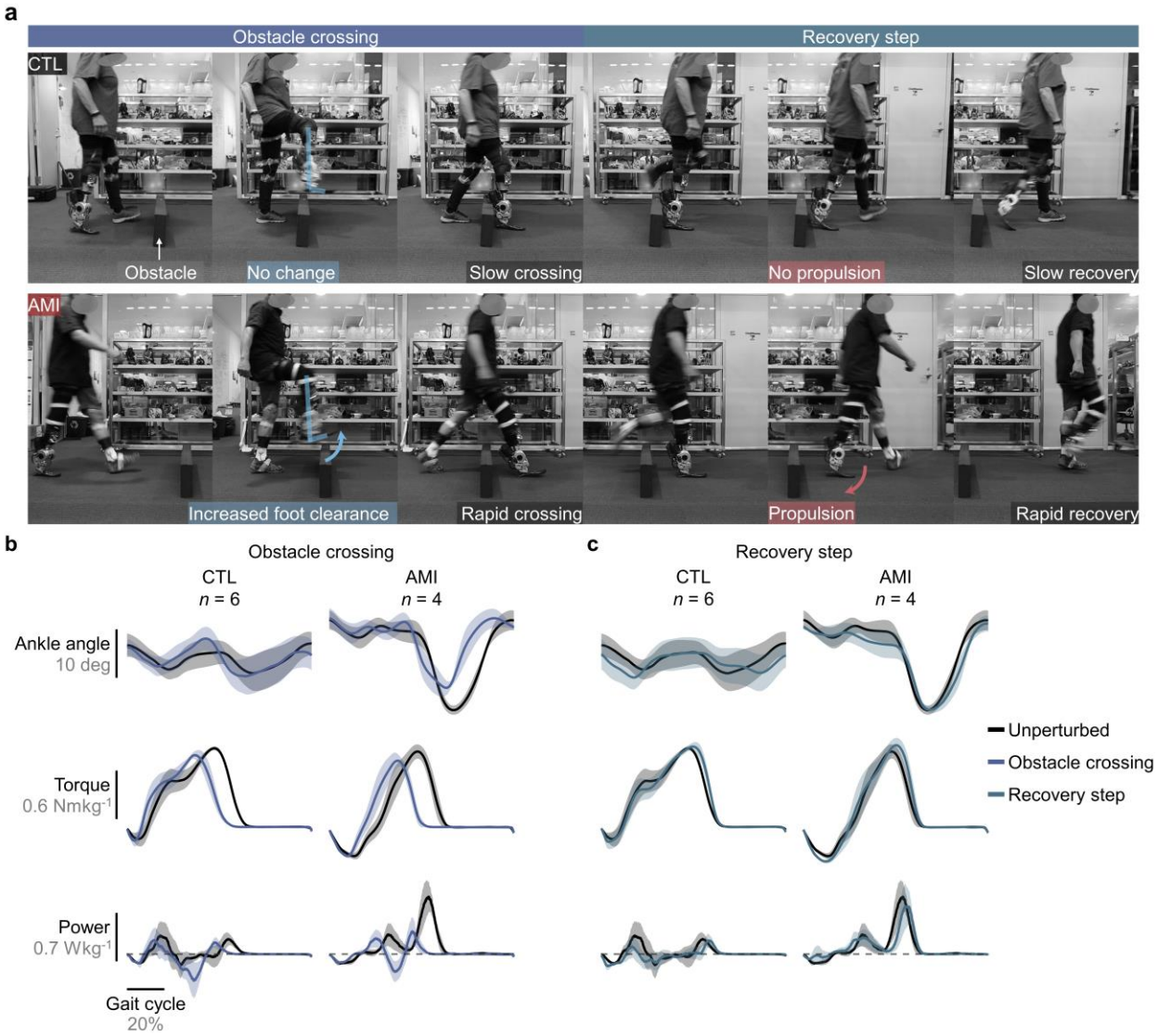

Figure 18 | Bionic mechanics during the perturbation response. a, Shown is an obstacle crossing test chronophotography. **a**, **b**, Bionic mechanics during obstacle crossing (**a**) and recovery step (**b**) are compared with those of walking on an unobstructed path (bolded lines, mean; shaded regions, SEM).

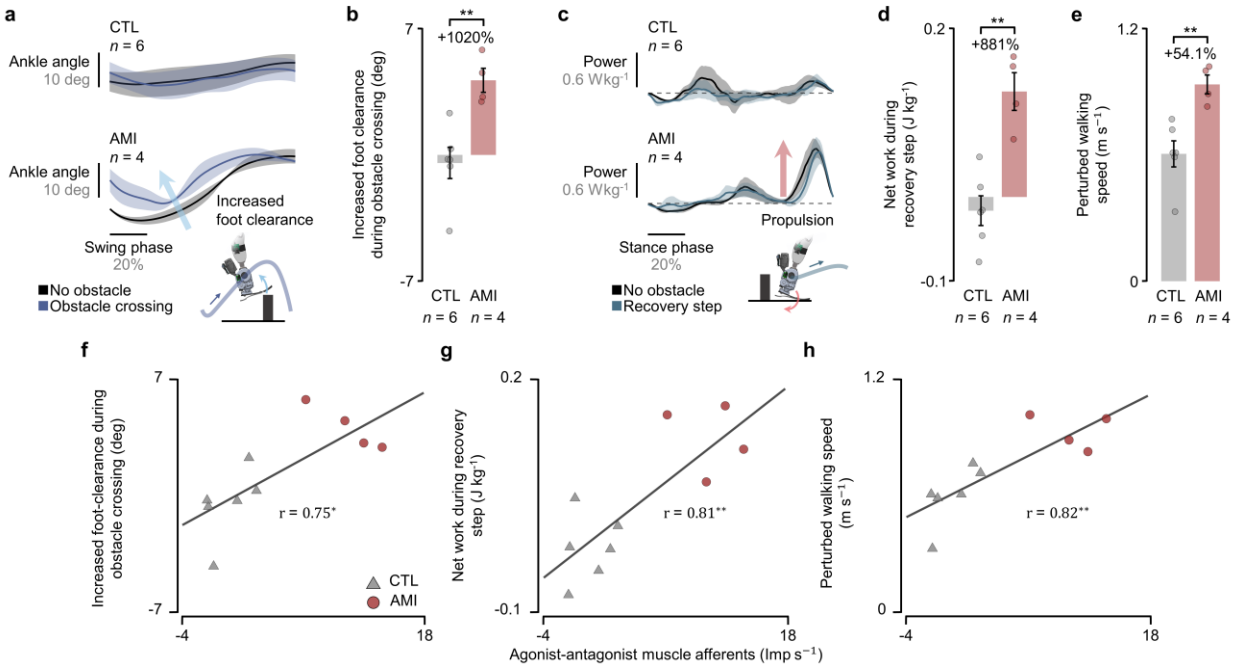

Figure 19 | Bionic response to perturbation at varying levels of muscle afferents. **a**, Comparison of bionic swing phase during obstacle crossing and unobstructed walking is plotted (bolded lines, mean; shaded regions, SEM). **b**, CTL and AMI subjects increased foot clearance is shown during obstacle crossing (bars, mean; error bars, SEM). **c**, Comparison of bionic stance phase during recovery step and unobstructed walking is shown (bolded lines, mean; shaded regions, SEM). **d**, CTL and AMI subjects' net work is plotted during the recovery step (bars, mean; error bars, SEM). **e**, Perturbed walking speed for CTL and AMI cohorts are shown. For these analyses, unpaired *t* tests were used ($n = 6$ CTL and $n = 4$ AMI, $^{**}P < 0.01$). **f-g**, Increased foot clearance during obstacle crossing (**f**), net work during recovery step (**g**), and perturbed walking speed (**h**) are plotted against agonist-antagonist muscle afferents in a combined analysis of all participants. Pearson correlations (r) are reported ($n = 10$, $^{*}P < 0.05$, $^{**}P < 0.01$).

Information Transmission between a Bionic Leg and Nervous System

The figure 20a shows the gait recovery and walking speed of AMI and CTL participants, along with their index of gait recovery performance (IGRP) levels. All AMI participants had data located in the top-right plane, indicating that they were able to recover their gait kinematics quickly and accurately after perturbation. In contrast, the data for the CTL participants varied in the left-half plane, indicating that they either recovered their gait kinematics slowly or walked fast without recovering kinematics. From an information theory perspective, this speed-accuracy tradeoff is limited by the information transmission rate between the human and the interface. The information transmission rate was evaluated using the IGRP, as described in the Methods and shown in Figure 20b. A significant positive correlation was found between IGRP during perturbed walking and the agonist-antagonist muscle afferents (r = 0.84, n = 10, P < 0.01). Representative kinematics of two subjects shown in Figure 20c, corresponding to the top-right and bottom-left subjects, respectively, exhibited these features. These results demonstrate that augmenting residual muscle afferents allows for higher integration between the human nervous system and neuroprosthetics, resulting in higher information transmission and enabling a higher level of neural responses.

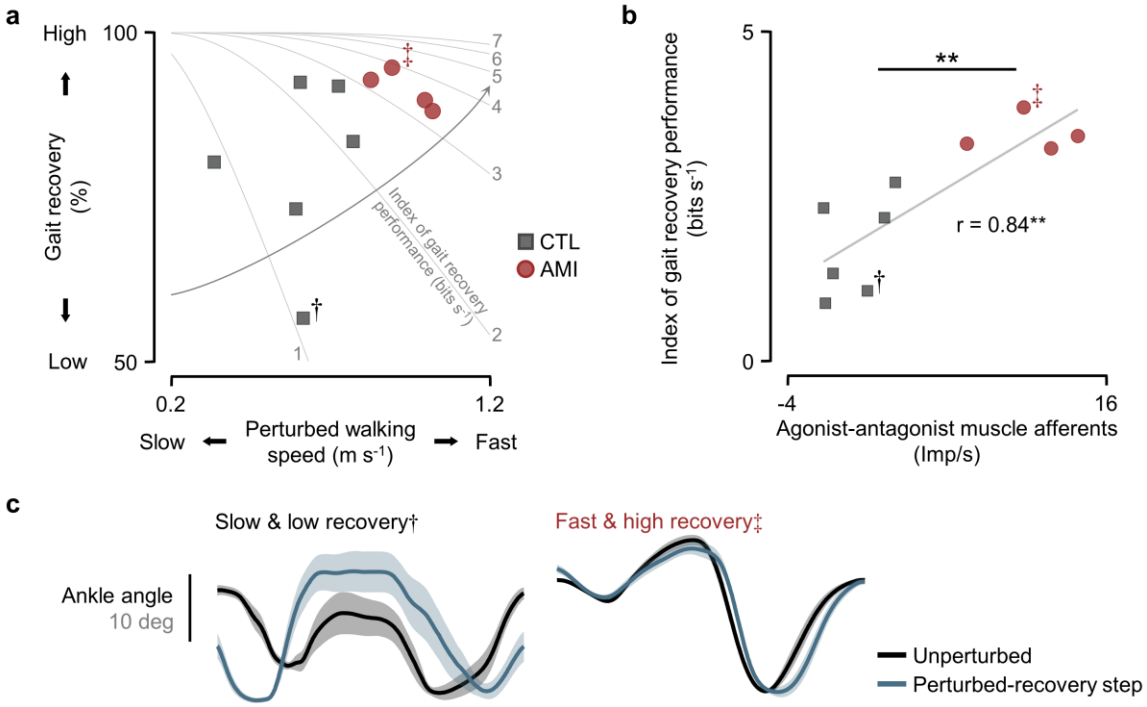

Figure 20 | Enhanced muscle afferents enable fast information transmission. a, Gait recovery and perturbed walking speed of the study population. Index of gait recovery performance is computed based on speed-accuracy tradeoff found in human motor behaviors (Fitts' law). **b**, Index of gait recovery performance at varying levels of agonist-antagonist muscle afferents. Pearson correlation (r) is reported and unpaired t-test was used for a between group comparison. (n = 10, **P < 0.01). **c**, Representative kinematics of recovery step compared with those of unperturbed walking at varying levels of gait recovery performance (slow and low recovery †, fast and high recovery ‡; bolded lines, mean; shaded regions, SEM).

Concluding Remarks

This chapter describes the development of the first neuroprosthetic leg that can respond to environmental perturbations under full neural control. The study shows that individuals are able to quickly recover from complex environmental disturbances using the neuroprosthesis. The analysis of bionic performance and neuromechanical data supports the idea that even partial muscle afferent augmentation can enable stable and robust neuroprosthetic gait. This highlights the effectiveness of the surgical strategy, such as AMI, in restoring high-fidelity bionic control in real-world scenarios.

Chapter 5. Development of Fatigue Resistant Myoneural Actuators for Mechanoneural Interfaces

Mechanoneural interfaces that modulate the mechanoneural transduction of sensory organs present a promising paradigm for enabling bi-directional communication between humans and neuroprosthetic systems. However, the development of such interfaces is subject to significant challenges, not least of which is the requirement for actuators that are self-sustainable in biological systems and exhibit high biocompatibility. In view of these constraints, hijacking neural control of a native muscle presents a viable means of providing the actuation necessary for mechanoneural interfaces. Nonetheless, muscles fatigue under continuous actuation, thereby restricting the fundamental capability of muscle-actuated systems. This chapter presents a myoneural mechanism that transforms a muscle into a fatigue-resistant actuator, surpassing the capabilities of its native form. The mechanism involves the augmentation of a fatigue-resistance through the reinnervation of a cutaneous nerve that possesses more uniform axon sizes than a motor nerve. Using a rodent model, the work demonstrates that fatigue resistance is enhanced by 260% under continuous actuation compared to a native muscle. Additionally, the work integrates the actuator with nerve block technology, demonstrating electrophysiologically isolated actuation. To illustrate the potential impact of the actuator technology, a novel neuroprosthetic interface, the Proprioceptive Mechanoneural Interface (PMI), is designed which utilizes the myoneural actuator to modulate proprioceptive afferents from a residual muscle. The technology provides design freedom, which enables the embedding of active mechanical design into biological systems for future mechanoneural interfaces.

Rationale and Study Design

Mechanoneural transduction is a ubiquitous principle of sensory feedback in the human body[95,96], whereby neural signaling is generated by deformation of sensory organs such as muscle and skin receptors[16,31]. The development of mechanoneural interfaces that emulate such sensory organ deformation through an actuator would enable direct control of sensory feedback and facilitate bi-directional communication between prosthetic limbs and the human nervous system. However, designing synthetic actuators with long-term biocompatibility, flexibility (impedance matching), and self-sustainability within biological systems poses a significant challenge[97–100]. A potential solution is to design a myoneural actuator that employs a biological muscle as the basis for actuation, supplemented with minimal synthetic components such as a nerve cuff for control. The predominantly biological composition of myoneural actuators makes them less prone to biocompatibility issues, and the self-healing properties of biological systems offer considerable advantages for maintaining actuation mechanisms within the human body. However, the fundamental capability of myoneural actuators is restricted by muscle fatigue under continuous contraction[101,102], limiting operation time and mechanical output of muscle actuated systems[103]. The absence of a myoneural technique that enhances fatigue resistance is currently impeding the advancement of mechanoneural interfaces.

This chapter introduces a myoneural framework for creating fatigue-resistant myoneural actuators, which aims to overcome the limited operational time and mechanical output of conventional myoneural systems. The proposed framework is based on the concept of hijacking biological motor control of a native muscle by denervating it and then reinnervating it with a sensory nerve. This process introduces a nerve to sustain muscle contractility and mass, while disabling biological motor control. The work hypothesizes that the reinnervation of a nerve with different axon sizes could promote an increase in the fatigue-resistive fiber ratio. Specifically, the work utilizes a sensory nerve for reinnervation, as it is known to have smaller and more uniformed axon sizes compared to motor nerves[104–106]. Electrophysiologically isolated myoneural actuation is achieved by controlling the myoneural actuator through proximal nerve stimulation while simultaneously applying nerve block[107–110] distal to the actuator.

To demonstrate the potential of the myoneural actuator technology, this chapter further presents a novel mechanoneural interface called the Proprioceptive Mechanoneural Interface (PMI). The PMI is designed to enable direct modulation of proprioceptive afferents from a residual muscle for neuroprosthetic limbs. In previous chapters, the efficacy of the surgical strategy of the Agonist-antagonist Myoneural Interface (AMI) was demonstrated in emulating mechanoneural transduction between major flexor and extensor muscle pairs by mechanically coupling them. However, the AMI has a number of limitations in providing biological afferents. For example, the AMI afferent signaling is fixed by the surgical architecture and is affected by various factors such as muscle tension, force capacities, and mechanical impedance. Additionally, the AMI recreates mechanoneural transduction of sensory organs within a residual muscle-tendon by using its agonist muscle, which involves muscle contraction. This prevents the AMI from emulating non-muscular actuated mechanoneural transduction in biologically-intact limbs, such as mechanoneural transduction induced by gravity and inertial forces. To address these limitations, the PMI consists of a serially coupled residual muscle and myoneural actuator pair. The myoneural actuator directly modulates the mechanoneural transduction of sensory end

organs within the residual muscle and can be controlled to generate biological afferents found in biological counterparts. These results highlight the potential impacts of the myoneural actuator in designing complex and functional biohybrid systems.

Methods

Animal Husbandry

The experimental and surgical procedures carried out in this study were approved by the Committee on Animal Care (CAC; protocol 2203000299A007) at the Massachusetts Institute of Technology (MIT) and conducted in accordance with ethical guidelines. The study involved a total of $n = 30$ female Lewis rats (273.6 ± 7.1g body weight). The rats were kept in pairs under a light/dark cycle of 12 hours.

Myoneural Actuator Design and Implementation

This work sought to implement a myoneural actuator by hijacking the neural control of a native muscle in a rodent model (Figure 21). Denervation of a biological muscle is known to result in a loss of contractility[111,112]. To maintain contractility while decoupling the rat's motor control of the muscle, a cutaneous sensory nerve was reinnervated after denervation of the native nerve. It was hypothesized that reinnervating the cutaneous sensory nerve would increase the fatigue resistance of the myoneural actuator in comparison to its native form. It was postulated that the cutaneous sensory nerve, characterized by a more homogeneous distribution of smaller axon sizes[104–106], would induce a reduction in the average size of the muscle fiber population and consequently enhance fatigue resistance. The lateral gastrocnemius muscle (L. GAS) was utilized as the actuator basis, and the sural nerve was used as the cutaneous sensory nerve for reinnervation. An incision of approximately 1.5 cm was made on the lateral side of the tibia to provide access to both the native motor nerve (the tibial nerve) and the sural nerve. Further, a small incision was made in the bicep femoris to surgically expose both nerves. After denervation of a tibial nerve branch to the L. GAS, the proximal tibial nerve end was sutured to a biceps femoris muscle to prevent unintended reinnervation back to the L. GAS. The transected sural nerve was embedded into a muscle pocket made on the L. GAS and sutured to close the pocket. All surgical procedures were conducted in aseptic conditions and under general anesthesia (2% isoflurane).

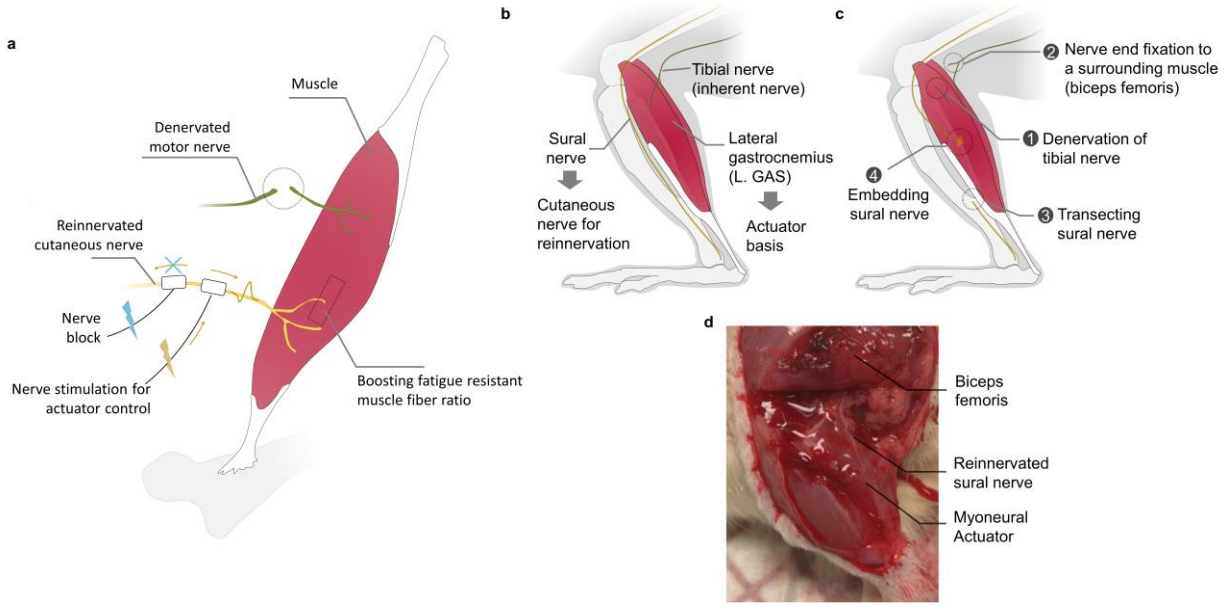

Figure 21 | Myoneural actuator. a, The components of the myoneural actuator are shown in the diagram. To hijack the neural control of biological muscle, an inherent motor nerve is denervated and a cutaneous nerve is reinnervated. Electrical stimulation is applied at the reinnervated cutaneous nerve to control the myoneural actuator. To achieve electrophysiologically isolated actuation, additional electrical nerve block is applied at the distal site of the cutaneous nerve. The work hypothesized that the reinnervated cutaneous nerve would sustain muscle contractility while boost the fatigue-resistant fiber ratio. **b**, **c**, The implementation of the myoneural actuator in rodent models is shown. The lateral gastrocnemius muscle (L. GAS) and sural nerve are used as the actuator basis and cutaneous nerve for reinnervation, respectively (**b**). To prevent unintended reinnervation of the tibial nerve, the proximal tibial nerve end is fixed onto the biceps femoris muscle (surrounding muscle) after transection (**c1**, **c2**). A distal end of the sural nerve is transected (**c3**) and embedded into the L. GAS by inserting the nerve end into a muscle pocket and securing it with suture (**c4**). **d**, The myoneural actuator is shown post-15 weeks.

Assessment of Myoneural Actuator Sustainability

To assess the sustainability of the myoneural actuator, the maximum isometric force and mass of the actuator were evaluated at three different time points, namely 9, 12, and 15 weeks (n = 5 per each time point), alongside additional native muscles (n = 8) for baseline evaluation (Figure 22). All surgical procedures were carried out under general anesthesia (2% isoflurane). A large incision (~ 4 cm) was made on the lateral side of the tibia to expose the myoneural actuator (L. GAS basis) by opening up the biceps femoris. The proximal retraction of biceps femoris provided complete access to the sural and sciatic nerves. The sciatic nerve branches were transected to prevent any undesired activation of surrounding muscles (e.g. tibial anterior or soleus) due to potential current leakage during electrical stimulation. The surrounding tissues of the sural nerve were cleared to secure space to place a hook electrode, and the Achilles tendon was transected as distally as possible to separate the myoneural actuator from the medial

gastrocnemius (M. GAS). The animal was then moved to the experimental apparatus, which consisted of a heated bed and a force transducer (305C-LR, Aurora Scientific, USA). A patellar tendon and anterior talofibular ligament were sutured to the heated bed to mechanically ground the limb firmly, and the distal tendon of the myoneural actuator was sutured to the force transducer lever. Targeted electrical stimulation was applied through a hook electrode placed on the sural nerve. To assess the maximum isometric force, a 1 s electrical nerve stimulation (IZ2, Tucker-Davis Technologies, USA) was applied at 70 μA, 40 Hz with incremental pulse width (PW) until force saturation was observed. The PW was incremented by 0.05% until it reached 0.25% and then by 0.25% until it reached 1%. Post 1%, PW was incremented by 1% as needed to plateau the output force. The mass of the myoneural actuator or native L. GAS was weighed by harvesting it after the characterization. Both the maximum isometric force and mass were normalized by the total weight of the animal to allow comparisons between cohorts. The maximum isometric force scaling factor to its mass was assessed by normalizing each maximum force normalized by the weight of the actuator or native muscle.

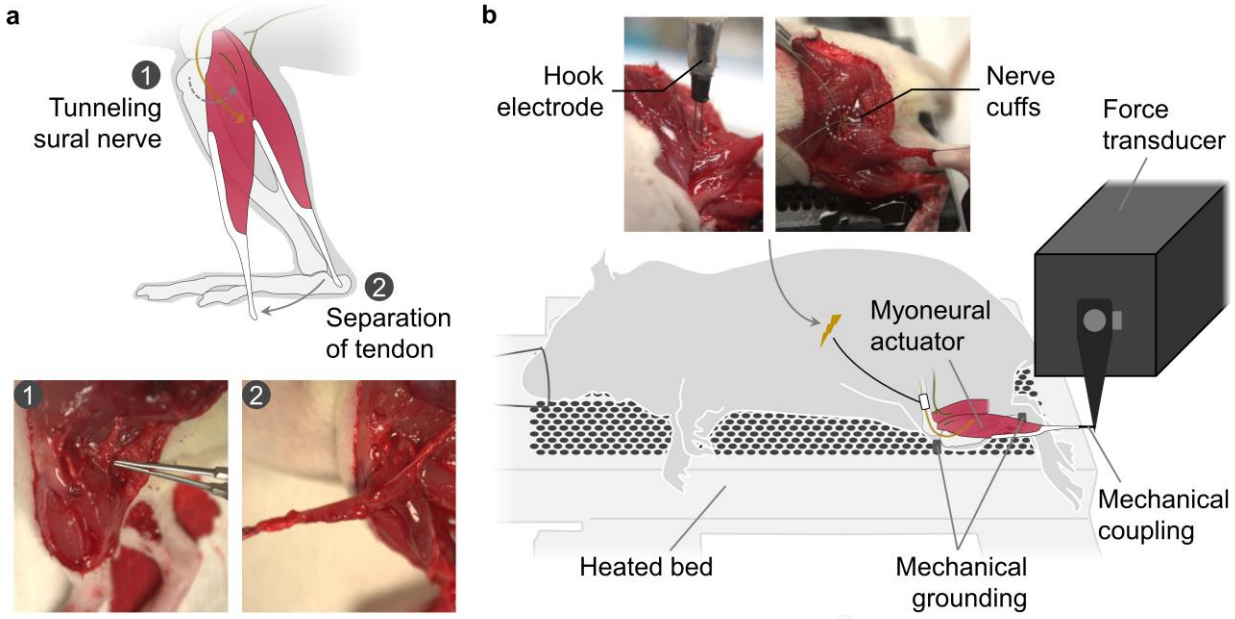

Figure 22 | Experimental setup for actuator characterization. a, Preparation of the myoneural actuator for characterization involved tunneling around the sural nerve to clear and secure spaces for placement of a hook electrode or nerve cuffs (**a1**). The prepared rat was placed on an experimental apparatus comprising a heated bed and force transducer (**a2**). **b**, To conduct force characterization and closed-loop control experiments without nerve block, the patellar tendon and anterior talofibular ligament were mechanically grounded to the heated bed. The myoneural actuator tendon was mechanically coupled to the force transducer. Hook electrodes were used for force characterization, whereas nerve cuffs were used for nerve block validation and closed-loop control experiments with nerve block.

Assessment of Myoneural Actuator Fatigue Responses

The protocol for evaluating fatigue response was carried out in the same manner as the myoneural actuator characterization described in the previous section (Figure 22). Two types of fatigue responses were assessed for both native muscles and myoneural actuators. A series of 1-second-long discrete stimulations was applied at 70 μA, 40 Hz, consisting of incremental pulse width from 0.05% to 15% in increments of 0.05% to 0.25%, and increments of 0.25% to 1%, followed by increments of 1% to 15%. A resting period of 10 seconds was given between stimulations. The average force during the latter half of the stimulation cycle was recorded to determine steady force values. For the fatigue response to continuous stimulation, a 70 μA, 40 Hz stimulus with 4% pulse width was applied for 5 minutes. To facilitate between-group comparisons, the force data was normalized by its maximum values. Fatigue resistance under discrete stimulations was evaluated as the ratio of the final output force to the maximum force during the discrete stimulation sequence. Fatigue resistance under continuous stimulation was evaluated as the time it took for the output force to decrease to 75% of its maximum value (fatigue time).

Closed-Loop Force Control of Myoneural Actuator

To demonstrate the controllability of the myoneural actuator, a closed-loop force control was performed at three different levels: 30%, 50%, and 70% of the maximum output force for both myoneural actuators (n = 8) and native muscles (n = 5). The surgical preparation for this experiment was the same as that used for the myoneural actuator characterization (Figure 22). The maximum output force was determined by gradually increasing the pulse width, as previously described. The pulse width was modulated by proportional control based on the force feedback from the force transducer (305C-LR, Aurora Scientific, USA). Ten consequent output forces were collected for each target force level. The steady state control performance was evaluated based on the average force during the latter half of 0.83 second (1.2 Hz) control periods.

Electrophysiologically Isolated Actuation

To achieve electrophysiologically isolated actuation, it is necessary to block neural afferents that travel to the nervous system, which are inevitably evoked by nerve stimulation for myoneural actuator control. Among various nerve block strategies, the electrical nerve block technique[108–110] was integrated with a myoneural actuator. High frequency electrical stimulation (8 V peak-to-peak voltage, 20 kHz) on the nerve is known to block neural signaling in nerves. Direct validation of nerve block from electroneurography (ENG) recording of afferents was not feasible due to the large stimulation artifact introduced by electrical nerve block. Therefore, nerve block was verified using muscle force outputs similar to previous literature[108–110]. Two nerve cuffs were placed on the sural nerve. To first verify the nerve block effect, nerve block was applied through the proximal nerve cuff to the myoneural actuator while attempting to activate the actuator through the distal nerve cuff. A 2%, 3%, and 4% PW was applied at the distal nerve cuff to test nerve block performance at varying levels of nerve stimulation. The output force under no nerve stimulation was collected for baseline evaluation. Ten cycles of the actuator output force for each condition were recorded. The steady state control performance was evaluated based on

the average force during the latter half of 1 second control periods. For the demonstration of closed-loop force control under nerve block, nerve block was applied at the distal nerve cuff, and the actuator was controlled using the proximal nerve cuff to the actuator. The testing protocol was identical to closed-loop force control without nerve block described previously.

Proprioceptive Mechanoneural Interface (PMI)

PMI was implemented in a rodent model, simulating a residual muscle with medial gastrocnemius (M. GAS) (Figure 23). A myoneural actuator was implemented as described in the previous chapter. The sural nerve was exposed, and the actuator was separated from the M. GAS following the same procedures as for the actuator characterization. However, a tibial nerve branch to the M. GAS was left for afferent recording from the simulated residual muscle. The residual muscle and actuator were then brought to the anterior site of the tibia and surgically coupled using one of the tendons to implement stable mechanoneural actuation. To prevent the conjunction point from slipping proximally towards the knee joint, the other tendon was sutured to distal tissue around the ankle joint to allow for effective mechanoneural actuation when the myoneural actuator was activated. To evaluate the capability of gradual mechanoneural actuation and afferent modulation, a pair of sonocrystals and nerve cuff were placed on the M. GAS and its tibial nerve branch. Muscle strains were recorded at 200 Hz and raw ENG was recorded at 6 kHz. The raw ENG was band-pass filtered (second-order Butterworth filter, pass-band: 300 – 3000 Hz) and the simulation artifact was rejected by blanking the signals for 2 ms based on stimulation triggers. The filtered ENG signals were further rectified-bin-integrated[113] (RBI) during a 4 ms window and smoothed using a moving average filter (250 ms window). A hook electrode was used to deliver stimulation at 70 μA, 40 Hz with varying PW between 2% to 8% (incremented by 2%, n = 10 for each condition) to evaluate the capability of gradual mechanoneural actuation.

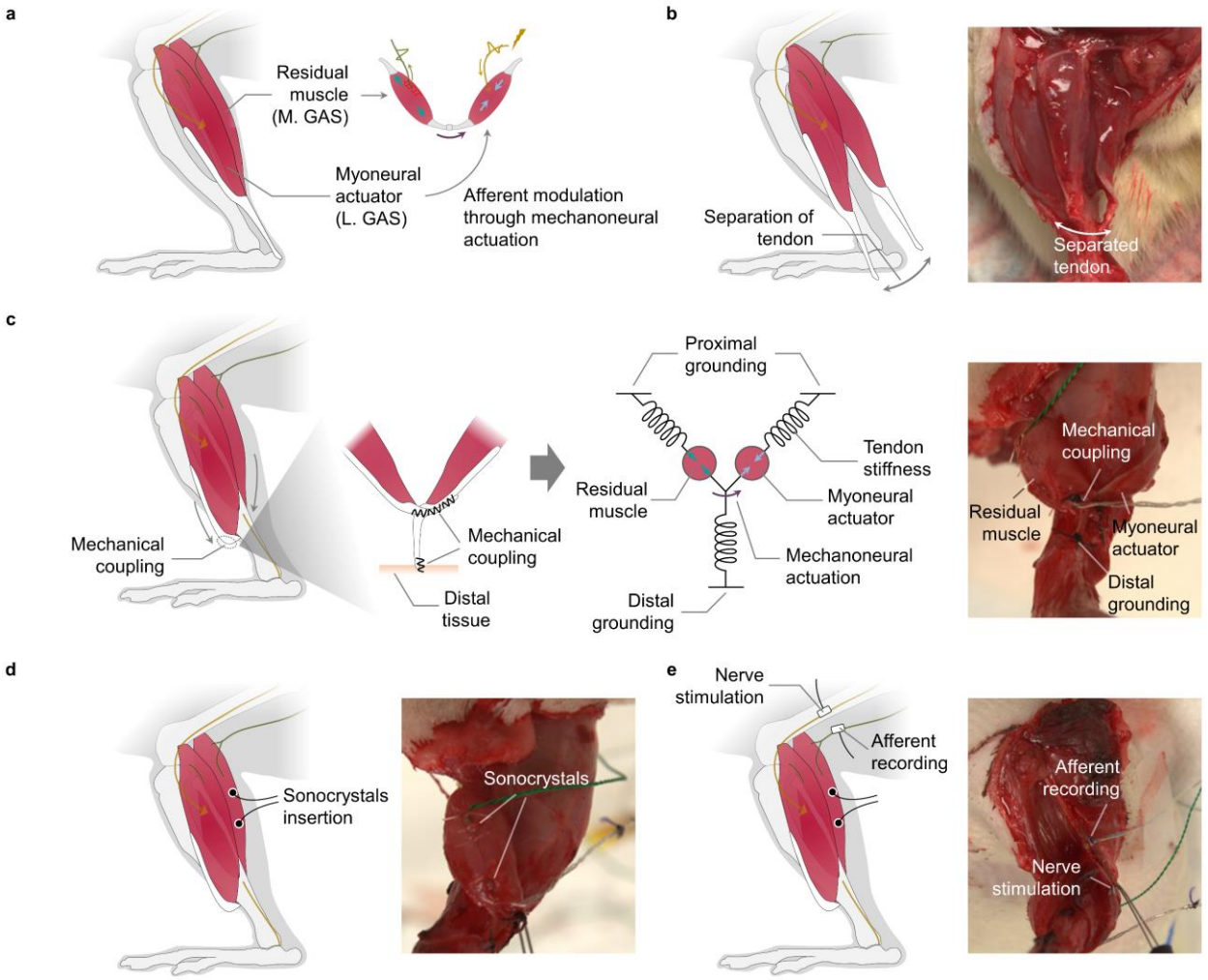

Figure 23 | Proprioceptive Mechanoneural Interface (PMI) implementation. a, Medial and lateral gastrocnemius muscles (M. GAS and L. GAS) are used to simulate residual muscle and myoneural actuator, respectively. The goal of the PMI is to provide neural afferent modulation of the residual muscle through mechanoneural actuation by the serially coupled myoneural actuator. **b**, The Achilles tendon is separated into half to prepare a residual muscle and myoneural actuator. **c**, Both residual muscle and myoneural actuator are brought to the anterior site of the tibia and surgically coupled using one of the tendons. To prevent the conjunction from sliding off towards the knee, the other tendon is used to mechanically ground the conjunction to the distal site. This allows three mechanical groundings consisting of tendons, serving as a stable biomechanical architecture for mechanoneural actuation. **d**, A pair of sonocrystals is inserted into the residual muscle to record muscle strains. **e**, A nerve cuff is put at the branch of tibial nerve that innervates the residual muscle to allow recording of modulated muscle afferents. A hook electrode is placed on the sural nerve for myoneural actuator control.

Statistics

All reported results for the native muscles and myoneural actuators were presented as mean ± standard error of the mean (SEM). To verify normality of the data, we utilized the Shapiro-Wilk test at a significance level of $\alpha = 0.05$. Two-sided paired and unpaired *t* tests were utilized for within-group and between-group comparisons, respectively. The closed-loop force control performance analyses were evaluated by slopes (m) between the target and performed force values along with their corresponding R^2 and P values. All statistical analyses were performed using MATLAB 2022b (Mathworks, USA). For the PMI afferent modulation analysis, Kendall's tau coefficients (τ) were reported between varying residual muscle strains, evoked afferents, and stimulation PW applied to the actuator along with their corresponding P values.

Results and Discussion

Myoneural Actuator Sustainability and Fatigue Resistance

The myoneural actuator was demonstrated in a rodent model, where the lateral gastrocnemius (L. GAS) muscle and sural nerve were used as the basis for the actuator and reinnervation, respectively (Figure 24a). The maximum isometric force and mass of the myoneural actuator were accessed at 9, 12, and 15 weeks, and no significant differences were found across all time points ($n = 5$ for each time point, unpaired *t* tests, force: $P > 0.91$, mass: $P > 0.34$) (Figure 24b). The myoneural actuator provided a comparable force-to-mass scaling factor to the native muscles (native $n = 8$, myoneural actuator $n = 15$, unpaired *t* test, $P = 0.19$) (Figure 24c). These results indicate that the myoneural actuator provides the long-term sustainability of force and mass, with an equivalent force scaling factor to actuator mass compared to native muscles.

The proposed myoneural actuator offers a key advantage in terms of augmented fatigue resistance. Fatigue response was tested for short periodical stimulations and long continuous stimulation. For the short periodical stimulation protocol, a series of 22 contraction cycles were performed, consisting of 1-second long stimulations with incremental pulse width (PW; up to 15%) followed by 10-second resting periods (Figure 24d). The myoneural actuators were able to maintain maximum output forces across the series of stimulation cycles (90 ± 3%). In contrast, native muscles were not able to withstand the series of muscle contractions (67 ± 3%) even with resting times that were 1,000% of the actuation time. As a result, the myoneural actuator exhibited an 34% enhanced muscle fatigue resistance compared to native muscles (intact: $n = 8$, actuators: $n = 13$, unpaired *t* test, $P < 0.001$). The fatigue responses under continuous stimulation showed even larger difference (Figure 24e). The myoneural actuator fatigue time (18.67 ± 2.96 s) was augmented by 260% compared to native muscles (5.19 ± 1.16 s; native: $n = 7$, actuator: $n = 4$, unpaired *t* test, $P < 0.001$) (Figure 24f).

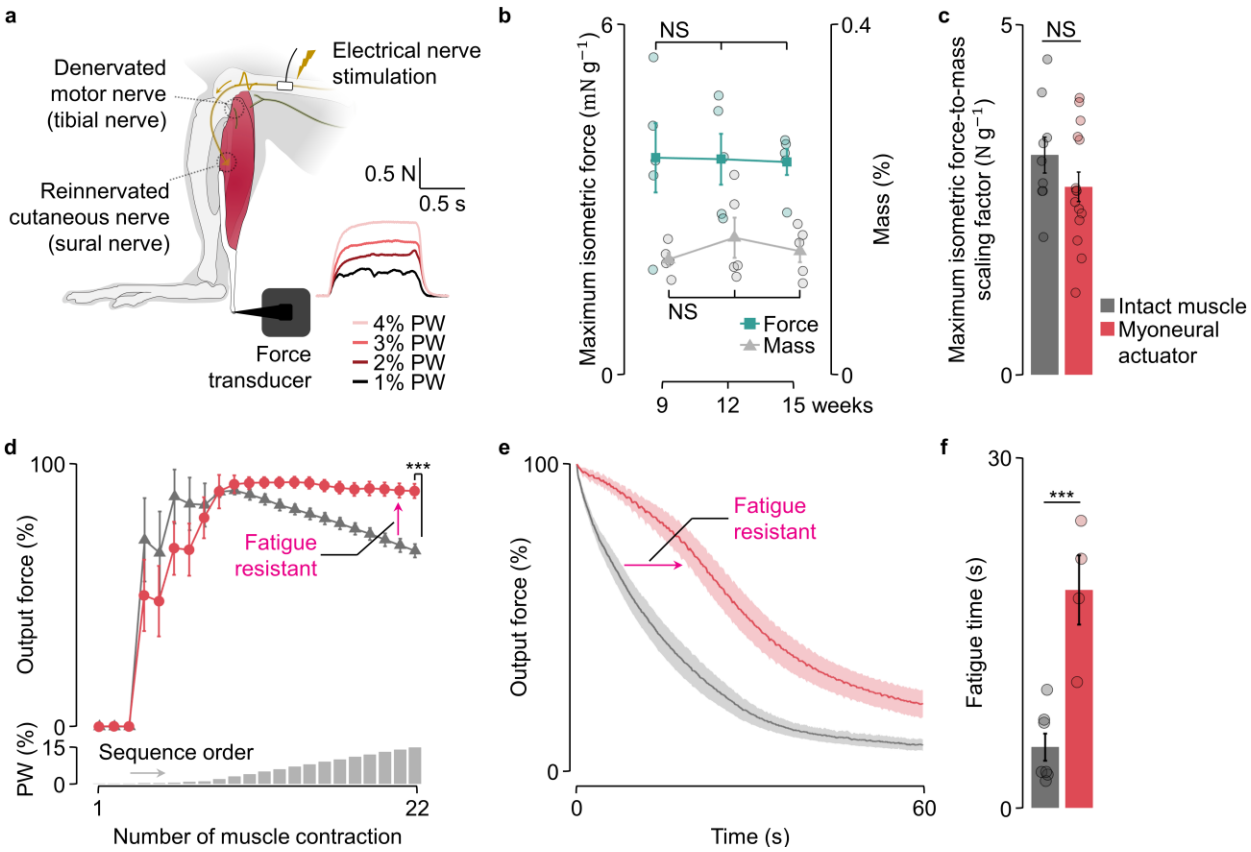

Figure 24 | Myoneural actuator sustainability and fatigue resistance. a, An experimental setup for characterizing the myoneural actuator is shown. The distal tendon of the actuator is fixed to a force transducer, while a hook electrode is placed on the reinnervated cutaneous nerve. An example force trace is displayed for 70 μA at 40 Hz stimulation with varying pulse width (PW). **b**, The maximum isometric force and mass of the myoneural actuator over 9 to 15 weeks post-surgical intervention are shown (n = 5 per cohort; bolded points, mean; error bars, SEM). **c**, The force-to-mass scaling factors of the biologically-intact muscle and myoneural actuator are displayed (intact: n = 8, actuator: n = 15; bars, mean; error bars, SEM). **d**, Force fatigue responses to repeated, discrete stimulations are presented (intact: n = 8, actuator: n = 13; bolded points, mean; error bars, SEM). Each stimulation lasts for 1 s with incremented stimulation intensity (up to 15% PW), followed by 10 s of a resting period (n = 22 cycles in total). **e**, **f**, Force fatigue responses (**e**) and fatigue time (**f**) to continuous stimulation of 4% PW are reported (intact: n = 7, actuator: n = 4; bolded lines, mean; shaded regions, SEM). Group comparisons were conducted using unpaired t tests (***P < 0.001; NS, not significant).

Myoneural Actuator Control

To assess myoneural actuator controllability, closed-loop force control was implemented using force reading from the force transducer (Figure 25a). Force control performance was tested for three different levels including 30%, 50%, and 70% of the maximum force (Figure 25b). The results revealed that the myoneural actuators provide comparable controllability compared to native muscles at all three-target forces (native: $n = 5$, actuator: $n = 8$, unpaired t tests, $P > 0.19$) (Figure 25c). Further, the actuators showed high linearity ($m = 0.93$, $R^2 > 0.99$, $P < 0.001$) at the similar level as native muscles ($m = 0.94$, $R^2 > 0.99$, $P < 0.001$).

In numerous muscle-actuated systems, the demand for high force output from a myoneural actuator may necessitate high nerve stimulation, which can generate undesired afferent signals that may cause discomfort or pain. To address this issue, a nerve block technique was integrated with a myoneural actuator to achieve electrophysiologically isolated actuation. Among various nerve block mechanisms[108–110,114–116], electrical nerve block[108–110] provides ease implementation and control. The nerve block was verified by applying it proximal to the nerve stimulation from the myoneural actuator (Figure 25d), which resulted in the blockage of distal nerve stimulation and the disabling of the myoneural actuator (Figure 25e). This demonstrated the effectiveness of the nerve block technique in preventing effective channeling across the nerve block (Figure 25f). Subsequently, the controllability of the myoneural actuator under the nerve block was tested by applying it distal to the nerve stimulation (Figure 25g). The results showed that the myoneural actuator can be controlled gradually while retaining high linearity ($m = 0.85$, $R^2 = 0.97$, $P < 0.001$) (Figure 25h, 25i). In future work, the control performance of the myoneural actuator may be further improved by implementing an active disturbance rejection mechanism into the control design[117,118] or possibly integrating with different nerve block mechanisms such as using localized cooling[114] and chemical dosing[115,116].

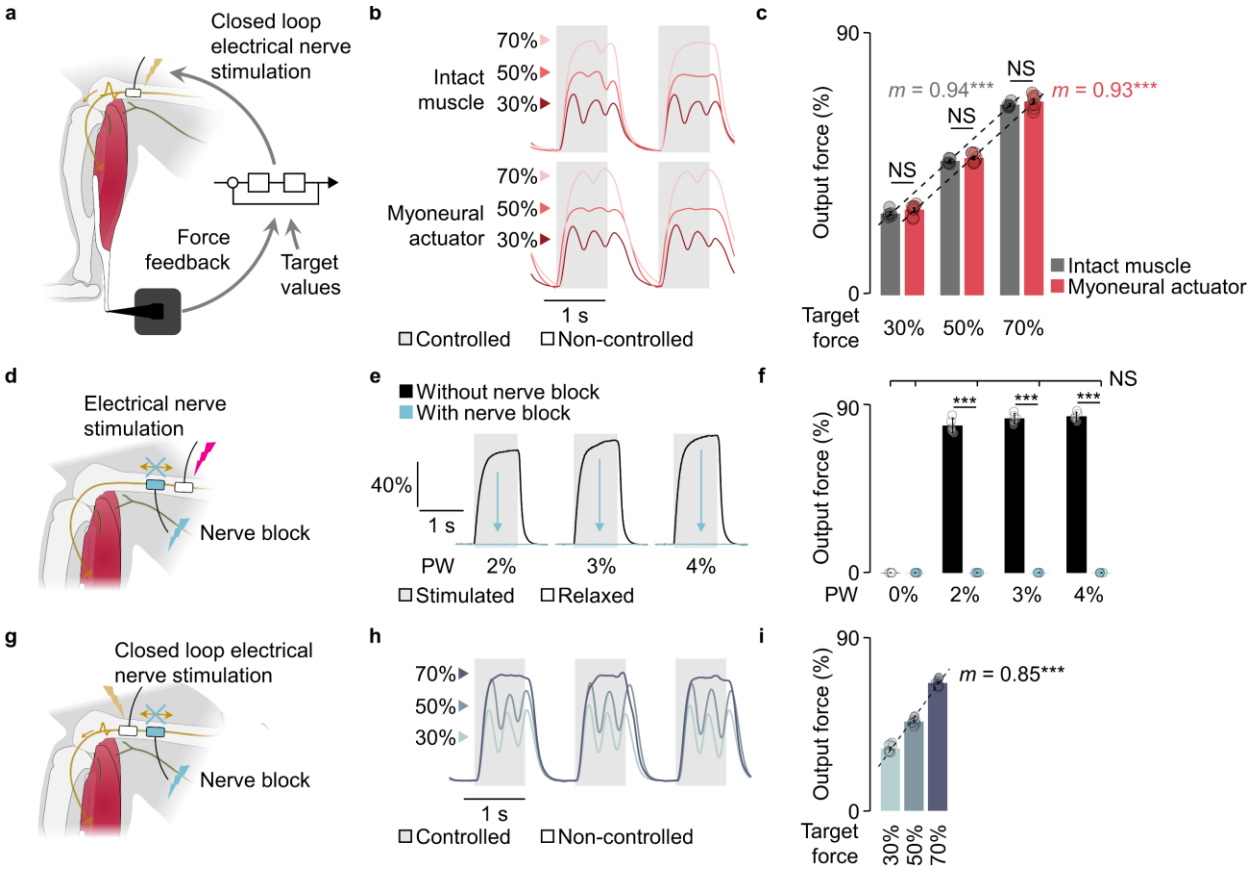

Figure 25 | Myoneural actuator control. a, The closed-loop control of the myoneural actuator based on force feedback is shown. **b**, A representative closed-loop force control of an intact muscle and myoneural actuator are shown for three different target force levels. **c**, The force control performance of intact muscles and myoneural actuators is shown (intact: $n = 5$, actuator: $n = 8$; bars, mean; error bars, SEM). Slopes (m) between target and performed forces are reported. **d**, The experimental setup for electrical nerve block validation is shown. The nerve block is applied proximal to the stimulation for myoneural actuator control. **e**, Force traces under varying stimulation intensity (2 to 4% PW) with and without proximal nerve block are shown. **f**, The output force with and without nerve block is compared ($n = 10$ cycles per each PW). **g**, The experimental setup for closed-loop force control with nerve block is shown. **h**, Closed-loop force performances with distal nerve block are demonstrated. **i**, The force control performance of myoneural actuator with nerve block is shown for three different target force levels ($n = 10$ cycles per each level). Slopes (m) between target and performed forces are reported. For these analyses, unpaired t tests were used (***$P < 0.001$; NS, not significant).

Direct Proprioceptive Afferent Modulation

The properties of the actuator allow for the design and control of active mechanics in biological systems. In this study, two biohybrid systems were presented, each involving linear and circular actuation. The first biohybrid neuroprosthetic interface, Proprioceptive Mechanoneural Interface (PMI), was designed to enable the modulation of proprioceptive afferents from residual muscles after amputation (Figure 26a). The PMI consisted of pairs of a serially coupled myoneural actuator and residual muscle. By controlling the linear actuation on a residual muscle, the PMI allowed for the direct modulation of residual muscle stretch which in turn evokes proprioceptive afferents from sensory organs within the residual muscle-tendon (mechanoneural actuation). Multiple PMIs can be constructed for each residual muscle to control residual muscle dynamics corresponding to neuroprosthetic joint dynamics (Figure 26a). Direct modulation of mechanoneural actuation would emulate biomimetic mecahnoneural actuation caused by antagonist muscles and external forces such as gravity and ground reaction forces in residual muscles, providing natural proprioceptive feedback of the prosthetic limb. In the PMI demonstration in rodent model, a residual muscle was simulated using medial gastrocnemius muscle (M. GAS). The myoneural actuator was surgically coupled with M. GAS at the anterior site of the tibia (Figure 26b). Gradual modulation of neural afferents from M. GAS was tested by gradually increasing the level of myoneural actuation (0 – 8% PW). The results showed that both M. GAS strains and evoked neural afferents increased as the level of myoneural actuation increased (n = 10 cycles per each level, strains: τ = 0.78, afferents: τ = 0.84, $P < 0.001$), demonstrating the afferent modulation capability of the PMI (Figure 26c).

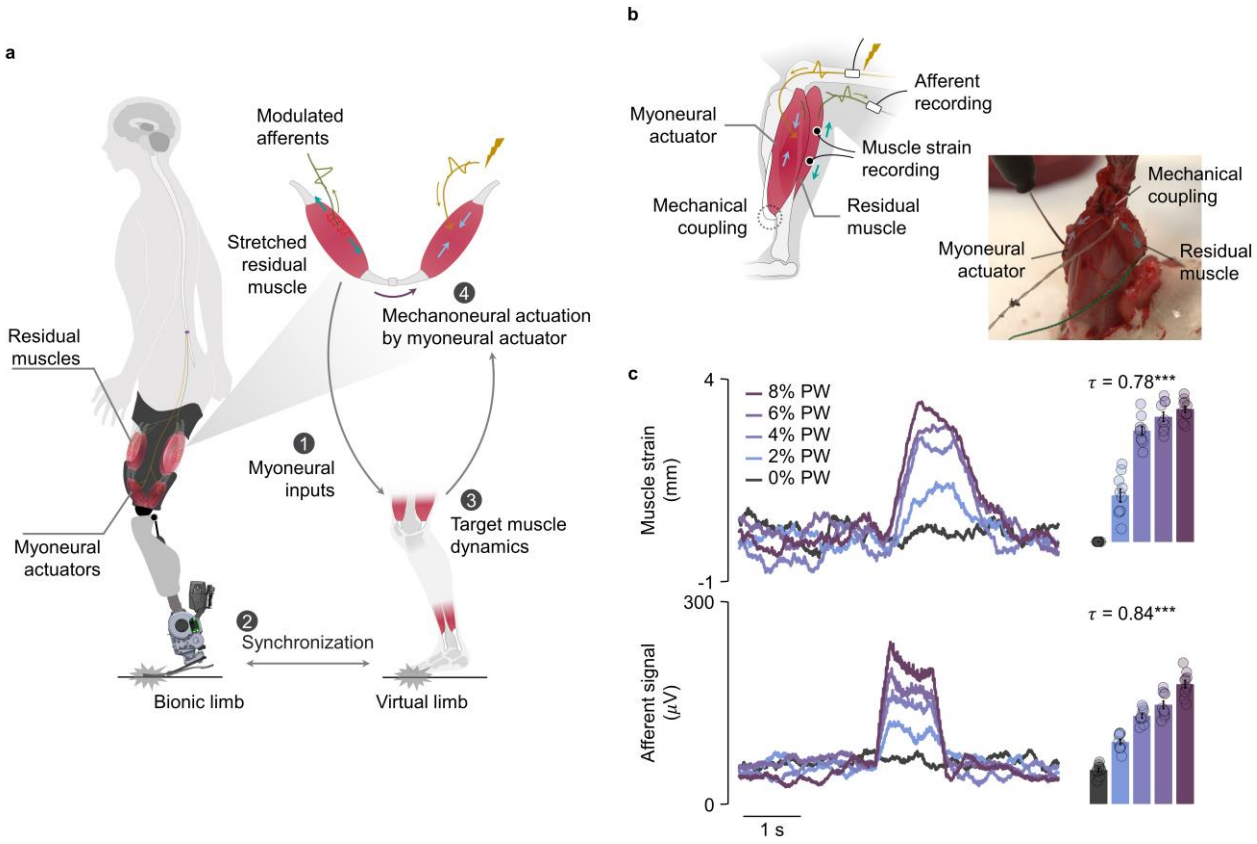

Figure 26 | Demonstration of Proprioceptive Mechanoneural Interface (PMI). a, The depicted neuroprosthetic interface is the PMI, which enables neural afferent feedback corresponding to neuroprosthetic limb movements. The PMI comprises residual muscles that are serially coupled with myoneural actuators, offering direct controllability of mechanoneural actuation. Biomimetic neural afferent feedback can be attained by adjusting residual muscle dynamics to match those of an intact limb that was amputated previously. **b**, The PMI demonstration in a rodent model is illustrated, with the medial gastrocnemius (M. GAS) serving as a residual muscle and serially coupled with a myoneural actuator located at the anterior site of the tibia. **c**, Muscle strains and afferent signals from the residual muscle for different levels of applied myoneural actuation (n = 10 cycles per each level) are shown. The PMI exhibits gradual controllability of residual muscle afferents, as shown by Kendall's tau coefficients (τ) between various levels of myoneural actuation, residual muscle strains, and evoked afferents. **d**, A biohybrid organ system is depicted, in which an organ such as an intestine is integrated with the myoneural actuator to provide control of mechanical functions. **e**, The biohybrid intestine demonstration in a rodent model is shown. **f**, The operation of the biohybrid intestine is illustrated, with varying levels of mechanical intestine activity modulated by the myoneural actuator.

Concluding Remarks

The implications of presented myoneural mechanisms go far beyond augmenting the muscle fatigue resistance, as it can be generalized to manipulate fiber composition to optimize actuator properties for application needs. The study demonstrated that reinnervation of a nerve with small axons promotes the formation of fatigue-resistant, slow-twitch muscle fibers. This suggests that if an impulsive actuation for only a short duration is required for an application, using a nerve with large axons for reinnervation would result in an optimal myoneural actuator. Leveraging the dependency of muscle fiber re-composition on the axon size of a reinnervating nerve may allow for the customization of myoneural actuators for specific applications.

Future efforts could focus on developing surgical designs to secure the muscle basis for a myoneural actuator. One potential surgical technique could involve splitting a muscle in half while maintaining its vascularization to use only one half as a myoneural actuator. The other half could be preserved for its function or used as other components of a biohybrid system. Additionally, the development of different scales and types of myoneural actuators that use muscle grafts or smooth muscle could significantly expand the design freedom for embedding active mechanics in biological systems.

The present study demonstrates the potential impact of the myoneural actuator technology that enables to design and control of active mechanics in biological systems through the novel mechanoneural interface, PMI. The PMI is designed to enable direct modulation of proprioceptive afferents from a residual muscle for neuroprosthetic limbs through linear actuation on a residual muscle. The myoneural actuator in biohybrid mechanoneural interfaces is not limited to muscle proprioceptive afferent modulation. It can also be used for mechanoneural actuation of other sensory end organs, such as skin, to modulate other sensory modalities such as cutaneous sensation[119]. This approach of using actuators can be extended to broader scope of organs requiring mechanical actuation, such as the bladder[120,121], diaphragm[122], and heart[123]. Future efforts could also focus on developing biohybrid systems on a different scale by using different scale myoneural actuators, such as muscle grafts or smooth muscles.

Chapter 6. Summary and Conclusion

Summary

This doctoral investigation aimed to explore the impact of preserved muscle neurophysiology in the residuum of individuals with below-knee amputation. Chapter 2 was focused on assessing sensorimotor responses associated with a wide range of free-space phantom limb control based on the muscle synergy theory. The level of muscle neurophysiology preservation was evaluated via agonist-antagonistic muscle strain (AMS) compared to biological counterparts. The outcomes revealed significant correlations between all sensorimotor responses and AMS, and it was estimated that providing 21-26% of biologically-intact values would enable preservation of biomimetic free-space motor control. In Chapters 3 and 4, the study demonstrated the first biomimetic prosthetic gait fully driven by the human nervous system. Here, the level of muscle neurophysiology preservation was evaluated by estimating afferent signaling in the residuum during maximum phantom ankle movements (agonist-antagonist muscle afferents). The findings indicated that even modest preservation of 17.5% of biologically-intact value in the residuum sufficed to enable versatile bionic gait responsive to environmental perturbations. While diverse sensorimotor responses and muscle neurophysiology metrics were assessed, the results suggest that even modest preservation of biomechanics or afferent signaling in the residuum enables fine motor control and perception. The study highlights that partial reinstatement may be adequate to achieve high degrees of neuroprosthetic integration necessary for human locomotion, given the challenges associated with complete afferent restoration.

Chapter 5 of this doctoral study focused on the development of a myoneural actuator technology that enhances fatigue resistance while maintaining the same force-to-mass scaling factor as native muscles. The study proposed a potential myoneural mechanism for manipulating muscle fiber composition in the myoneural actuator, thereby enabling the optimization of myoneural actuator properties based on application requirements. The study demonstrated the capability of the myoneural actuator to emulate actuation mechanisms underlying neural signaling and function in biology, thereby enabling direct control of these mechanisms.

Conclusion

The doctoral work advocates for the perspective that the human body should be viewed as a target for engineering, or *biomechatronics*. Through exploring the relationships between residual muscle physiology and sensorimotor responses, the study aims to provide design principles for future biomechatronics. The developed myoneural actuator technology provides considerable design freedom, offering opportunities to optimize the design of surgical reconstructions in a way that is similar to conventional mechatronic design processes. By considering future surgical reconstruction as a design optimization problem of biomechatronics for given constraints and target specifications, the work aims to enable more effective and precise approaches to enhancing human function and quality of life.

Bibliography

1. Cimolato, A. *et al.* EMG-driven control in lower limb prostheses: A topic-based systematic review. *J. NeuroEng. Rehabil.* **19**, 43 (2022).
2. Eilenberg, M. F., Geyer, H. & Herr, H. M. Control of a powered ankle–foot prosthesis based on a neuromuscular model. *IEEE Trans. Neural Syst. Rehabil. Eng.* **18**, 164–173 (2010).
3. Herr, H. M. & Grabowski, A. M. Bionic ankle–foot prosthesis normalizes walking gait for persons with leg amputation. *Proc. R. Soc. B.* **279**, 457–464 (2012).
4. Shultz, A. H., Lawson, B. E. & Goldfarb, M. Variable cadence walking and ground adaptive standing with a powered ankle prosthesis. *IEEE Trans. Neural Syst. Rehabil. Eng.* **24**, 495–505 (2016).
5. Mendez, J., Hood, S., Gunnel, A. & Lenzi, T. Powered knee and ankle prosthesis with indirect volitional swing control enables level-ground walking and crossing over obstacles. *Sci. Robot.* **5**, eaba6635 (2020).
6. Lenzi, T., Hargrove, L. & Sensinger, J. Speed-adaptation mechanism: Robotic prostheses can actively regulate joint torque. *IEEE Robot. Automat. Mag.* **21**, 94–107 (2014).
7. Culver, S., Bartlett, H., Shultz, A. & Goldfarb, M. A stair ascent and descent controller for a powered ankle prosthesis. *IEEE Trans. Neural Syst. Rehabil. Eng.* **26**, 993–1002 (2018).
8. Jing Wang, Kannape, O. A. & Herr, H. M. Proportional EMG control of ankle plantar flexion in a powered transtibial prosthesis. in *IEEE Int. Conf. Rehabil. Robot.* 1–5 (IEEE, 2013). doi:10.1109/ICORR.2013.6650391.
9. Chen, B., Wang, Q. & Wang, L. Adaptive slope walking with a robotic transtibial prosthesis based on volitional EMG control. *IEEE/ASME Trans. Mechatron.* **20**, 2146–2157 (2015).
10. Hargrove, L. J., Young, A. J. & Simon, A. M. Intuitive control of a powered prosthetic leg during ambulation: A randomized clinical trial. *Jama* **63**, 1405–1406 (2016).
11. He Huang *et al.* Continuous locomotion-mode identification for prosthetic Legs based on neuromuscular–mechanical fusion. *IEEE Trans. Biomed. Eng.* **58**, 2867–2875 (2011).
12. Hargrove, L. J. *et al.* Robotic leg control with EMG decoding in an amputee with nerve transfers. *N. Engl. J. Med.* **369**, 1237–1242 (2013).
13. Song, S. & Geyer, H. A neural circuitry that emphasizes spinal feedback generates diverse behaviours of human locomotion. *J. Physiol.* **593**, 3493–3511 (2015).
14. Harkema, S. *et al.* Effect of epidural stimulation of the lumbosacral spinal cord on voluntary movement, standing, and assisted stepping after motor complete paraplegia: a case study. *Lancet* **377**, 1938–1947 (2011).
15. Grillner, S. Biological pattern generation: The cellular and computational logic of networks in motion. *Neuron* **52**, 751–766 (2006).
16. Proske, U. & Gandevia, S. C. The proprioceptive senses: Their roles in signaling body shape, body position and movement, and muscle Force. *Physiol. Rev.* **92**, 1651–1697 (2012).
17. Prochazka, A. Proprioceptive feedback and movement regulation. *Compr. Physiol.* **76**, 89–127 (1996).
18. Brown, B. J. *et al.* Outcomes after 294 transtibial amputations with the posterior myocutaneous flap. *Int. J. Low. Extrem. Wounds* **13**, 33–40 (2014).
19. Petrini, F. M. *et al.* Enhancing functional abilities and cognitive integration of the lower limb prosthesis. *Sci. Transl. Med.* **11**, eaav8939 (2019).

20. Charkhkar, H. *et al.* High-density peripheral nerve cuffs restore natural sensation to individuals with lower-limb amputations. *J. Neural Eng.* **15**, 056002 (2018).
21. Petrini, F. M. *et al.* Sensory feedback restoration in leg amputees improves walking speed, metabolic cost and phantom pain. *Nat. Med.* **25**, 1356–1363 (2019).
22. Charkhkar, H., Christie, B. P. & Triolo, R. J. Sensory neuroprosthesis improves postural stability during sensory organization test in lower-limb amputees. *Sci. Rep.* **10**, 6984 (2020).
23. Kuiken, T. A. *et al.* Targeted Muscle Reinnervation for Real-time Myoelectric Control of Multifunction Artificial Arms. *JAMA* **301**, 619–628 (2009).
24. Mioton, L. M. & Dumanian, G. A. Targeted muscle reinnervation and prosthetic rehabilitation after limb loss. *J. Surg. Oncol.* **118**, 807–814 (2018).
25. Myers, H., Lu, D., Gray, S. J. & Bruscino-Raiola, F. Targeted muscle reinnervation to improve electromyography signals for advanced myoelectric prosthetic limbs: a series of seven patients. *ANZ J. Surg.* **90**, 591–596 (2020).
26. Vu, P. P. *et al.* A regenerative peripheral nerve interface allows real-time control of an artificial hand in upper limb amputees. *Sci. Transl. Med.* **12**, eaay2857 (2020).
27. Woo, S. L. *et al.* Partial Skeletal Muscle Grafts for Prosthetic Control. *Plast. Reconst. Surg.* **134**, 55–56 (2014).
28. Clites, T. R., Carty, M. J., Srinivasan, S. S., Zorzos, A. N. & Herr, H. M. A murine model of a novel surgical architecture for proprioceptive muscle feedback and its potential application to control of advanced limb prostheses. *J. Neural Eng.* **14**, 036002 (2017).
29. Clites, T. R. *et al.* Proprioception from a neurally controlled lower-extremity prosthesis. *Sci. Transl. Med.* **10**, eaap8373 (2018).
30. Song, H. *et al.* Agonist-antagonist muscle strain in the residual limb preserves motor control and perception after amputation. *Commun. Med.* **2**, 97 (2022).
31. Edin, B. B. & Johansson, N. Skin strain patterns provide kinaesthetic information to the human central nervous system. *J. Physiol.* **487**, 243–251 (1995).
32. Herr, H. M. *et al.* Reinventing extremity amputation in the era of functional limb restoration. *Ann. Surg.* **273**, 269–279 (2021).
33. Bovi, G., Rabuffetti, M., Mazzoleni, P. & Ferrarin, M. A multiple-task gait analysis approach: Kinematic, kinetic and EMG reference data for healthy young and adult subjects. *Gait & Posture* **33**, 6–13 (2011).
34. Fleming, A., Huang, S., Buxton, E., Hodges, F. & Huang, H. H. Direct continuous electromyographic control of a powered prosthetic ankle for improved postural control after guided physical training: A case study. *Wearable Technol.* **2**, e3 (2021).
35. Huang, S., Wensman, J. P. & Ferris, D. P. Locomotor adaptation by transtibial amputees walking with an experimental powered prosthesis under continuous myoelectric control. *IEEE Trans. Neural Syst. Rehabil. Eng.* **24**, 573–581 (2016).
36. Huang, S. & Ferris, D. P. Muscle activation patterns during walking from transtibial amputees recorded within the residual limb-prosthetic interface. *J. NeuroEng. Rehabil.* **9**, 55 (2012).
37. Seyedali, M., Czerniecki, J. M., Morgenroth, D. C. & Hahn, M. E. Co-contraction patterns of trans-tibial amputee ankle and knee musculature during gait. *J. NeuroEng. Rehabil.* **9**, 29 (2012).
38. Cheung, V. C. K., d'Avella, A., Tresch, M. C. & Bizzi, E. Central and Sensory Contributions to the Activation and Organization of Muscle Synergies during Natural Motor Behaviors. *J. Neurosci.* **25**, 6419–6434 (2005).

39. Cheung, V. C. K. *et al.* Muscle synergy patterns as physiological markers of motor cortical damage. *Proc. Natl. Acad. Sci.* **109**, 14652–14656 (2012).
40. Torres-Oviedo, G. & Ting, L. H. Muscle Synergies Characterizing Human Postural Responses. *J. Neurophysiol.* **98**, 2144–2156 (2007).
41. Orendurff, M. S. *et al.* Functional level assessment of individuals with transtibial limb loss: Evaluation in the clinical setting versus objective community ambulatory activity. *J. Rehabil. Assist. Technol. Eng.* **3**, 205566831663631 (2016).
42. Taylor, B. & Poka, A. Osteomyoplastic transtibial amputation: The Ertl technique. *J. Am. Acad. Orthop. Surg.* 259–265 (2016).
43. Farris, D. J. & Lichtwark, G. A. UltraTrack: Software for semi-automated tracking of muscle fascicles in sequences of B-mode ultrasound images. *Comput. Methods Programs Biomed.* **128**, 111–118 (2016).
44. Gillett, J. G., Barrett, R. S. & Lichtwark, G. A. Reliability and accuracy of an automated tracking algorithm to measure controlled passive and active muscle fascicle length changes from ultrasound. *Comput. Methods Biomech. Biomed. Eng.* **16**, 678–687 (2013).
45. Menegaldo, L. L., de Toledo Fleury, A. & Weber, H. I. Moment arms and musculotendon lengths estimation for a three-dimensional lower-limb model. *J. Biomech.* **37**, 1447–1453 (2004).
46. Lee, D. D. & Seung, H. S. Learning the parts of objects by non-negative matrix factorization. *Nature* **401**, 788–791 (1999).
47. Ji, Q. *et al.* Assessment of ankle muscle activation by muscle synergies in healthy and post-stroke gait. *Physiol. Meas.* **39**, 045003 (2018).
48. Frère, J. & Hug, F. Between-subject variability of muscle synergies during a complex motor skill. *Front. Comput. Neurosci.* **6**, (2012).
49. Sakurada, T., Knoblich, G., Sebanz, N., Muramatsu, S. & Hirai, M. Probing links between action perception and action production in Parkinson's disease using Fitts' law. *Neuropsychologia* **111**, 201–208 (2018).
50. Corben, L. A. *et al.* The Fitts task reveals impairments in planning and online control of movement in Friedreich ataxia: reduced cerebellar-cortico connectivity? *Neuroscience* **192**, 382–390 (2011).
51. Medina, J., Jax, S. A. & Coslett, H. B. Two-component models of reaching: Evidence from deafferentation in a Fitts' law task. *Neurosci. Lett.* **451**, 222–226 (2009).
52. Aman, J. E., Elangovan, N., Yeh, I.-L. & Konczak, J. The effectiveness of proprioceptive training for improving motor function: a systematic review. *Front. Hum. Neurosci.* **8**, (2015).
53. Azim, E. & Seki, K. Gain control in the sensorimotor system. *Curr. Opin. Physiol.* **8**, 177–187 (2019).
54. Guermazi, A. *et al.* Imaging of Muscle Injuries in Sports Medicine: Sports Imaging Series. *Radiology* **282**, 646–663 (2017).
55. Bizzi, E., Tresch, M. C., Saltiel, P. & d'Avella, A. New perspectives on spinal motor systems. *Nat. Rev. Neurosci.* **1**, 101–108 (2000).
56. Anderson-Barnes, V. C., McAuliffe, C., Swanberg, K. M. & Tsao, J. W. Phantom limb pain – A phenomenon of proprioceptive memory? *Med. Hypotheses* **73**, 555–558 (2009).
57. Jensen, T. S., Krebs, B., Nielsen, J. & Rasmussen, P. Immediate and long-term phantom limb pain in amputees: Incidence, clinical characteristics and relationship to pre-amputation limb pain. *Pain* **21**, 267–278 (1985).

58. Katz, J. & Melzack, R. Pain ‘memories’ in phantom limbs: review and clinical observations. *Pain* **43**, 319–336 (1990).
59. Srinivasan, S. S. *et al.* On prosthetic control: A regenerative agonist-antagonist myoneural interface. *Sci. Robot.* **2**, eaan2971 (2017).
60. Clites, T. R., Herr, H. M., Srinivasan, S. S., Zorzos, A. N. & Carty, M. J. The Ewing Amputation: The First Human Implementation of the Agonist-Antagonist Myoneural Interface. *Plast. Reconstr. Surg.* **6**, e1997 (2018).
61. Bourke, H. E., Yelden, K. C., Robinson, K. P., Sooriakumaran, S. & Ward, D. A. Is revision surgery following lower-limb amputation a worthwhile procedure? A retrospective review of 71 cases. *Injury* **42**, 660–666 (2011).
62. Collins, S. H., Wiggin, M. B. & Sawicki, G. S. Reducing the energy cost of human walking using an unpowered exoskeleton. *Nature* **522**, 212–215 (2015).
63. Ahn, J. & Hogan, N. Walking is not like reaching: Evidence from periodic mechanical perturbations. *PLOS ONE* **7**, e31767 (2012).
64. Yeon, S. H. *et al.* Acquisition of surface EMG using flexible and low-profile electrodes for lower extremity neuroprosthetic control. *IEEE Trans. Med. Robot. Bionics* **3**, 563–572 (2021).
65. Hsieh, T.-H. Design and control of a two-degree-of-freedom powered ankle-foot prosthesis. (Massachusetts Institute of Technology, 2019).
66. Hogan, N. Adaptive control of mechanical impedance by coactivation of antagonist muscles. *IEEE Trans. Automat. Contr.* **29**, 681–690 (1984).
67. Hogan, N. The mechanics of multi-joint posture and movement control. *Biol. Cybern.* **52**, 315–331 (1985).
68. Lee, H. & Hogan, N. Time-varying ankle mechanical impedance during human locomotion. *IEEE Trans. Neural Syst. Rehabil. Eng.* **23**, 755–764 (2015).
69. Hasson, C. J., Miller, R. H. & Caldwell, G. E. Contractile and elastic ankle joint muscular properties in young and older Adults. *PLOS ONE* **6**, e15953 (2011).
70. Anderson, D. E., Madigan, M. L. & Nussbaum, M. A. Maximum voluntary joint torque as a function of joint angle and angular velocity: Model development and application to the lower limb. *J. Biomech.* **40**, 3105–3113 (2007).
71. Yeon, S. H. & Herr, H. M. Rejecting impulse artifacts from surface EMG signals using real-time cumulative histogram filtering. in *IEEE Int. Conf. Eng. Med. Biol. Soc.* 6235–6241 (IEEE, 2021). doi:10.1109/EMBC46164.2021.9631052.
72. Markowitz, J. *et al.* Speed adaptation in a powered transtibial prosthesis controlled with a neuromuscular model. *Phil. Trans. R. Soc. B* **366**, 1621–1631 (2011).
73. Duval, J.-F. & Herr, H. M. FlexSEA: Flexible, scalable electronics architecture for wearable robotic applications. *IEEE Int. Conf. Biomed. Robot. Biomechatronics* 1236–1241 (2016) doi:10.1109/BIOROB.2016.7523800.
74. McFadyen, B. J. & Winter, D. A. An integrated biomechanical analysis of normal stair ascent and descent. *J. Biomech.* **21**, 733–744 (1988).
75. Siebers, H. L. *et al.* Comparison of different symmetry indices for the quantification of dynamic joint angles. *BMC Sports Sci. Med. Rehabil.* **13**, 130 (2021).
76. Montgomery, J. R. & Grabowski, A. M. The contributions of ankle, knee and hip joint work to individual leg work change during uphill and downhill walking over a range of speeds. *R. Soc. Open Sci.* **5**, 180550 (2018).

77. Godha, S. & Lachapelle, G. Foot mounted inertial system for pedestrian navigation. *Meas. Sci. Technol.* **19**, 075202 (2008).
78. Sinitski, E. H., Hansen, A. H. & Wilken, J. M. Biomechanics of the ankle–foot system during stair ambulation: Implications for design of advanced ankle–foot prostheses. *J. Biomech.* **45**, 588–594 (2012).
79. Yeon, S. H., Song, H. & Herr, H. M. Spatiotemporally synchronized surface EMG and ultrasonography measurement using a flexible and low-profile EMG electrode. in *IEEE Int. Conf. Eng. Med. Biol. Soc.* 6242–6246 (IEEE, 2021). doi:10.1109/EMBC46164.2021.9629789.
80. Formento, E. *et al.* Electrical spinal cord stimulation must preserve proprioception to enable locomotion in humans with spinal cord injury. *Nat. Neurosci.* **21**, 1728–1741 (2018).
81. Prochazka, A. Quantifying proprioception. *Prog. Brain Res.* **123**, 133–142 (1999).
82. Grey, M. J., Nielsen, J. B., Mazzaro, N. & Sinkjaer, T. Positive force feedback in human walking. *J. Neurophysiol.* **581**, 99–105 (2007).
83. Prochazka, A., Gillard, D. & Bennett, D. J. Positive force feedback control of muscles. *J. Neurophysiol.* **77**, 3226–3236 (1997).
84. Palmer, M. L. Sagittal plane characterization of normal human ankle function across a range of walking gait speeds. (Massachusetts Institute of Technology, 2002).
85. Lloyd, C. H., Stanhope, S. J., Davis, I. S. & Royer, T. D. Strength asymmetry and osteoarthritis risk factors in unilateral trans-tibial, amputee gait. *Gait & Posture* **32**, 296–300 (2010).
86. Au, S. & Herr, H. Powered ankle-foot prosthesis. *IEEE Robot. Automat. Mag.* **15**, 52–59 (2008).
87. Haefeli, J., Vögeli, S., Michel, J. & Dietz, V. Preparation and performance of obstacle steps: interaction between brain and spinal neuronal activity. *Eur. J. Neurosci.* **33**, 338–348 (2011).
88. McFadyen, B. J. & Carnahan, H. Anticipatory locomotor adjustments for accommodating versus avoiding level changes in humans: *Exp. Brain Res.* **114**, 500–506 (1997).
89. Guiard, Y., Olafsdottir, H. B. & Perrault, S. T. Fitt's law as an explicit time/error trade-off. in *Conf. Hum. Factors Comput. Syst.* 1619–1628 (ACM, 2011). doi:10.1145/1978942.1979179.
90. MacKenzie, I. S. & Isokoski, P. Fitts' throughput and the speed-accuracy tradeoff. in *Conf. Hum. Factors Comput. Syst.* 1633–1636 (ACM, 2008). doi:10.1145/1357054.1357308.
91. Malone, A., Kiernan, D., French, H., Saunders, V. & O'Brien, T. Obstacle crossing during gait in children with cerebral palsy: Cross-sectional study with kinematic analysis of dynamic balance and trunk Control. *Phys. Ther.* **96**, 1208–1215 (2016).
92. Latt, M. D., Lord, S. R., Morris, J. G. L. & Fung, V. S. C. Clinical and physiological assessments for elucidating falls risk in Parkinson's disease: Predictors of falls in Parkinson's Disease. *Mov. Disord.* **24**, 1280–1289 (2009).
93. Cappellini, G. *et al.* Locomotor patterns during obstacle avoidance in children with cerebral palsy. *J. Neurophysiol.* **124**, 574–590 (2020).
94. Khudados, E., Cody, F. W. J. & O'Boyle, D. J. Proprioceptive regulation of voluntary ankle movements, demonstrated using muscle vibration, is impaired by Parkinson's disease. *J. Neurol. Neurosurg. Psychiatry* **67**, 504–510 (1999).
95. Orr, A. W., Helmke, B. P., Blackman, B. R. & Schwartz, M. A. Mechanisms of Mechanotransduction. *Developmental Cell* **10**, 11–20 (2006).

96. Hahn, C. & Schwartz, M. A. Mechanotransduction in vascular physiology and atherogenesis. *Nat. Rev. Mol. Cell Biol.* **10**, 53–62 (2009).
97. Wang, Y. *et al.* Stimuli-responsive composite biopolymer actuators with selective spatial deformation behavior. *Proc. Natl. Acad. Sci.* **117**, 14602–14608 (2020).
98. Chin, S. Y. *et al.* Additive manufacturing of hydrogel-based materials for next-generation implantable medical devices. *Sci. Robot.* **2**, eaah6451 (2017).
99. Zheng, T. *et al.* Biocompatible Carbon Nanotube-Based Hybrid Microfiber for Implantable Electrochemical Actuator and Flexible Electronic Applications. *ACS Appl. Mater. Interfaces* **11**, 20615–20627 (2019).
100. Yan, B. Actuators for Implantable Devices: A Broad View. *Micromachines* **13**, 1756 (2022).
101. Enoka, R. M. & Duchateau, J. Muscle fatigue: what, why and how it influences muscle function: Muscle fatigue. *J. Physiol.* **586**, 11–23 (2008).
102. Wan, J., Qin, Z., Wang, P., Sun, Y. & Liu, X. Muscle fatigue: general understanding and treatment. *Exp. Mol. Med.* **49**, e384–e384 (2017).
103. Schätzlein, E. & Blaeser, A. Recent trends in bioartificial muscle engineering and their applications in cultured meat, biorobotic systems and biohybrid implants. *Commun. Biol.* **5**, 737 (2022).
104. Brushart, T. M. E. & Seiler, W. A. Selective reinnervation of distal motor stumps by peripheral motor axons. *Exp. Neurol.* **97**, 289–300 (1987).
105. Moradzadeh, A. *et al.* The impact of motor and sensory nerve architecture on nerve regeneration. *Exp. Neurol.* **212**, 370–376 (2008).
106. Gillespie, M. J. & Stein, R. B. The relationship between axon diameter, myelin thickness and conduction velocity during atrophy of mammalian peripheral nerves. *Brain Research* **259**, 41–56 (1983).
107. Tanner, J. Reversible Blocking of Nerve Conduction by Alternating-Current Excitation. *Nature* **195**, 712–713 (1962).
108. Williamson, R. P. & Andrews, B. J. Localized Electrical Nerve Blocking. *IEEE Trans. Biomed. Eng.* **52**, 362–370 (2005).
109. Eggers, T. *et al.* Combining direct current and kilohertz frequency alternating current to mitigate onset activity during electrical nerve block. *J. Neural Eng.* **18**, 046010 (2021).
110. Bhadra, N., Vrabec, T. L., Bhadra, N. & Kilgore, K. L. Reversible conduction block in peripheral nerve using electrical waveforms. *Bioelectronics in Medicine* **1**, 39–54 (2018).
111. Sunderland, S. & Ray, L. J. Denervation changes in mammalian striated muscle. *J. Neurol. Neurosurg. Psychiatry* **13**, 159–177 (1950).
112. Tower, S. S. The reaction of muscle to denervation. *Physiol. Rev.* **19**, 1–48 (1939).
113. Riso, R. R., Mosallaie, F. K., Jensen, W. & Sinkjaer, T. Nerve cuff recordings of muscle afferent activity from tibial and peroneal nerves in rabbit during passive ankle motion. *IEEE Trans. Rehab. Eng.* **8**, 244–258 (2000).
114. Reeder, J. T. *et al.* Soft, bioresorbable coolers for reversible conduction block of peripheral nerves. *Science* **377**, 109–115 (2022).
115. Simons, E. J., Bellas, E., Lawlor, M. W. & Kohane, D. S. Effect of Chemical Permeation Enhancers on Nerve Blockade. *Mol. Pharmaceutics* **6**, 265–273 (2009).
116. Lee, J. & Lee, Y. S. Percutaneous chemical nerve block with ultrasound-guided intraneural injection. *Eur Radiol* **18**, 1506–1512 (2008).

117. Han, J. From PID to Active Disturbance Rejection Control. *IEEE Trans. Ind. Electron.* **56**, 900–906 (2009).
118. Feng, H. & Guo, B.-Z. Active disturbance rejection control: Old and new results. *Annu. Rev. Control* **44**, 238–248 (2017).
119. S. Srinivasan, S. & M. Herr, H. A cutaneous mechanoneural interface for neuroprosthetic feedback. *Nat. Biomed. Eng* **6**, 731–740 (2021).
120. Arab Hassani, F., Jin, H., Yokota, T., Someya, T. & Thakor, N. V. Soft sensors for a sensing-actuation system with high bladder voiding efficiency. *Sci. Adv.* **6**, eaba0412 (2020).
121. Hassani, F. A. *et al.* A 3D Printed Implantable Device for Voiding the Bladder Using Shape Memory Alloy (SMA) Actuators. *Adv. Sci.* **4**, 1700143 (2017).
122. Hu, L. *et al.* An implantable soft robotic ventilator augments inspiration in a pig model of respiratory insufficiency. *Nat. Biomed. Eng* **7**, 110–123 (2022).
123. Roche, E. T. *et al.* Soft robotic sleeve supports heart function. *Sci. Transl. Med.* **9**, eaaf3925 (2017).